Hypatia
Colloquium

EARLY CAREER
ASTRONOMER SERIES
AT ESO 2021

ESO

PROCEEDINGS

G. Beccari
H.M.J. Boffin

Editors

Contents

COSMOLOGY

GALAXIES AND GALACTIC NUCLEI

INTERSTELLAR MEDIUM, STAR FORMATION and PLANETARY SYSTEMS

STELLAR EVOLUTION

Preface

As stipulated in the Convention signed almost 60 years ago, ESO's Mission is twofold: build and operate world-class astronomical telescopes and foster cooperation in astronomy. Engaging with the astronomical community is a vital element towards both overarching Mission goals. ESO has well-established activities in place to support this community engagement, not least the studentship and fellowship programmes (for scientists and engineers), summer internships, workshops etc. This returns important benefits: early career researchers get to grow professionally while they work at ESO, and they create standing links once they move forward to take up jobs elsewhere.

Early career scientists were and are among the most affected people by the COVID-19 pandemic that hit the world in early 2020. Lack of networking opportunities, of visiting other research institutions and of being able to present their own research work at conferences, seriously hampered their career opportunities. As part of its mandate to "foster cooperation in astronomy", ESO undertook several activities to facilitate networking during pandemic times. These included virtual tours to the observatories, on-line workshops, a series of scientific debates on various astronomical topics called the *Cosmic Duologues* and, specifically targeting early career scientists, the *Hypatia colloquia*. The Hypatia colloquia were born at the initiative of the ESO Offices for Science in order to provide a forum for early career astronomers (up to 3 years after the PhD) who could expose their research activities in front of a broad audience, to which ESO invited potential employers (grant holders, heads of University Departments and of Research Institutes, etc).

The demand to speak at the Hypatia colloquia was overwhelming, and choices had to be regretfully made. The colloquia were very well attended and therefore served their purpose. I'm aware consideration is being given to repeating the experience in 2022. At the end, the Hypatia colloquia may be one of the few positive impacts of the pandemic!

This book, kindly prepared by the ESO Faculty colleagues Giacomo Beccari and Henri Boffin, is a compilation of the presentations that were delivered during the colloquia. By reading it, one can get a panoramic view of state-of-the-art astronomical research topics as conducted by some of the most enthusiastic and motivated early career astronomers.

I encourage all astronomers to read it and enjoy it as much as I have.

Garching, 6 October 2021

Xavier Barcons
ESO Director-General

Introduction

Giacomo Beccari and Henri M.J. Boffin

European Southern Observatory, Karl-Schwarzschild-Strasse 2, 85748 Garching bei München

The COVID19 pandemic is a most dramatic challenge that affects the entire World. Almost two years of restrictions and social distancing have changed the way we live, work and interact with each other. Despite the closure of schools and universities, the adoption of distance learning measures has allowed to sustain the educational system in most countries, but has had deep consequences on the overall educational experience of the younger generations. Similarly, early career astronomers at all levels (PhD and post-doc) have been forced to adapt to a new working scenario that presented numerous challenges. The "classical" approaches needed to build a solid and gratifying professional profile, to create a network of collaborations, and to communicate the scientific results went through a complete revision which required (and still requires) creativity, strong commitment and support from senior astronomers, supervisors and mentors. At ESO, we felt the responsibility to invest our energy and creativity to put in place a channel to allow excellent young researchers to show the results of their scientific work.

Thanks to the positive experience of the ESO Cosmic Duologues series [1], we have now learned to which extent on-line seminars can be an efficient practice to engage and reach out to the astronomical community even under the severe restrictions imposed by the pandemic. As part of the ESO science activities, the Office for Science in the Directorate of Science therefore organised a new series of seminars called the *Hypatia Colloquium*, dedicated to early career scientists. This book collects the scientific contributions of most of the speakers of the first series in the form of proceedings.

The call for abstracts

At the beginning of November 2020, ESO released a call for abstracts through which PhD students and early post-docs (maximum 3 years from the PhD) working in any field of theoretical and observational astronomy and astrophysics, without any limitations of their nationality or host country, were invited to apply to be nominated as speaker of an Hypatia Colloquium. The new series was designed to host two seminars per event. This translated into 42 slots available for the talks. The deadline to send the application was set to November 30, 2020. In less than a month, ESO received 334 valid applications from young astronomers around the world.

The extremely positive reaction and participation from young astronomers already witness a strong desire to break the walls of confinement in which the pandemic has contained our scientific life and explore new spaces to express talent and creativity. The selection of the top speakers was done by an ad-hoc committee composed of ESO astronomers from both Garching and Vitacura, based on the scientific quality of the submitted abstracts and the speaker's contribution to the work. The 42 selected speakers were contacted towards mid-December and the full programme released before Christmas 2020.

The complete programme of the talks can be found on the dedicated web page[*]. The programme page reports the name and a picture of the speakers together with the title of the talk and the date and time of each event. By clicking on the title of the talk it is also possible to download the full abstract of the talk and a curriculum vitae of the speaker.
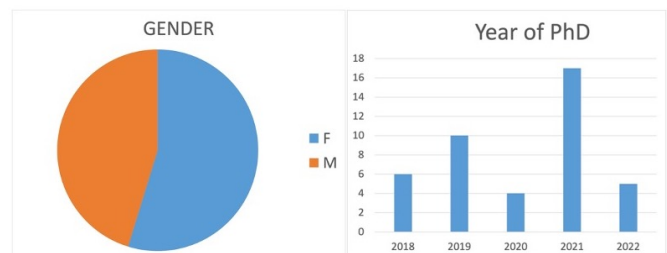
Figure 1: Distribution of gender and year of the PhD of the speakers of the Hypatia Colloquium series. The call was released on November 2020 meaning that all speakers whose PhD is planned in 2021 and 2022 where still PhD students at the time of giving the talk.

We show in Figure 1 the distribution of the gender (left pie-plot) and year of PhD (right histogram) of the speakers selected for the Hypatia Colloquium 2021. It is worth to note that the call was released in November 2020 and the program published at the end of the same year. Hence, at the time of giving their talk, half of the speakers had not yet completed their PhD. Impressing fact when considering the scientific quality of the talks!

The new series

The talks were scheduled on Tuesdays at 3pm Garching (Germany) time from February 2 to July 27, 2021 (except once per month, when there was an ESO Cosmic Duologue). The format of this series foresees two 20 min-long talks, each followed by questions and discussion. Most of the seminars were co-chaired by an ESO Student and an ESO Fellow.

The seminars were entirely hosted on-line using the video conferencing tool `Zoom` and live streamed on the Hypatia Colloquium `YouTube` channel[†]. Attendees could register to the series using a web form. Registered participants were able to attend the seminars and interact with the speakers via the `Zoom` meeting. Alternatively, the community was invited to attend the live events on the dedicated `YouTube` page. All `YouTube` attendees could ask questions during the live event using the Live Chat

---

[*]https://www.eso.org/sci/meetings/garching/hypatia-colloquium/program.html

[†]https://www.youtube.com/c/HypatiaColloquium/featured
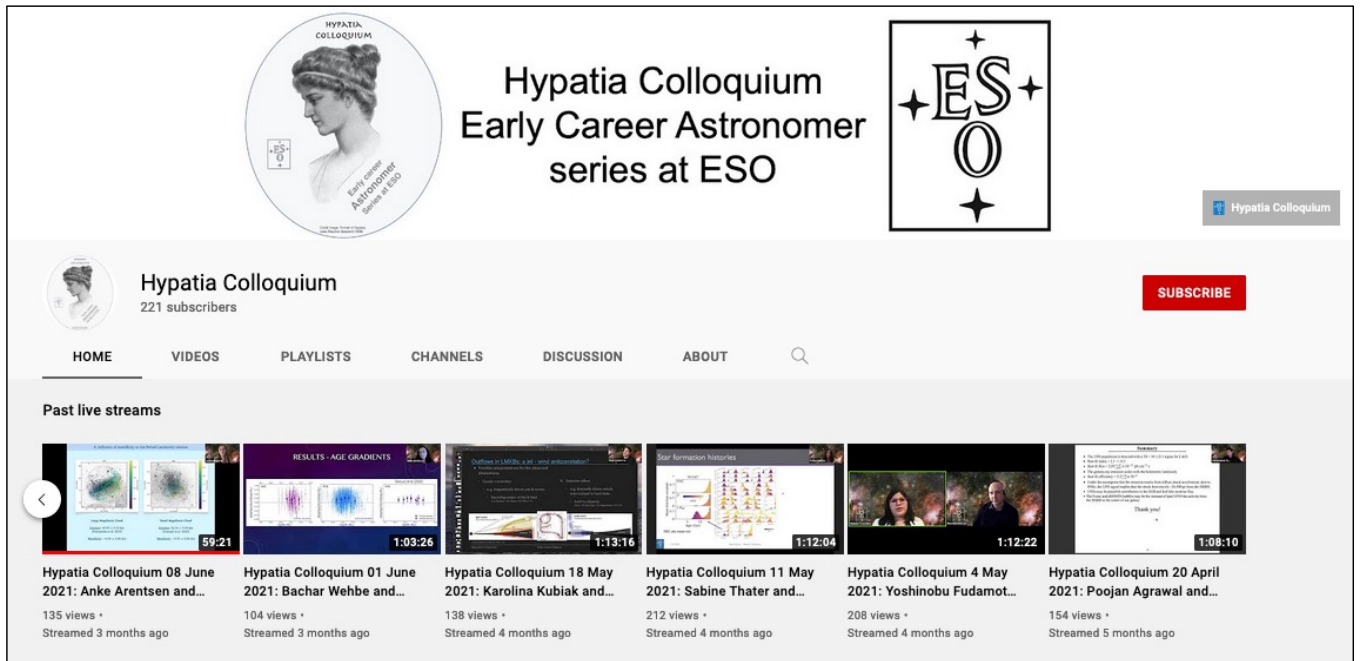
Figure 2: Snapshot of the YouTube channel of the Hypatia Colloquium. All the talks of the series of 2021 are available on the dedicated playlist.

on `YouTube` (or using a web form or by email if they preferred). All the video recordings of the live events, including the content of the live chat, are available on `YouTube`‡. We show in Figure 2 a snapshot of the front page of the Hypatia Colloquium `YouTube` channel.

The channel analytics clearly attests the success of the series. While each event was followed live by a total of 40 to 60 participants equally spread between `Zoom` and `YouTube`, the videos record (at the time of writing this introduction in October 2021) a total of almost 4 600 views. While the numbers are already quite impressing, it is when watching the seminars that the real quality and impact of the series can be fully appreciated. With the Hypatia Colloquium, ESO allowed the young generation of astronomers to paint a remarkable and unique portrait of the excellence of the science presently done by the early career astronomers. The videos available on-line represent an extraordinary and exploitable treasure and resource of talent.

The support to the young generation
The final words should be spent for all the young astronomers who are struggling during these challenging times. It is not easy to maintain the focus and motivation when such a dramatic event like the COVID19 pandemic is putting our (and our beloved's) health, life and safeness in great danger. Science is a wonderful endeavour which requires dedication and sacrifice but always pays back through astonishing discoveries that reveal the beauty hidden in our Universe.

Universities, research institutes, senior astronomers and mentors at all levels have now the responsibility to build the infrastructures and to redesign evaluation and hiring processes, in order to face the new reality with a modern attitude, adequate to the times and able to create the space for the creativity of the youngest generations to bloom and grow. At the same time, we must all help each other to remember that gratitude, humility, passion and professionalism are key ingredients to translate our efforts into knowledge for the future generations.

Reference
[1] Beccari, G., & Boffin, H. M. J. 2020, ESO Messenger, 181, 34

---

‡The links are all available on the web page of the programme

Road to the stars

A unique opportunity to conduct part of your PhD research at the European Southern Observatory

#ESOJOBS
eso.org/studentship

ESO Headquarters, Garching near Munich, Germany
ESO Vitacura, Santiago, Chile

Application deadline: 31 May and 30 November, each year

COSMOLOGY

Quantifying hidden massive red galaxies at $z > 3$

Belén Alcalde Pampliega

European Southern Observatory (ESO), Chile

Understanding when and how galaxies assemble is essential to unveil the complete picture of galaxy formation and evolution across the history of the Universe. In the local Universe, the gigantic massive ellipticals are thought to represent one of the most mature stages of galaxy evolution. Those massive systems seem to have formed at early times and through violent and rapid processes [1, 2]. In the last decade, deep observations have also revealed a population of remarkably dense massive ($M_* > 10^{10-11}M_\odot$) quiescent galaxies at $z > 2-3$ [3, 4] whose progenitors formed the bulk of their stars in luminous starbursts at $z > 4$ [5, 6, 7]. The existence of massive evolved systems at $z > 3$ has been recently spectroscopically confirmed [8, 9, 10]. In this sense, analyzing and quantifying the number density of massive galaxies that were already in place at early epochs can help us understand when those systems first appeared and how did they evolve.

Unveiling a new population of galaxies

The most complete currently available catalogs (e.g., CANDELS or 3D-HST) are built from UV/optical selected samples, which are biased against massive red (dusty or evolved) systems. Consequently, they are missing a substantial population of IR-bright but optically faint sources that are not detected even in the deepest HST images.

With the goal of complementing the deepest NIR-selected catalogs available in GOODS (CANDELS & 3D-HST), we conducted a comprehensive search of this elusive massive population at $z > 3 - 4$, first presented in [11]. Specifically, we found 33 Balmer Break galaxies (BBGs, also referred to as optically faint or HST-dark galaxies) selected as Spitzer/IRAC bright ([3.6] & [4.5] < 24.5 mag), H-band dropouts ($H > 26.5$ mag). We note that the luminosity in the 3.6 and 4.5 μm IRAC bands is a robust and unbiased proxy of the total stellar mass.

The nature of massive (red) galaxies at $z > 3$

To better understand the nature of this new population, we analyze the optically faint BBGs by comparing them with a mass-limited ($M_* > 10^{10}$ $M_\odot$ and $z > 3$) sample and a color-selected ($H - [3.6] > 2.5$ mag) sample extracted from the CANDELS catalogs published for these fields.

As BBGs can be considered a continuation of the color-selected sample (if the selection was based on IRAC instead of F160W), their derived mass ($M_* > 10^{10}M_\odot$) and redshift ($z > 3$) distribution help us demonstrate that our color cut (implied in the H-band dropouts) translates into a mass and redshift selection.

From the Spectral Energy Distribution (SED) modelling, we find a strong evidence that massive red galaxies at $z = 3 - 6$ span a diverse range in stellar population properties. In order to explore those different star formation modes, we classify BBGs, according to their

location with respect to the main sequence of star forming galaxies (MS) into Starburst (18%), MS (48%) and subMS (34%) galaxies (see Fig. 1).
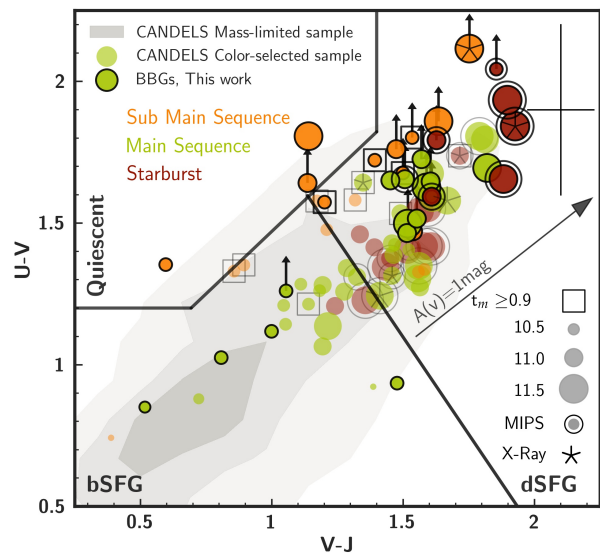
Figure 1: Plot from [11] showing the rest-frame U-V vs. V-J colors for BBGs and the CANDELS color-selected comparison sample color-coded by star formation modes and sized by stellar mass. The upper boundary (black wedge) separates quiescent galaxies (top left) from star forming galaxies (SFGs, bottom). The black diagonal line denotes an additional criterion to separate blue (bSFG) from dusty (dSFG) star-forming galaxies.

Subdividing BBGs by their rest-frame UVJ colors (Fig. 1), we also find a wide variety of systems. While it is true that the vast majority ($\sim$80%) of this optically faint population do correspond to dusty star-forming galaxies (dSFGs), some of which might be hosting AGNs in their center, $\sim$10% correspond to blue star-forming galaxies (bSFGs) and the rest to quiescent galaxies. Although a few recent studies have also revealed a non-negligible number of objects consistent with being either post-starburst or quiescent systems [e.g., 10, 12] at that epoch, only 3 of our BBGs lie within the quiescent wedge and 3 more BBGs have mass-weighted ages that are old enough ($t_m > 0.9$ Gyr, symbols enclosed by a black square in Fig. 1) to be consistent with evolved galaxies.

The role of BBGs in galaxy evolution

The abundance of this hidden population of massive red high-z galaxies is particularly relevant in the high mass end of the galaxy stellar mass function. Indeed, BBGs account for 30-40% of the known galaxies with $M_* > 10^{11}M_\odot$ at $4 < z < 7$ (Fig. 2). The derived number density ($\approx 10^{-5}$ Mpc^{-3}) of massive ($M_* > 10^{11}M_\odot$) galaxies in the early Universe is extremely challenging for the most advanced galaxy formation models and state-of-the-art

hydrodynamical simulations such as EAGLE [13] or Illustris [14], which struggle to reproduce the formation of galaxies with more than $10^{11} M_\odot$ in the first 2 Gyr of the Universe (Fig. 2). In fact, our results point out that 1 of every 30 massive ($M_* > 10^{11} M_\odot$) galaxies in the local Universe was assembled in the first 1.5 Gyr after the Big Bang.

These discrepancies between models and observations, even though the reason is unclear, suggest that a major revision of the formation and evolutionary mechanisms that yield to the built-up of galaxies is required.
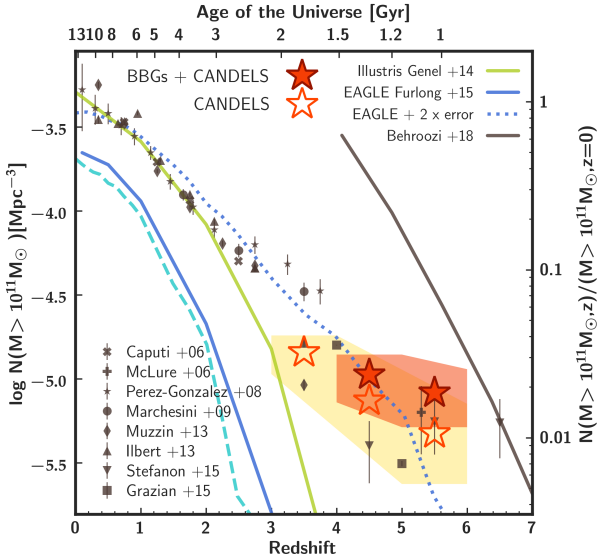
Figure 2: Evolution of the number density of massive ($M_* > 10^{11} M_\odot$) galaxies with redshift (bottom axis) and the corresponding age of the Universe (top axis). The fraction of the local number density is also shown in the secondary vertical axis. The values inferred from the CANDELS sample and those including the BBGs are shown with empty and filled red stars respectively. The blue and green lines show the number density predicted by EAGLE and Illustris simulations.

Conclusions & outlook

We have presented the detection and analysis of a new population of previously unknown optically faint massive red galaxies and gathered a more complete sample of the general population of massive galaxies at $z > 3$.

Although the existence of optically faint objects has been known for a decade [15, 16], only recently several studies, have provided evidence of their ubiquitous existence [11, 17, 18, 19, 20, 21, 22, 23, 26].

As a consequence of their highly obscure nature, optically faint galaxies were initially thought to be classical sub-mm galaxies (SMGs, [24, 25, 26, 27]). However, as

demonstrated in [18], most of them are much fainter at 870 μm (median $S_{870\mu m} \sim 1.6$ mJy) than extreme starburst and SMGs. In addition, they do not represent a homogeneous population, but a variety of transitional evolutionary states instead [11] – see also Fig. 1.

The existence of this numerous population of massive galaxies at high redshifts, which may correspond to the progenitors of the most massive local galaxies, represents a challenge for state-of-the-art simulations which fail to reproduce their number densities.

In order to properly constrain and improve galaxy formation models, accurately accounting for the tail of massive galaxies at $z > 4$ becomes vital. The main source of uncertainty of the observationally derived number density and physical properties is the lack of spectroscopic confirmation of these sources. Given their extreme faintness in the optical/NIR regime ($H > 26.5$ mag), ground-based spectroscopy remains extremely challenging. In this sense, ALMA will be crucial to first confirm their redshift and then constrain the amount of dust and gas in these systems, as well as discriminating between dust-enshrouded star formation and obscured AGN activity. Imaging in near- and mid- infrared wavelengths together with spectroscopy from the JWST will be also essential to understand their nature and characterize their star formation histories.

References

[1] Thomas, D., et al. 2005, ApJ, 621, 673
[2] Saracco, P., et al. 2020, ApJ, 905, 40
[3] Marchesini, D., et al. 2010, ApJ, 725, 1277
[4] Straatman, C. M. S., et al. 2014, ApJl, 783, L14
[5] Daddi, E., et al. 2004, ApJ, 617, 746
[6] Kriek, M., et al. 2009, ApJ, 700, 221
[7] Toft, S., et al. 2014, ApJ, 782, 68
[8] Marsan, Z. C., et al. 2015, ApJ, 801, 133
[9] D'Eugenio, C., et al. 2020, ApJl, 892, L2
[10] Forrest, B., et al. 2020, ApJ, 903, 47
[11] Alcalde Pampliega, B., et al. 2019, ApJ, 876, 135
[12] Schreiber, C., et al. 2018, A&A, 611, A22
[13] Furlong, M., et al. 2015, MNRAS, 450, 4486
[14] Genel, S., et al. 2014, MNRAS, 445, 175
[15] Huang, J. S., et al. 2011, ApJl, 742, L13
[16] Caputi, K. I., et al. 2012, ApJl, 750, L20
[17] Wang, T., et al. 2016, ApJ, 816, 84
[18] Wang, T., et al. 2019, , 572, 211
[19] Yamaguchi, Y., et al. 2019, ApJ, 878, 73
[20] Williams, C. C., et al. 2019, ApJ, 884, 154
[21] Romano, M., et al. 2020, MNRAS, 496, 875
[22] Smail, I., et al. 2021, MNRAS, 502, 3426
[23] Talia, M., et al. 2021, ApJ, 909, 23
[24] Weiss, A., et al. 2013, ApJ, 767, 88
[25] Strandet, M. L., et al. 2016, ApJ, 822, 80
[26] Franco, M., et al. 2018, A&A, 620, A152
[27] Zavala, J. A., et al. 2017, MNRAS, 464, 3369

Short CV

2011–2013:	Master in Astronomy, UCM & UAM, Spain
2013:	AAO research fellowship, Sydney, Australia
2013–2014:	ESA young graduate trainee at ESAC, Madrid, Spain
2016:	FPI-MINECO predoctoral research stay fellowship, UC Berkeley, USA
2018–2019:	ING Student fellowship (INT Support astronomer), La Palma, Spain
2014–2020:	PhD in Astronomy, FPI-MINECO fellowship, UCM, Madrid, Spain
2020–present:	ESO/ALMA Fellow, Santiago de Chile, Chile

Cosmic dissonance: new physics or systematics behind the Hubble tension?

Nikki Arendse

DARK, Niels Bohr Institute, University of Copenhagen

The Hubble tension

The Hubble constant (H_0) is a fundamental cosmological parameter that determines the expansion rate of the Universe in the past, present and future. Additionally, it is an essential quantity for calibrating the cosmic distance scale and calculating the age of the Universe. Despite its importance in cosmology, its value is a matter of strong debate. Local determinations of the Hubble constant using Cepheids and type Ia supernovae find $H_0 = 73.2 \pm 1.3$ km s^{-1} Mpc^{-1} [1], while observations from the cosmic microwave background (CMB) radiation obtain $H_0 = 67.4 \pm 0.5$ km s^{-1} Mpc^{-1} [2]. This difference is one of the most outstanding problems in present-day cosmology and is often referred to as the *Hubble tension*. The discrepancy might be explained by some residual systematics in any of the measurements, but it also questions our understanding of the Universe. Since the CMB-based method needs a cosmological model to extrapolate the parameters measured at recombination to redshift zero, it uses the standard ΛCDM model. In other words, if the true underlying cosmology deviates from ΛCDM, this might explain why the CMB measures a different H_0 than local measurements.

The main question that I will answer in this proceeding is the following: *Can modifications of ΛCDM solve the Hubble tension?* The results and conclusions presented here are from [3].

The importance of the sound horizon

Contrary to what the name might suggest, the Hubble tension is about more than just H_0. Another important cosmological parameter that we focus on in our work is the sound horizon (r_d). The sound horizon characterizes a distance scale in the early Universe, when the baryons and photons where trapped in a primordial plasma. Any over-densities in the plasma would lead to gravitational collapse, as well as a radiation pressure directed outwards. The counteracting forces of gravity and pressure resulted in oscillations, very similar to sound waves. The sound horizon constitutes the maximum distance the sound waves have travelled before the Universe became transparent at the epoch of recombination.

Today, we can still observe this characteristic scale in the distribution of galaxies and clusters, as more structures have formed at a separation of r_d. Baryon Acoustic Oscillation (BAO) measurements use the clustering of galaxies to extract this feature. By comparing the radius of the sound horizon at recombination to the sound horizon at lower red-shifts, the product of $H_0 \times r_\mathrm{d}$ can be constrained. Therefore, the Hubble tension is just as much a tension in the sound horizon. Measurements of the CMB find a low H_0 and a high r_d, while several local measurements obtain a high H_0 and a low r_d.

Data sets

In our work, we employ observations of type Ia supernovae (SNe) and BAO as relative distance measurements. These probes can be calibrated by absolute distance measurements of Cepheid variable stars, as carried out by the *Supernovae and H_0 for the Equation of State of dark energy* project (SH0ES; [1]), or from stars at the Tip of the Red Giant Branch (TRGB), obtained by the Carnegie-Chicago Hubble Program (CCHP; [4]). However, Cepheids and TRGB stars can only be observed at low red-shifts. For that reason, we are using an additional calibration from gravitationally lensed quasars, as measured by the H_0 *Lenses in COSMOGRAIL's Wellspring* collaboration (H0LiCOW; [5]). By measuring the time-delays between brightness fluctuations of the multiple images of the quasar, absolute distances between the observer, lens galaxy and the quasar can be determined. The advantage of lensed quasars is that they allow for a calibration at higher red-shifts.

Tension between CMB and local observations

Our measurements of the sound horizon are summarized below, together with the CMB constraints by *Planck* for a comparison.

SNe + BAO + H0LiCOW:	$r_\mathrm{d} = 134.2 \pm 4.4$ Mpc
SNe + BAO + H0LiCOW + SH0ES:	$r_\mathrm{d} = 135.1 \pm 2.9$ Mpc
SNe + BAO + H0LiCOW + CCHP:	$r_\mathrm{d} = 139.5 \pm 3.6$ Mpc
CMB (*Planck*):	$r_\mathrm{d} = 147.2 \pm 0.3$ Mpc

When type Ia supernovae and BAO are calibrated by a combination of Cepheid measurements by SH0ES and lensed quasars from H0LiCOW, our combined $H_0 - r_\mathrm{d}$ results are in 5σ tension with observations from the CMB.
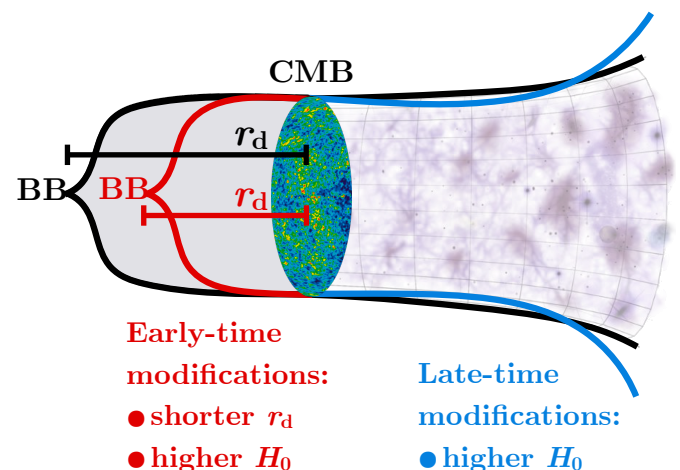

Figure 1: Expansion history of the Universe as predicted by the ΛCDM model (black), early-time modifications (red) and late-time modifications (blue).

However, the tension is lowered considerably if we replace the SH0ES calibration by that of the TRGB by the CCHP collaboration.

Local measurements can be obtained without assumptions about the underlying cosmological model, whereas the CMB analysis require one; hence, they use ΛCDM. This raises the question whether modifications to ΛCDM might be able to shift the CMB results closer to the local ones and reconcile the tension.

Modifications of ΛCDM

Extensions to the standard cosmological model can follow two distinct approaches; they can either change the early-time physics (pre-recombination) or they can change the late-time physics (post-recombination).

Early-time modifications introduce an additional component in the early Universe, such as additional relativistic particles ('dark radiation') or early dark energy, which increases the expansion rate. This reduces the time between the Big Bang and recombination and, in turn, decreases the maximum distance the sound waves could travel before recombination. As such, the radius of the sound horizon is shorter than in the standard ΛCDM scenario. Since we still observe the same angular size of the sound horizon in the CMB power spectrum, this automatically implies a shorter angular diameter distance to the CMB. Shorter distances corresponds to a higher Hubble constant. In this way, early-time modifications alter simultaneously the Hubble constant and the sound horizon.

Late-time modifications, on the other hand, leave the physics before recombination unaltered. Instead, they impose a phase of extra accelerated expansion at later times. This is generally achieved by modifying the dark energy density such that it increases over time, which eventually leads to the 'Big Rip' scenario in which cosmic expansion will rip everything in the Universe apart. On the bright side, this scenario has the potential to solve the Hubble tension by increasing the present-day expansion rate. However, as the physics of the early Universe is unchanged, these models cannot alter the value of the sound horizon.

Figure 1 illustrates how early-time and late-time models change the expansion history of the Universe.

Results

In order to study the effects that modifications of ΛCDM have on the tension, we investigated four models that are commonly used in the literature. Figure 2 shows how the $H_0 - r_{\mathrm{d}}$ contours from the CMB change after applying these models. The early-time models (dark radiation and early dark energy) move both H_0 and r_{d} closer to their local values. Although, in the case of local data calibrated by SH0ES and H0LiCOW measurements, the shift is not sufficient to solve the tension. Late-time extensions (dark

energy models 1 and 2) increase H_0 but are not able to alter the value of r_{d}; they fail to address the combined tension.

Additionally, it has recently been pointed out that both early-time and late-time modifications exacerbate the mild growth tension that exists between CMB and large scale structure measurements.

Conclusions

Returning to the original question; *can modifications of ΛCDM solve the Hubble tension?*

In my opinion, the answer is no. Early-time modifications slightly reduce the tension, but create a new problem when it comes to the growth tension, while late-time modifications fail to address the combined tension completely, since they cannot alter the value of the sound horizon.
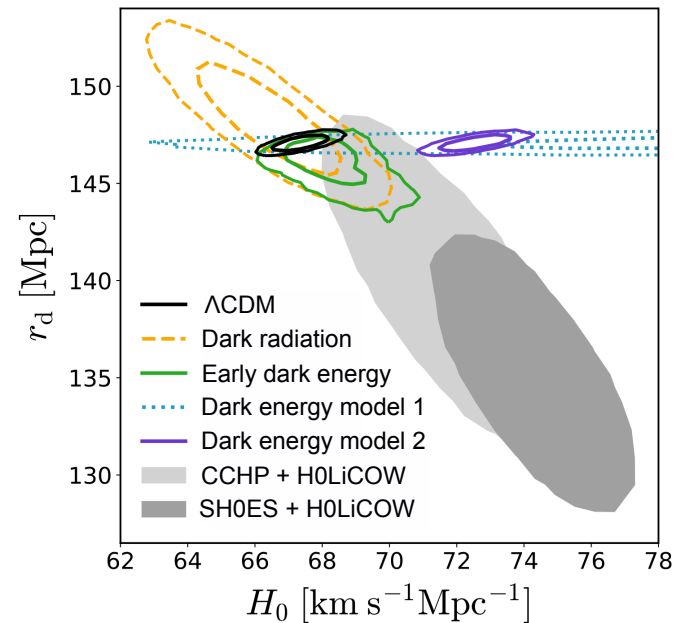
Figure 2: The effects of modifications of ΛCDM (coloured contours) on the CMB observations from *Planck* (black contours). The filled gray contours correspond to the 2σ credibility regions of local observations (SNe + BAO + H0LiCOW + SH0ES/CCHP). Early-time models (dark radiation and early dark energy) shift both H_0 and r_{d} closer to the local values, while late-time models (dark energy models 1 and 2) only change the Hubble constant and, therefore, fail to solve the combined tension. Figure adapted from [3].

References
[1] Riess, A., et al. 2021, M. 1988, ApJ, 908, L6
[2] Planck collaboration, 2020, A&A, 641, A6
[3] Arendse, N., et al. 2020, A&A, 639, A57
[4] Freedman, W., et al. 2021, arXiv e-prints, 2106.15656
[5] Wong, K., et al. 2020, MNRAS, 498, 1420

Short CV

2018: Master in Astronomy, Kapteyn Institute, University of Groningen, The Netherlands
2018–2021: PhD in Astronomy, University of Copenhagen, Denmark

El Gordo: a massive blow to ΛCDM cosmology

Indranil Banik

University of Bonn, Nussallee $14 - 16$, D-53115 Bonn, Germany

University of St Andrews, North Haugh, St Andrews, Fife KY16 9SS, UK

Galaxy clusters are the largest gravitationally bound structures in the Universe. When these structures form is highly dependent on the cosmological model, and thus on the assumed gravitational law. The correct model must be able to statistically predict the cosmological epochs at which different structures can be observed.

In recent years, improvements in the quality and resolution of telescopes have made it possible to observe objects which are very deep in space. The mass and velocity of some of these objects turned out to be significantly higher than what the standard model of cosmology (ΛCDM) predicted. A particularly extreme example of this is the galaxy cluster ACT-CL J0102-4915, also known as "El Gordo".

Figure 1: A composite image showing El Gordo in X-ray light from NASA's Chandra X-ray Observatory (blue), along with optical data (red, green, and blue) from the European Southern Observatory's Very Large Telescope (VLT), and infrared emission from NASA's Spitzer Space Telescope (red and orange). Notice the twin tails towards the upper right. Credits: X-ray: NASA, CXC, Rutgers, J. Hughes et al.; Optical: ESO, VLT and SOAR, Rutgers, F. Menanteau; IR: NASA, JPL, Rutgers, F. Menanteau. Image taken from [3].

El Gordo is an interacting galaxy cluster at redshift $z = 0.87$ composed of two infalling subclusters of total mass $M_{200} \approx 3 \times 10^{15} \, M_\odot$. Other particularities of this cluster are its strong Sunyaev-Zel'dovich (SZ) effect and its strong X-ray luminosity, which is distributed in a single peak and two faint tails (see Figure 1). Both of these suggest that the subclusters are infalling onto each other at a considerable velocity. In our paper "A massive blow for

ΛCDM $-$ the high redshift, mass, and collision velocity of the interacting galaxy cluster El Gordo contradicts concordance cosmology" [1], we statistically quantified how likely it is for this galaxy cluster to arise in the ΛCDM cosmology, and thus whether El Gordo poses a challenge to this model.

Method

In order to find out the likelihood of observing an El Gordo-like object in ΛCDM, we searched for El Gordo analogues in the *N*-body Juropa Hubble Volume (Jubilee[§]) cosmological simulation [2]. With a co-moving simulation volume of $(6 \, h^{-1} \, \text{co-moving Gpc (cGpc)})^3$, Jubilee is one of the largest ΛCDM cosmological simulations available at present. A very large simulation box is needed to search for objects as extreme as El Gordo, but a larger simulation box generally implies a decrease in the resolution. Therefore, we cannot attempt to find analogues to El Gordo that match some of its more detailed properties, e.g. its two-tailed X-ray morphology. However, we can still look for a pair of halos whose mass, mass ratio, and infall velocity could potentially give rise to a structure that reproduces the observed characteristics of El Gordo. That is, we can search for the El Gordo progenitors.

The properties of the El Gordo progenitors had already been investigated in previous studies, which used idealised hydrodynamical simulations to constrain the values of these parameters. In this project, we used the results of [4] as they present one of the most recent and most accurate hydrodynamical simulations of El Gordo. After running 123 simulations for different parameters, these authors concluded that the parameter values of the El Gordo progenitors that provide the best fit to observations are: total mass $M_{\text{tot}} = 3.19 \times 10^{15} \, M_\odot$, mass ratio 3.6, and infall velocity $V_{\text{infall}} = 2500$ km/s.

Statistical analysis

We compared all infalling pairs of halos identified in the Jubilee simulation at $z = 1$ (since we are looking for analogues to the El Gordo progenitors, the redshift at which we search for them must be slightly higher than that at which El Gordo is observed). We chose as analogues those pairs which match the properties of mass ratio and infall velocity constrained by [4]. There are no cluster pairs in the Jubilee simulation which are massive enough to match the estimated total mass of El Gordo, so we inferred the number of El Gordo analogues by extrapolating the mass function of lower mass 'analogues' which satisfy the other criteria. To obtain the redshift dependence, we repeated the same procedure for red-shifts $z = 0.5$ and $z = 0$. After taking into account that the volume in which El Gordo was first observed is significantly smaller than the Jubilee simulation box, we were able to obtain
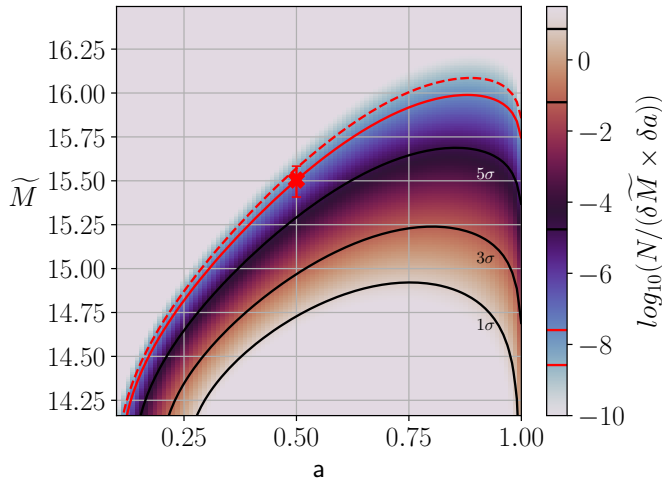
14

Figure 2: Plot showing the probability of finding El Gordo progenitors in the ΛCDM model at each position in the grid, which we constructed for many values of the cosmic scale factor a (x-axis) and total mass in $\log_{10}$ scale (y-axis). The point in the grid corresponding to the $\widetilde{M}$ and a values of the El Gordo progenitors is marked with a red X. Observing an even more extreme pair has a probability of 7.51×10^{-10} (6.16σ), the total probability beyond the solid red contour. Reproduced from Fig. 7 of [1].

the probability of observing an El Gordo-like structure with the observed total mass and cosmic scale factor $a \equiv 1/(1+z)$ (see Figure 2).

Results

The results of our statistical analysis show that the probability of observing an object as extreme as El Gordo in the survey volume in which it was originally found is 7.51×10^{-10} (6.16σ) in the ΛCDM cosmology. The probability is even lower if we account for the fact that other problematic objects for ΛCDM have also been observed, e.g. the Bullet Cluster. From the statistical analysis of [5], we inferred that the probability of observing the Bullet Cluster in its survey region is 5.40×10^{-3} (2.78σ). Combining the probability of having found both El Gordo and the Bullet Cluster in their respective survey regions, we obtained that ΛCDM is in 6.43σ tension with observations.

We considered several possibilities that might alleviate this tension. A lower mass and/or velocity could increase the probability of finding analogues in the ΛCDM cosmological simulation, but the parameters have to be consistent with the high luminosity and brightness observed for El Gordo, which imply a very energetic interaction between its two subclusters. After repeating the

analysis for lower masses and velocities, we found that ΛCDM is still in $> 5\sigma$ tension for every plausible mass and velocity. Another possibility is that the statistics obtained from the Jubilee simulation could be uncertain due to Poisson noise, but this seems unlikely as the mass function that we got from Jubilee is based on 15035 pairs, making the Poisson noise extremely small. We also considered if a different fit to the mass function could significantly affect the final result, but after testing several different fits, we concluded that the results are not greatly affected by this.

El Gordo in νHDM

In light of our results, we conclude that the observations of very large and/or high velocity clusters at high redshift − such as El Gordo and the Bullet Cluster − cannot be explained in a ΛCDM context. Because of this, we propose an alternative cosmological model in which these observations can be explained naturally: the neutrino-Hot Dark Matter (νHDM) model [6, 7]. This model assumes MONDian gravity [8] and sterile neutrinos as hot dark matter. In MOND, there is an enhancement to Newtonian gravity at accelerations below $a_0 = 1.2 \times 10^{-10}$ m/s^2. Therefore, νHDM predicts that smaller structures assembled together to form larger structures faster than in ΛCDM. [9] performed a series of cosmological simulations using the νHDM model to examine the formation of galaxy clusters. In their $\left(0.512\ h^{-1}\ \text{cGpc}\right)^3$ simulation box, they found about 1 El Gordo analogue, which corresponds to 1.16 analogues in the survey volume. Thus, νHDM predicts the right order of magnitude for the number of El Gordo-like objects that should be observed in the surveyed region.

Conclusions

The model parameters of the El Gordo progenitors obtained from the hydrodynamical simulations of [4] contradict ΛCDM at 6.16σ based on the Jubilee cosmological simulation. The tension rises to 6.43σ if we also consider the Bullet Cluster, even before considering other known extreme objects. However, El Gordo can be naturally explained in the νHDM cosmological model.

References

[1] Asencio, E., et al. 2021, MNRAS, 500, 5249
[2] Watson, W.A., et al. 2013, MNRAS, 433, 1230
[3] NASA mission pages: Chandra, accessed: 15/08/2021
[4] Zhang, C., et al. 2015, ApJ, 813, 129
[5] Kraljic, D. & Sarkar, S. 2015, JCAP 04, 050
[6] Angus, G.W. 2009, MNRAS, 394, 527
[7] Haslbauer, M., et al. 2020, MNRAS, 499, 2845
[8] Milgrom, M. 1983, ApJ, 270, 365
[9] Katz, H., et al. 2013, ApJ, 772, 10

Short CV

2010: Undergraduate and Master, Cambridge, UK
2014: PhD, St Andrews, UK
2018: Humboldt Fellow, Bonn, Germany
2021: Postdoc, St Andrews, UK

Calibrating the Cepheid distance scale with Gaia

Louise Breuval

LESIA, Observatoire de Paris, Meudon, France

Cepheids are pulsating variable stars which play a key role as primary distance indicators thanks to the empirical relation between their pulsation period and intrinsic luminosity, the period-luminosity (PL) relation (or Leavitt law [1]). This law is used to calibrate the brightness of type-Ia supernovae (SNe Ia) in nearby galaxies, which is in turn used to measure the distance to galaxies in the Hubble flow. This provides an estimate of the current expansion rate of the Universe, the Hubble constant (H_0). In recent years, a significant tension of at least 4σ has arisen between the early universe measurement of H_0 from the Planck satellite, assuming a ΛCDM model [2], and the late universe direct measurements based on Cepheid distances [3]. The persistence of this tension would imply new physics beyond the standard model of cosmology: it is therefore critical to improve the period-luminosity calibration with precise and reliable Cepheid distance measurements.

Calibration of the PL relation with *Gaia* parallaxes

The *Gaia* mission is dedicated to measure the distance to more than 1.5 billion stars using the method of the parallax and constitutes an essential tool for the calibration of the PL relation. However, Cepheid parallaxes suffer from several systematic effects. *Gaia* Data Release 2 (DR2) parallaxes are subject to a zero-point offset which value is debated. Additionally, Cepheids undergo color changes during their pulsation cycle which produces additional noise in the astrometric data. Finally, the brightness of Cepheids often results in the saturation of the detectors and therefore in unreliable parallaxes for a large number of these stars.

In order to overcome these issues, we proposed an original approach based on companion stars and open clusters hosting Cepheids [4]. The astrometric solution of fainter and stable neighbour companions of Cepheids are more reliable than that of their parent variable star. Open clusters are also interesting for similar reasons: their numerous member stars allow us to derive an average value of the cluster parallax, which provides an alternative way to measure a precise distance to the Cepheids they host. In [4], we assumed a *Gaia* DR2 parallax zero-point of -0.046 $\pm$ 0.015 mas, which covers most of the estimates from the literature, and we adopted the *Gaia* DR2 parallaxes of 22 Cepheid companions and 14 open clusters hosting Cepheids to calibrate the PL relation in the optical and near-infrared (NIR). The dispersion of the PL relation obtained with this method is significantly reduced compared with using directly the *Gaia* DR2 parallaxes of Cepheids.

Recently, more precise parallaxes were published in the *Gaia* Early Data Release 3 (EDR3). The parallax zero-point can be estimated for each star individually and takes into account the magnitude, the color and the position of the sources. Moreover, the longer time coverage of *Gaia* EDR3 seems to reduce the contamination of the astrometry due to variability that was present in *Gaia* DR2. In [5], I concluded that Cepheid parallaxes are more reliable in *Gaia* EDR3 than in *Gaia* DR2, and even more precise on average than companions which are sometimes very faint. On the other hand, the precision reached with *Gaia* EDR3 for mean cluster parallaxes is twice better than individual Cepheid parallaxes: clusters are therefore excellent substitutes to Cepheids for measuring their distance (see Figure 1).
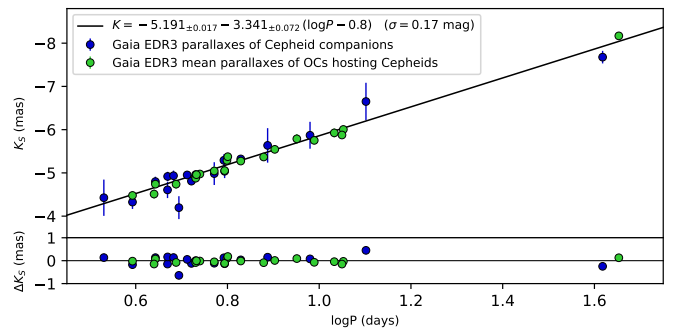
Figure 1: PL relation in the K_S band based on *Gaia* EDR3 parallaxes of companions and open clusters [5].

The PL relation has direct consequences on the Hubble constant since it is applied to calibrate SN Ia luminosities in nearby galaxies, which are in turn used to derive the distance to remote galaxies at large red-shifts. In [5], I replaced the previous HST and *Hipparcos* parallaxes used in [6] by our sample of *Gaia* EDR3 parallaxes of companions and host open clusters. I re-evaluated the initial Hubble constant of 76.18 $\pm$ 2.37 km/s/Mpc obtained by [6] and anchored to the Milky Way to a revised value of 73.47 $\pm$ 1.77 km/s/Mpc. This result is lower than the original value but is also in better agreement with other estimates based on water masers in NGC 4258 and detached eclipsing binaries in the LMC and in M31 from [6].

Influence of metallicity on the PL relation

It has been demonstrated that the chemical composition of Cepheids impacts their intrinsic brightness. Therefore, the difference in Cepheid metallicity between galaxies in which the PL relation is calibrated and the galaxies hosting SNe Ia must be taken into account by including a corrective term in the PL relation.

To measure this effect, we compared the Leavitt law in the Milky Way, where Cepheids are metal-rich ([Fe/H] $\approx$ +0.08 dex), with the PL relation in the LMC and SMC where Cepheids are more metal-poor than in our galaxy

([Fe/H] $\approx$ -0.34 dex and [Fe/H] $\approx$ -0.75 dex respectively). In the Milky Way, we adopted the *Gaia* EDR3 parallaxes corrected for the zero-point offset. We also applied a quality selection based on the RUWE parameter provided in the *Gaia* catalog. For the Magellanic Clouds, we adopted the distances recently measured by [10] and [11] with a remarkable precision using late-type detached eclipsing binaries. We slightly corrected these distances to take into account the inclination of the LMC and SMC and therefore used individual distances to Cepheids depending on their position in the Clouds. In order to avoid the presence of outliers, we only select Cepheids within a radius of 3 degrees around the LMC center and 0.6 degree around the SMC center. For the SMC especially, which has a very elongated shape, it is not to exclude that Cepheids could appear projected along the line of sight but are actually located at shorter distance: these stars are identified by a larger dispersion with respect to the PL relation and are excluded by the application of a $\sigma-$clipping procedure.

Apparent mean magnitudes are derived from well covered light curves and are corrected for the extinction. By applying a Monte Carlo simulation to the PL calibrations in the three galaxies, we derived that metal-rich Cepheids are intrinsically brighter than metal-poor ones. This is equivalent to including a negative metallicity term γ in the Leavitt law. The metallicity effect in the V, I, J, H and K_S bands is represented as a function of wavelength in Figure 2.
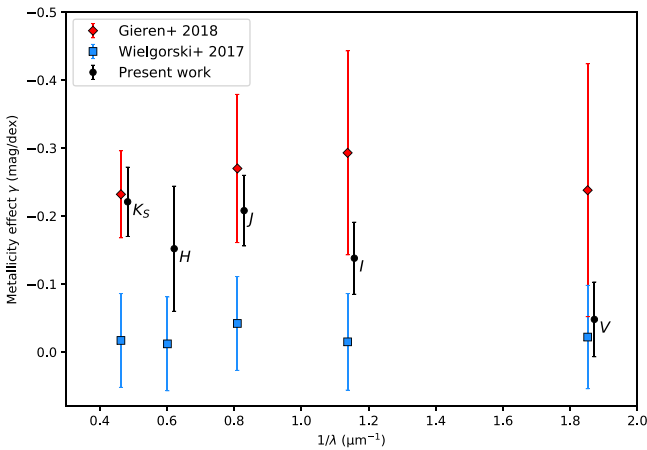

Figure 2: Metallicity effect as a function of wavelength and comparison with the literature [8, 9].

The results of this analysis are presented in [7]. In the near infrared (NIR), we find a significant metallicity effect with γ_K = -0.221 $\pm$ 0.051 mag/dex. In the opti-

cal, it is also negative but weaker with γ_V = -0.048 $\pm$ 0.055 mag/dex. Our results agree well with the Baade-Wesselink analysis carried out by [8], although they derived a stronger metallicity effect in the optical and generally larger error bars. On the other hand, [9] obtained a metallicity effect consistent with zero and independent of the wavelength, based on a purely differential analysis between the LMC and SMC Leavitt law.

A slight trend is visible in our values represented in Figure 2, which suggests that the metallicity effect is stronger (in absolute sense) in the NIR than in the optical. This trend should be confirmed by studying the metallicity effect on a wider range of wavelengths, including more bands such as *Gaia* optical bands and *Spitzer* mid-infrared bands (see also [5]).

Perspectives

This study shows that the calibration of the Cepheid PL relation, although improved in the recent years, still needs to be refined, and that several systematic effects must be better understood to overcome the remaining uncertainties in the extragalactic distance scale. The publication of the next *Gaia* data releases should considerably improve the calibration of the Leavitt law by providing a better estimation of the parallax zero-point and by including a correction for the color variation that affects Cepheids. Precise metal abundance measurements for Galactic as well as Magellanic Cloud Cepheids are paramount, since most studies still rely on mean metallicities in the three galaxies, due to the lack of precision of the current individual measurements. Cepheids in Open Clusters are very promising thanks to their precise average parallax: this sample will be observed in the HST system for consistency with the measurements of extragalactic Cepheids in SNe Ia hosts, which should considerably reduce the systematics related to the photometric zero-points. Finally, the upcoming launch of the JWST is expected to resolve the crowding around extragalactic Cepheids, which will again help reduce the systematics and approach a 1% precision on the Hubble constant.

References

[1] Leavitt, H. S., & Pickering, E. C. 1912, Harvard College Observatory Circular, 173, 1
[2] Planck Collaboration et al. 2020, A&A, 641, A6
[3] Riess, A. G., et al. 2021, ApJ, 908, L6
[4] Breuval, L., et al. 2020, A&A, 643, A115
[5] Breuval, L., PhD thesis 2021, PSL University, Paris
[6] Riess, A. G., et al. 2016, ApJ, 826, 56
[7] Breuval, L., et al. 2021, ApJ, 913, 38
[8] Gieren W., et al. 2018, A&A, 620, A99
[9] Wielgórski, P., et al. 2017, ApJ, 842, 116
[10] Pietrzyński, G., et al. 2019, Nature, 567, 200
[11] Graczyk, D., et al. 2020, ApJ, 904, 13

Short CV

2018: Master in Astronomy & Astrophysics, Paris Saclay University, France
2021: PhD in Astronomy & Astrophysics, Paris Observatory, France
2022: Postdoctoral researcher, Johns Hopkins University, Baltimore, USA

Clash of giants - Radio emission from merging galaxy clusters

Virginia Cuciti

Hamburger Sternwarte, Universität Hamburg, Gojenbergsweg 112, 21029, Hamburg, Germany

In the present scenario of structure formation of the Universe, galaxy clusters form via hierarchical merger of smaller structures along the filaments of the cosmic web. Galaxy clusters mergers are the most energetic events in the Universe, releasing up to 10^{63} erg in 1 Gyr timescale. This energy is dissipated through the cluster's volume via shocks and turbulence, heating the intra cluster medium (ICM). Part of this energy is also channelled into the acceleration of particles and the amplification of magnetic fields. The most spectacular evidence of these non-thermal phenomena in the ICM is observable in the radio band in form of gigantic (1 Mpc scale) diffuse sources, called radio halos [1] .

According to the most favoured scenario, radio halos form when turbulence, induced in the ICM during merger events, accelerates cosmic ray electrons [2]. In this framework, the radio spectra of radio halos are expected to show a cutoff at a frequency that is proportional to the energy budget available in the merger event. Therefore massive systems undergoing major mergers are expected to form radio halos visible up to $\sim$ GHz frequencies, while less massive systems and minor mergers are expected to form the class of ultra steep spectrum radio halos (USSRHs), only visible at $\sim$ 100 MHz or below [3]. This allows us to derive some basic predictions on the statistical properties of radio halos:
- Radio halos should be predominantly found in merging clusters.
- The radio power of radio halos should correlate with the mass of the host clusters.
- Radio halos should be more powerful in more dynamically disturbed clusters.
- The fraction of radio halos should increase with the mass of clusters.
- The fraction of radio halos should increase at low frequency, because of the existence of USSRHs.

Radio halos: state of the art

The above mentioned expectations can be tested with radio and X-ray observations of large samples of galaxy clusters. In this respect, a lot of effort has been made in the past decades, mostly with observations at $\sim$ GHz frequencies [4, 5, 6, 7]. Here I outline the most recent results on the observed statistical properties of radio halos aimed at addressing the points listed in the previous section. These results are based on a mass-selected sample of galaxy clusters with $M_{500} > 6 \times 10^{14} M_\odot$ and $z = 0.08 - 0.33$ observed at frequencies > 600 MHz [8, 9, 10].
• We used archival X-ray Chandra data, available for the great majority of the clusters, to infer their dynamical state. We found that more than the 90 % of radio halos in this sample are in merging clusters, confirming the
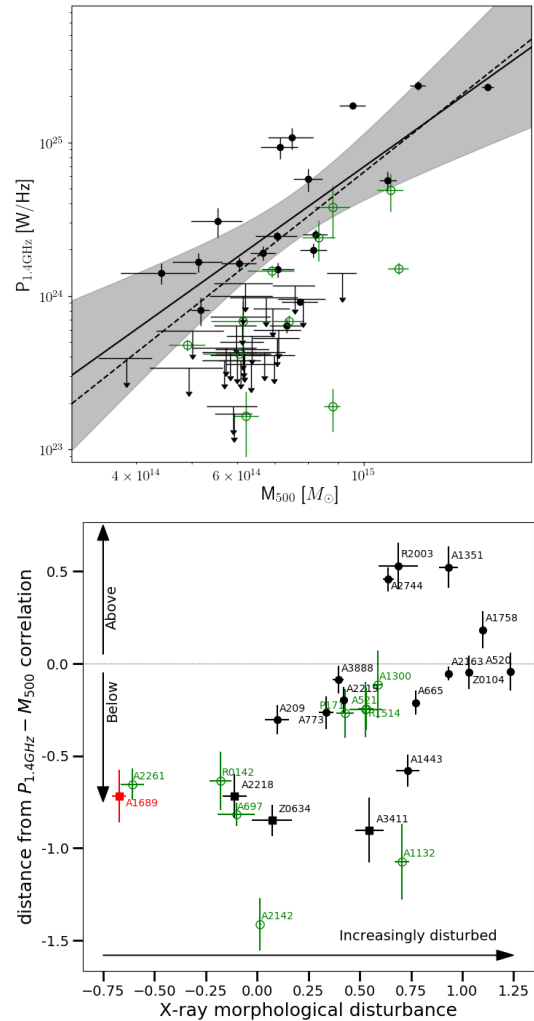
Figure 1: Top: Radio power–mass diagram. The solid line represents the best fit relation to radio halos only and the shadowed area is the 95% confidence interval region. Bottom: distance from the radio power – mass correlation versus dynamical disturbance. In both panels, green empty circles represent USSRHs. Figures adapted from [10]

hypothesis that merger events play a crucial role in the formation of radio halos.
• The existence of a correlation between the radio power of radio halos and the mass of the host clusters is confirmed with unprecedented statistics (Figure 1, top panel) and the radio power of clusters without radio halos (upper limits) is well below the correlation.
• The correlation shows a relatively large scatter, which may reflect the complex mixture of different evolutionary phases during the clusters' life time. The idea is that the radio emission of clusters evolves in time according to their dynamical history: relaxed clusters lay in the region of the upper limits, when a merger event occurs,

the radio halo lights up and the cluster migrates up to the correlation. After ~ 1 Gyr, the cluster appears dynamically relaxed again, the radio emission fades away and the cluster goes back to the upper limits region. In agreement with this picture, we found a trend between the distance from the correlation and the dynamical disturbance of galaxy clusters, i.e. more powerful radio halos are found in the most disturbed clusters (Figure 1, bottom panel).

• This sample allowed us to show for the first time that the fraction of radio halos drops in low mass systems, in agreement with the turbulent acceleration model (Figure 2).
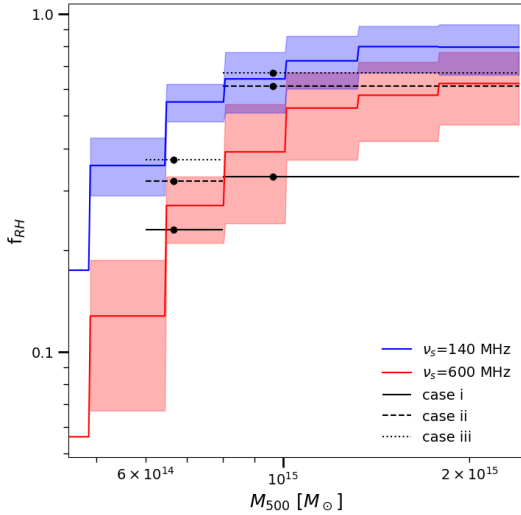

Figure 2: Expected fraction of cluster with radio halos as a function of the cluster mass with cutoff frequency 600 MHz (red line and shadowed region) and 140 MHz (blue line and shadowed region). The black lines represent the observed fraction of radio halos in two mass bins: the low mass ($M_{500} < 8 \times 10^{14} M_\odot$) and the high mass bin ($M_{500} > 8 \times 10^{14} M_\odot$). Figure adapted from [10].

The statistical studies of radio halos have remained limited so far to massive clusters ($M_{500} > 5-6 \times 10^{14} M_\odot$) and high observational frequencies. This does not allow us to test the most important prediction of models, i.e. the existence of a population of USSRHs only detectable at low frequency and the consequent increase of the fraction of halos that should be seen in samples observed at low frequencies.

The LOFAR revolution

In order to overcome the current limits and be able to test the most important expectation of the turbulent re-acceleration model, sensitive low frequency observations are necessary. To date, the Low Frequency Array (LOFAR, [12]) is the best instrument to perform such a test. The main reasons are the high sensitivity to the extended emission, combined with the high resolution, needed to disentangle the contribution of discrete sources blended with radio halos. Not only LOFAR is allowing the exploration of a new frequency window (10-240 MHz), but it is also allowing us to probe new cluster mass ranges (down to $M_{500} > 1 \times 10^{14} M_\odot$), where the majority of USSRHs should be found.

Using the data from the LOFAR Two Meter Sky Survey (LoTSS, [13]) we are carrying out the first systematic study of radio halos at 150 MHz. Specifically, we analysed the radio images of all the 309 Planck clusters [11] within the LoTSS data release 2 (Shimwell et al. in prep.) in order to search for diffuse emission. These clusters span a large redshift ($z = 0.016 - 0.9$) and the mass range ($M_{500} = 1 - 12 \times 10^{14} M_\odot$). We identified ~ 80 radio halos (Botteon et al., in prep.). This is the largest sample of galaxy clusters observed at low frequency and the largest sample of radio halos analysed so far. The statistical exploitation of these data is ongoing (Cuciti et al., in prep., Cassano et al., in prep.). This unique sample will allow us to 1) extend previous studies to lower mass ranges and higher redshift, where we expect to find the majority of USSRHs; 2) measure the occurrence of radio halos at low frequency and compare it with the results obtained at high frequency; 3) study the radio power – mass correlation at low frequency and down to low masses. This work, combined with higher frequency (GMRT and VLA) follow ups that are already ongoing will allow us to perform the first statistically solid study of the spectral behaviour of radio halos, providing the missing and crucial test for current models, together with new constraints for the development of future more sophisticated models and simulations.

References
[1] van Weeren, M.P., et al. 2019, Space Sci. Rev., 215, 16
[2] Brunetti, G., et al. 2001, MNRAS, 320, 365B
[3] Cassano, R., & Brunetti, G., 2005, MNRAS, 357, 1313
[4] Venturi, T., et al. 2007, A&A, 463, 937
[5] Venturi, T., et al. 2008, A&A, 484, 327
[6] Cassano, R., et al. 2013, ApJ, 777, 141
[7] Basu, K. 2012, MNRAS, 421, L112
[8] Cuciti, V., et al. 2015, A&A, 580, A97
[9] Cuciti, V., et al. 2021, A&A, 647A, 50C
[10] Cuciti, V., et al. 2021, A&A, 647A, 51C
[11] Planck Collaboration, 2016 A&A, 594A, 27P
[12] van Haarlem, M.P., et al. 2013, A&A, 556, A2
[13] Shimwell, T. W., et al., 2019, A&A, 622A, 1S

Short CV

2011:	Bachelor degree in Astronomy, University of Bologna, Italy
2014:	Master's degree in Astrophysics and Cosmology, University of Bologna, Italy
2018:	PhD in Astrophysics, University of Bologna, Italy
2018–2020:	Postdoc at the Observatory of Hamburg, Germany
2020–present:	Alexander von Humboldt Fellow at the Observatory of Hamburg

The panchromatic view of galaxy build-up in the first 2 Gyr of cosmic history

Yoshinobu Fudamoto

National Astronomical Observatory of Japan

Waseda University

Over the past decades, several important steps have been taken to understand the formation and evolution of first generations of galaxies. Thanks to deep multi-wavelength observations by Hubble Space Telescope (HST), studies of early galaxies have now been pushed well into the Epoch of Reionization, i.e. up to $z \sim 10 - 11$ only $500\,\mathrm{Myr}$ after the Big Bang [1, 2, 3]. However, our current knowledge beyond $z \sim 2 - 3$ is significantly biased to the rest-frame ultraviolet observations as it's only accessible by deep optical/near-infrared observations, and dust-obscured properties of high-redshift galaxies have remained mostly unknown. This situation was revolutionized by extremely sensitive and high-resolution far-infrared (FIR) interferometers such as ALMA and NOEMA. First ALMA observations showed us surprises by finding fainter FIR emission than expected from low-redshift galaxy observations, suggesting an evolution of dust-obscured galaxy properties at high-redshift[4, 5]. To understand this potential evolution with statistical samples and with a wide range of galaxy parameters, large ALMA observations were required. In the Hypatia colloquium, I discussed the evolution of dust-obscured star-formation of galaxies at $z \sim 3$ to $z \sim 6$ revealed by ALMA, including a recent ALMA large program: ALPINE. Furthermore, I also discussed newly found heavily dust-obscured galaxies in the epoch of reionization (EoR) from the on-going ALMA large program: REBELS. The newly found dusty galaxies are serendipitously found as companions of UV bright main-sequence galaxies at $z \sim 7$. Given the limited survey volume, they suggest an additional $10 - 25\,\%$ contribution to the cosmic star-formation rate density. These studies of dust attenuation properties and dust-obscured star-formation are crucial to interpret existing and upcoming observations, including upcoming very high-redshift galaxy observations by James Webb Space Telescope.

Dust Attenuation Properties of Star-Forming Galaxies at $z > 4$

To understand galaxy formation and evolution, star-formation rates (SFRs) of galaxies are one of the most fundamental parameters. For high-redshift galaxies, measuring SFRs of galaxies are largely based on the galaxy's rest frame ultraviolet (UV) emission which is generated by short-lived massive stars (i.e., O- or B-stars). As the UV emission is easily attenuated by interstellar dust, the dust attenuation correction is crucial to provide accurate total SFRs of galaxies.

To correct dust attenuation, there are mainly two methods: (1) direct observations of dust by infrared wavelengths, and (2) estimating dust attenuated UV emission by empirically calibrated relation. Because of its accessibility, one of the empirically calibrated relations is frequently used for high-redshift galaxies, which is known as the IRX-β relation [7]. The IRX-β relation is a powerful tool as one can perform dust attenuation correction only by a few photometry in the rest-frame UV emission. However, the relation is only calibrated using high-redshift analogue galaxies in the local Universe, and it is still unknown if the locally calibrated relation is really applicable to high-redshift galaxies.
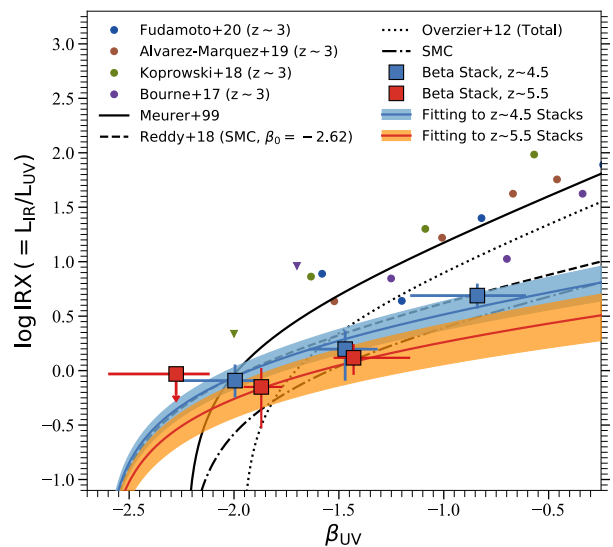
Figure 1: IRX-β relation obtained in the ALPINE survey [6]. The newly obtained relation suggests an evolution of dust attenuation properties of star-forming galaxies at $z > 4$, suggesting SMC-like dust attenuation properties and bluer intrinsic UV spectral slope.

The recent ALMA large program: ALPINE is an ideal opportunity to study dust attenuation properties of high-redshift galaxies. In the ALPINE survey, we targeted 118 main-sequence star-forming galaxies at $z = 4.5 - 6$, and observed [CII] $158\,\mu\mathrm{m}$ emission line and dust continuum. As a result, we obtained 23 individual dust continuum detections. Using the dust continuum observations, we created IRX-β of the target galaxies, which provided us the dust attenuation relation directly using high-redshift galaxies.

The resulting IRX-β relation (Figure 1) shows that locally calibrated relation is not applicable to $z > 4$ galaxies, and prefers bluer intrinsic UV slope (β) and flatter slope of the IRX-β relation. This suggests that dust attenuation properties of high-redshift galaxies are represented by a steep attenuation curve in UV emission, similar to or even steeper than dust extinction curve observed in the SMC.

At the same time, the observed low IR luminosity suggests the low obscured fraction of star-formation activities ($f_{\rm obs} = {\rm SFR}_{\rm IR}/{\rm SFR}_{\rm tot}$). For massive galaxies with $log M_*/M_\odot > 10$, the observed $f_{\rm obs}$ at $z \sim 5.5$ is around 50%, while the $f_{\rm obs}$ at $z < 3$ is $\sim 90\,\%$ [8]. This suggests rapid build-up of dust-obscured star-formation activity between $z \sim 5.5$ to $z \sim 3$ Universe. Further ALMA surveys to observe high-redshift galaxies are required to confirm and extend the newly found evolution from the ALPINE survey.

Dust-obscured Star-Formation Activities in the Epoch of Reionization

In the EoR, heavily dust-obscured galaxies are known to be limited to the extreme starburst galaxies [9] and companions of rare quasars [10]. These studies conclude that the contribution of dust-obscured galaxies to the cosmic star formation rate density at $z > 6$ is sub-dominant. Recent ALMA and Spitzer observations have identified a more abundant, less extreme population of obscured "optically-dark" galaxies at $z = 3 - 6$ [11]. However, this population has not been confirmed in the EoR so far.

In the latest ALMA large program, REBELS, we observed 40 main-sequence star-forming galaxies at $z = 6.5 - 9$ to scan [CII] $158\,\mu$m or [OIII] $88\,\mu$m emission lines. From two of the REBELS targets, REBELS-29 and REBELS-12, we identified serendipitous emission lines and dust continuum as companions of $z \sim 7$ galaxies (Figure 2). Although estimated SFRs and stellar masses are consistent with the main-sequence of $z \sim 7$ galaxies, these serendipitously found galaxies are completely absent from rest-frame UV images. This suggests that the newly found galaxies are heavily dust-obscured, but otherwise "normal" galaxies in the EoR. The finding of less extreme dusty star-forming galaxies in the clustered environments shows that we are still missing a significant amount of star-formation activities in the EoR. Although uncertain, after correcting clustering, current estimates suggest an additional $10 - 25\,\%$ contribution to the cosmic star-formation rate density.

The complete census of star-formation activities is clearly a prerequisite to understand the cosmic reionization. Further deep and wide field surveys by ALMA and JWST are essential to confirm number density of the heavily dust-obscured galaxy population, and to study how galaxies formed and evolved in the EoR.

Conclusion

Compared to the rest-frame UV observations, the infrared observation of high-redshift galaxies is still highly incomplete despite 10 years of ALMA operations with large amounts of scientific discoveries. However, we started to find several important properties of high-redshift galaxies, and our ALMA observations are becoming more and more efficient given the past experience and findings. In the next 10 years, we will be able to see more rapid progress of our understanding of high-redshift galaxies with strong synergy of ALMA and JWST.
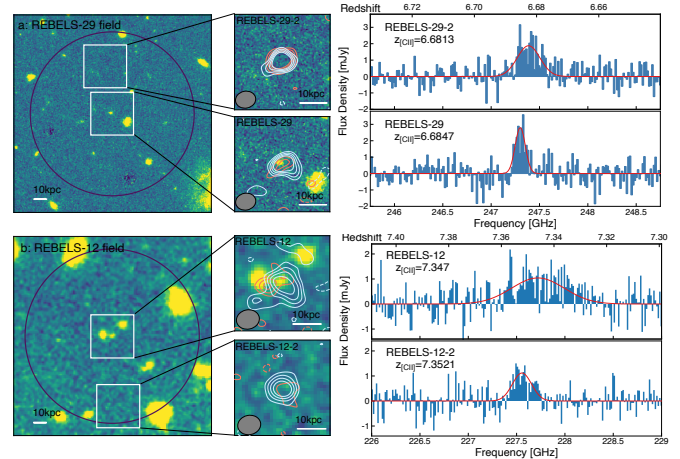

Figure 2: Two heavily dust-obscured, but otherwise "normal" galaxies are identified as companions of main-sequence galaxies at $z \sim 7$ [12]. The detections from tiny survey volume suggest the wide-spread existence of such dusty galaxies in the epoch of reionization.

At the same time, several on-going projects to build extremely sensitive and large single dish millimeter/submillimeter telescopes (such as Large Submillimeter Telescope; LST[¶]) will provide complementary observation with their large field of view in the future. The JWST and future telescope plans will make our high-redshift galaxy view more complete, and our current study will pave the way to our future understanding of galaxy formation and evolution throughout cosmic history.

References

[1] Bouwens, R. J., et al. 2015, ApJ, 811, 140
[2] Oesch, P. A., et al. 2018, ApJ, 855, 105
[3] Atek, H., et al. 2018 MNRAS, 479, 5184
[4] Capak, P. L., et al. 2015, Nature, 522, 455
[5] Bouwens, R., et al. 2020, ApJ, 902, 112
[6] Fudamoto, Y., et al. 2020, A&A, 643, A4
[7] Meurer, G. R., et al. 1999, ApJ, 521, 64
[8] Whitaker, K. E., et al. 2017, ApJ, 850, 208
[9] Marrone, D. P., et al. 2018, Nature, 553, 51
[10] Decarli, R., et al. 2017, Nature, 545, 457
[11] Wang, T., et al. 2019, Nature, 572, 211
[12] Fudamoto, Y., et al. 2021, Nature, 597, 489

Short CV

2016:   Master in Astronomy, Ludwig-Maximilians-Universität München, Germany
2020:   PhD in Astronomy, University of Geneva, Switzerland
2021–present: NAOJ-ALMA Project Postdoctoral Research Fellow, Tokyo, Japan

[¶]https://en.lstobservatory.org/

High-z Lyman break galaxies with JWST: parallel observations of dwarf satellites

Viola Gelli

Università degli Studi di Firenze, via G. Sansone 1, I-50019, Sesto Fiorentino, Italy

The upcoming advent of the James Webb Space Telescope (JWST) will revolutionise our understanding of the distant Universe, allowing us to unveil the properties of the faintest galaxies during the Epoch of Reionization ($z > 6$). Among the numerous new sources that will be discovered, we are particularly interested in dwarf galaxies ($M_\star < 10^9 \mathrm{M_\odot}$). These objects are indeed fundamental in cosmic history since they are the first galaxies to form in the Universe and they represent the basic building blocks responsible for the build-up, through merger events, of the massive galaxies we see today. Dwarf galaxies have been observed and studied in great details in the Local Universe, where dozens of them live as *satellites* of more massive galaxies like our Milky Way [1]. At high-z we do expect an analogous situation, i.e. the presence of not only *isolated* dwarf galaxies in the field [2], but also of *satellite* dwarf galaxies dwelling around massive systems like Lyman Break Galaxies (LBG). I investigated for the first time high-z dwarf satellite galaxies in order to answer some fundamental questions: what are the expected physical properties of this distinct population of dwarf galaxies living in dense environments around massive LBGs? Will JWST be able to detect them for the first time?

To address these questions I used a state-of-art cosmological simulation, described in [3]. It is an high-resolution ($\Delta x \approx 10\,\mathrm{pc}$) simulation that follows the evolution of a massive LBG ($M_\star \simeq 10^{10}\mathrm{M_\odot}$) up to $z \sim 6$, reproducing the typical observed properties. I inspected the surrounding regions of the LBG, finding that five dwarf galaxies and one proto-globular cluster live within its virial halo. In the following, I first describe their main evolutionary and stellar properties (as detailed in [4]), and then I take a step further studying their expected stellar emission and predicting their detectability with JWST [5].

Dwarf satellites of high-z LBGs

My analysis [4] demonstrated that the evolutionary and chemical properties of high-z dwarf galaxy satellites are independent of their orbits, while they are regulated by their mass. This is illustrated in Figure 1, where the age-metallicity relation, star formation rate and metallicity distribution function are shown, for satellites pertaining to different categories. Low-mass dwarf satellites ($M_\star < 5 \times 10^8\mathrm{M_\odot}$, upper panel) experience short and intense bursts of star formation ($< 50\,\mathrm{Myr}$) and are then completely quenched by internal *SN feedback*. On the other hand, high-mass satellites ($M_\star > 5 \times 10^8\mathrm{M_\odot}$, lower panel) have much longer star formation histories, fueled by the numerous *merger events* characterising the dense environment surrounding the massive LBG. We note that both types of satellites are highly enriched in metals with respect to typical isolated dwarf galaxies, reflecting an interstellar medium that by $z \sim 6$ has already been significantly polluted with heavy elements by the central LBG. In this scenario, high-mass dwarf satellites typically form at earlier times ($z > 9$) in a still pristine environment. However, despite their initial higher metallicities, low-mass systems contain a larger amount ($> 50\%$) of metal-poor stars ($\log Z_\star/\mathrm{Z_\odot} < -0.5$), due to their shorter star formation histories.
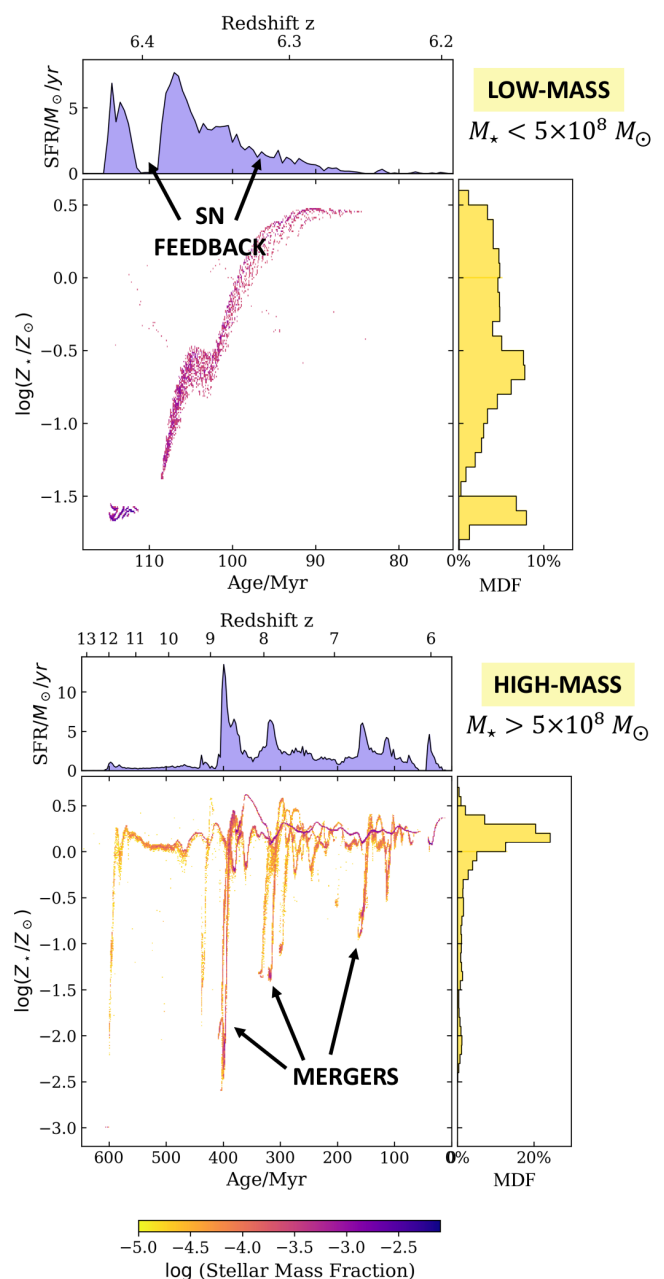

Figure 1: Examples of stellar age - metallicity relation (centre), star formation rate (top) and metallicity distribution function (right) for the two types of satellite dwarf galaxies.
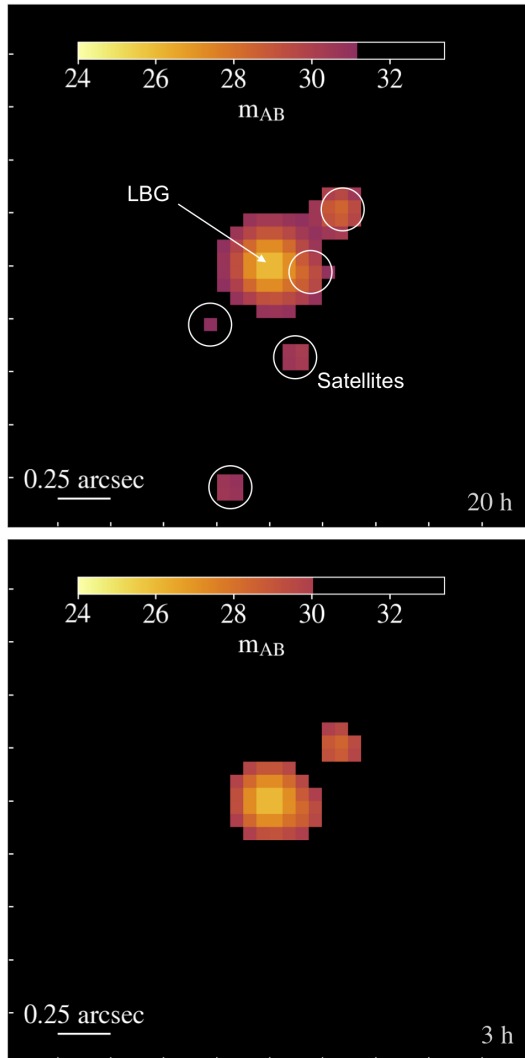
Figure 2: Synthetic images of the central LBG and its dwarf satellites in the filter F356W, for 20h (top) and 3h (bottom).

reconstructed their expected spectra [5].

I used STARBURST99 [6] to model their stellar emission at all stages of their evolution up to $z \sim 6$, and I also took into account the attenuation of dust [7]. I then produced synthetic images of the system of LBG and its dwarf satellites in order to understand if these can be spatially resolved by JWST and their emission disentangled from that of the highly luminous central galaxy. In Figure 2, I show as an example the results at $z \sim 6$ in the filter F356W of the NIRCam instrument. The coloured pixels show the flux above the S/N~ 3 sensitivity threshold for different exposure times. Noticeably the emission of all five dwarf galaxies is detectable in 20 hours, despite most satellites being at the faintest level of their evolution at the displayed stage, having been quenched by SNe feedback (Figure 1). Moreover, the flux of the two most massive satellites can be detected in just 3 hours. The images reveal that we can disentangle the emission of the satellites from the one of the central LBG if they are located at a distance of at least $> 0.25''$ from its centre, requirement achieved by all our galaxies except for one. Having demonstrated that JWST/NIRCam will indeed be able to catch the stellar emission of satellites of LBGs, I also derived color-magnitude diagrams of all the systems during their evolution. I found that the color F200W-F356W will represent a powerful diagnostic tool that can be used to identify star-bursting, low-mass, metal poor systems.

Already during the first planned campaigns, as for instance with the deep JADES survey, NIRCam will provide observations of dozens of LBGs. As a consequence, we expect to obtain *for free* and *for the first time* the detection of hundreds of satellite dwarf galaxies: a free lunch for JWST.

References
[1] McConnachie, A. W. 2012, AJ, 144, 4
[2] Zackrisson, E., et al. 2017, ApJ, 836, 78
[3] Pallottini, A., et al. 2017, MNRAS, 471, 4128
[4] Gelli, V., et al. 2020, MNRAS, 498, 4134
[5] Gelli, V., et al. 2021, ApJL, 913, 25
[6] Leitherer, C., et al. 1999, ApJS, 123, 3
[7] Weingartner, J. C. & Draine, B. T. 2001, ApJ, 548, 296

Can we detect high-z satellites?

In order to understand if the detection of high-z satellites will be feasible through imaging and photometry already during the first deep surveys with JWST (e.g., JADES), I

Short CV

2016–2019:	Master's Degree in Physics and Astrophysics, Università degli Studi di Firenze, Florence, Italy
2019–present:	PhD Student, Università degli Studi di Firenze, Florence, Italy

Cosmic telescopes: witnessing the radio quiet quasar emission mechanism

Philippa Hartley

SKA Organization, Jodrell Bank, Lower Whitington, Macclesfield SK11 9FT, UK

A small fraction – around 10 percent – of quasars produce large amounts of radio emission resulting from the acceleration of plasma particles in galactic-scale jets, which are thought to result from the violent accretion and collimation of matter close to the central supermassive black hole. In the remaining 90 percent of the population, however, large jets are absent, and little radio emission is observed. This stark difference leads some authors to suggest that so-called radio quiet quasars (RQQ) constitute a different population of objects from their radio loud counterparts: a population where star-formation is ongoing in the host galaxy [1, 2, 3]. On the other hand, some authors use evidence of excess radio emission from the radio–far-infrared (radio–FIR) correlation obeyed by star-forming galaxies [4], or of a continuous distribution between radio quiet and radio loud sources [5] to point to the existence of AGN-related radio emission in RQQ, perhaps occurring at different power scales [6]. The problem is crucial for the understanding of galaxy evolution; only by determining what is happening in these puzzling objects can we fully describe the role played by AGN feedback processes in the quenching of star-formation, responsible ultimately for the large numbers of 'red and dead' elliptical galaxies observed at late times in the local Universe.

Figure 2: Reconstruction of the unlensed RQQ of HS 0810+2554. The model comprises radio components 1 (blue marker) and 2 (red marker) located either side of an optical component (black marker). All three components are located on the inner side of the tangential lensing caustic (black curve), along which lensing magnification theoretically reaches infinity. The morphology and brightness temperatures of the radio components provide strong evidence that this RQQ features two mini radio jets either side of the optical quasar core (see [10]).
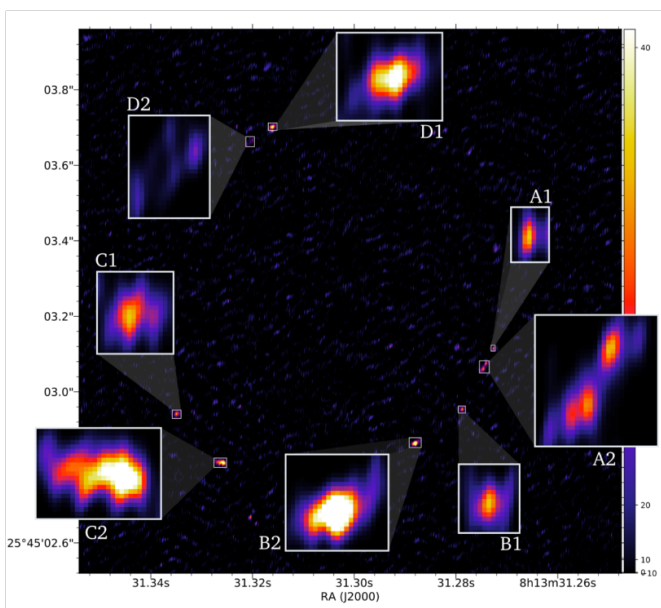

Figure 1: Radio emission from strongly lensed RQQ HS 0810+2554 using the EVN at 1.4 GHz. The very high resolution of the EVN combined with the magnification of lensing reveals that the background source consists of two highly compact components, each of which has been lensed into four images (see [10]).
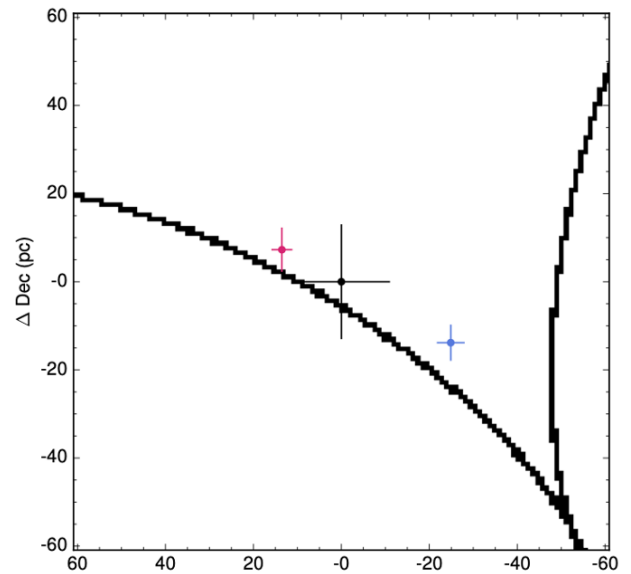
Strong gravitational lensing

Strong gravitational lensing, predicted by Einstein[||], is produced when the light from a background object is strongly deflected by a large intervening mass, such as a galaxy or cluster of galaxies. The resulting pattern we observe – featuring multiple images and sometimes dramatic arcs – is dependent on the distribution of the lensing mass. Strong lensing is therefore a powerful tool for the study of mass structures – both baryonic and dark – allowing us to probe the dark matter power spectrum down to the 10 $M_\odot$ scale [7]. The magnification afforded by lensing also increases the effective resolution and sensitivity of our observing instruments, such that a magnification factor of 10 provides ten-fold the instrumental resolution and a one hundred-fold effective integration time. Strong lenses therefore serve as 'cosmic telescopes', giving us access to the very faintest galaxy populations and resolving their structure into unprecedented detail. We use strong lenses to directly address the RQQ radio emission problem.

[||] *"Of course, we have no hope of observing this phenomenon directly"*, Einstein (1936)
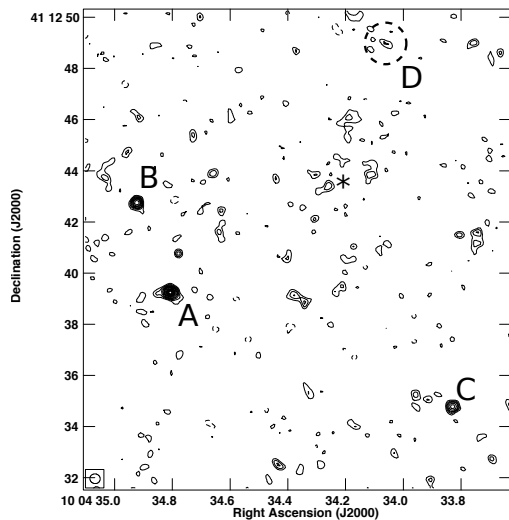
Figure 3: VLA 5 GHz map of strongly lensed RQQ SDSS J1004+4112. The RQQ radio emission is lensed into four images by an intervening galaxy cluster. Image D, which traverses the greatest distance of the four images, and is therefore the last to arrive, has more than halved in brightness in six years. Such rapid variability is strong evidence for the highly compact radio emission associated with the central AGN engine (see [8]).

The cosmic telescopes programme

Setting out to study all quadruply-lensed RQQ located above -30° declination, the cosmic telescopes programme [9] has used high sensitivity radio observations combined with the magnification power of lensing to directly probe the RQQ radio emission mechanism. We find, in this very faint population, that AGN-related activity can be responsible for the bulk of radio emission even in sources that reside in the faint end upturn of the radio quasar luminosity function typically modelled using a star-forming population. For example, very long baseline interferometry (VLBI) observations using the European VLBI Network (EVN) have demonstrated the presence of two mini-jets aligned in a linear configuration either side of the optical core in HS 0810+2554, a RQQ at redshift $z = 1.51$ (Figure 1 and 2). In this case, a lensing magnification factor of at least 50 provided an effective resolution of just 0.1 milli- arcseconds, or 0.27 parsec at the redshift of the source which, with a peak flux density of 890 nJy, is the faintest source ever imaged [10]. Jansky Very Large Array (VLA) observations of two $z = 1.7$ RQQ, SDSS J1004+4112 and PG 1115+080, has also found evidence of AGN-related radio emission, in the variability of the source (see Figure 3) and in the excess radio emission with respect to FIR emission associated with star-formation (see Figure 4), respectively [8]. Both HS 0810+2554 and SDSS J1004+4112 have been found to contain ultrafast outflows [11, 12], and both are found to lie on the radio-FIR correlation. Evidence

of AGN-related radio emission in these sources therefore hints at a connection between small and large scale AGN feedback process, and calls into question the use of the radio–FIR correlation to distinguish between AGN and star-forming activity in RQQ.

The RQQ picture is mixed, however, with some RQQ showing strong evidence for ongoing star-forming activity. For example, [13] have used the Atacama Large (sub)Millimeter Array (ALMA) and VLA observations to demonstrate a radio emission region that is co-spatial with a rotating molecular disk. Further, in a source that was not detected using VLBI observations [14], [15] used ALMA observations to find evidence for turbulent star-forming activity in the quasar host . The result leads the authors to suggest that RQQ star-formation efficiency is dependent on the host galaxy morphology as opposed to the nature of the AGN. Our programme continues with new and upcoming observations to help us determine once and for all the feedback mechanisms at play in RQQ and their role in galaxy evolution.
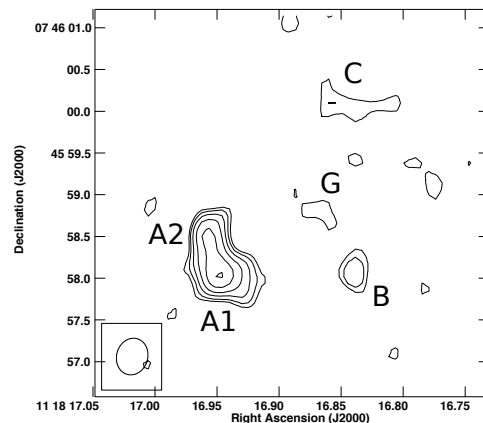
Figure 4: VLA 5 GHz map of strongly lensed RQQ PG 1115+080. Comparing the imaged radio emission with the FIR luminosity associated with star-formation finds an excess of radio emission with respect to the radio–FIR correlation obeyed by star-forming galaxies. Star-formation alone does not appear to explain the radio emission in this RQQ (see [8]).

References

[1] Kellerman, K.I., et al. 1989, AJ, 98, 1207
[2] Condon, J.J., et al. 2013, ApJ, 768, 37
[3] Stacey, H.R., et al. 2018, MNRAS 476, 5075
[4] White, S.V., et al. 2017, MNRAS, 468, 238
[5] Zakamska, N.L., et al. 2016, MNRAS, 455, 4191
[6] Jarvis, M. E., et al. 2019, MNRAS, 485, 2710
[7] Metcalf, R. B., & Madau, P. 2001, ApJ, 563, 9
[8] Hartley, P., et al. 2021, MNRAS, subm.
[9] Jackson, N., et al. 2015, MNRAS, 454, 287
[10] Hartley, P., et al. 2019, MNRAS, 485, 3009
[11] Chartas, G., et al. 2016, ApJ, 824
[12] Chartas, G., et al. 2003, ApJ, 595, 85
[13] Badole, S., et al. 2020, MNRAS, 496, 138
[14] Wucknitz, O., & Volino, F. 2008, arXiv:0811.3421
[15] Paraficz, D., et al. 2018, A&A, 613, A34

Short CV

2010: MSc in Astronomy and Astrophysics (part-time), University of Manchester, UK
2013: PhD in Astronomy and Astrophysics (part-time), University of Manchester, UK
2019: SKAO Postdoctoral Fellow, Cheshire, UK

Stellar population gradients of SAMI central galaxies

Giulia Santucci

University of New South Wales, NSW 2052, Australia

Massive galaxies at $z \sim 2$ are already found to be quiescent, but compact, with an effective radius (R_e) half of the size of galaxies of similar mass in the local universe [e.g., 1, 2, 3]. Hydrodynamical-zoom cosmological simulations found that massive galaxies likely form in a two-phase formation scenario [e.g., 4]. During the first phase, at high redshift, they grow by a rapid episode of in-situ star formation, resulting in compact massive systems. The initial stellar metallicity gradient is set by the initial episode of star formation, with the metallicity decreasing outward in the galaxy [5, 6]. From this process, we would expect steep, negative metallicity gradients and flat age radial profiles. After $z \approx 2$, these massive compact galaxies ($\log_{10}(M_*/M_\odot) > 10.5$) are predicted to be quiescent and grow mostly by accreting mass through galaxy interactions that add stars to their outskirts [4, 7, 8].

Integral field spectroscopy enables the mapping of stellar populations and kinematics across individual galaxies, rather than obtaining parameters from only the centre or one axis of the galaxy as fibre or long-slit observations do. My first PhD research project focused on studying the stellar population profiles of massive passive galaxies in order to understand how massive galaxies evolve. In particular, the main goal of this work was to determine whether central galaxies have different stellar population properties when compared to similarly massive satellite galaxies. The stellar populations of galaxies provide a means by which to determine their evolutionary histories. The efficiency of star formation, gas fractions and mergers leave imprints in the radial distributions of these populations. We studied the stellar population (age, metallicity, and [α/Fe]) radial profiles of passive galaxies in the SAMI Galaxy Survey.

Galaxy sample

The Sydney-AAO Multi-object Integral field spectrograph (SAMI) Galaxy Survey is a large, optical Integral Field Spectroscopy [9] survey of low-redshift ($0.04 < z < 0.095$) galaxies covering a broad range in stellar mass, $7 < \log_{10}(M_*/M_\odot) < 12$, morphology and environment. The sample, with ≈ 3000 galaxies, is selected from the Galaxy and Mass Assembly Survey (GAMA survey; [10]) regions (group galaxies), as well as eight additional clusters to probe higher-density environments [11].

Our sample consists of 533 passive galaxies with reliable measurements for metallicity and age in at least 3 annular apertures (96 central galaxies and 437 satellite galaxies) and 332 galaxies with reliable measurements for [α/Fe] in at least three annular apertures (79 centrals and 253 satellites). We focus on the passive central galaxies to ensure a like-to-like comparison in determining how their central and satellite status affects their stellar population gradients.
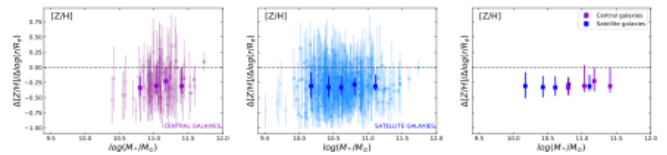

Figure 1: Metallicity gradients as a function of stellar mass. Individual gradients are shown in purple for central galaxies (left panel) and blue for satellites (middle panel) and the median value in bins of stellar mass in bold. The right panel shows the median gradient values for each mass bin in the two environments. Metallicity gradients are negative and shallow, for both central and satellite galaxies.
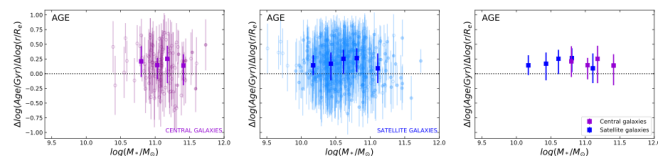
Figure 2: Age gradients as a function of stellar mass. All point types are as per Figure 1. Age gradients are generally positive and shallow for both central and satellite galaxies.
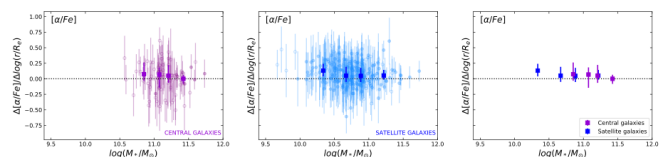
Figure 3: [α/Fe] gradients as a function of stellar mass. All point types are as per Figure 1. [α/Fe] gradients are consistent with zero for both central and satellite galaxies. We find a weak trend of the gradients with stellar mass.

Results

For the whole sample, we find negative metallicity radial gradients, which show evidence of becoming shallower with increasing stellar mass (Figure 1). The age and [α/Fe] gradients are slightly positive and consistent with zero, respectively (Figure 2 and Figure 3). The [α/Fe] gradients become more negative with increasing mass, while the age gradients do not show any significant trend with mass. We do not observe a significant difference between the stellar population gradients of central and satellite galaxies at fixed stellar mass. The mean age and [α/Fe] gradients are consistent between central and satellite galaxies, within the uncertainties. The stellar population gradients of central and satellite galaxies show no difference as a function of halo mass.

The gradients we find are consistent with those predicted for galaxies formed in a two-phase process [7, 12].

In this scenario, galaxies first undergo a rapid formation phase during which 'in-situ' stars are formed within the galaxy. The more massive ETGs start forming stars at earlier epochs. The resulting galaxy is compact, with a steep negative metallicity gradient (with gradients ranging from $\Delta[Z/H]/\Delta \log(r/R_e) = -0.35$ to -1.0; [12]) and a positive age gradient (due to the presence of a younger stellar population in the center of the galaxy). More specifically, the metallicity and age gradients would naturally correlate with galaxy mass as star formation lasts longer in the center of more massive systems which have deeper central potential wells [e.g. 12], so that more massive galaxies would have younger and more metal-rich centers, more positive age gradients and more negative metallicity gradients.

After the star formation is quenched, a second phase of slower evolution is dominated by dissipationless mergers. In particular, galaxy interactions will either steepen or flatten the metallicity gradients: major dissipationless mergers tend to cause gradients to become shallower, as metal-rich stars from the centre of the galaxy are redistributed further out (e.g., [12, 13]) and minor dissipationless mergers lead to steeper negative metallicity gradients, due to metal-poor stars being accreted in the outer regions from lower mass galaxies (e.g., [14]).

Central galaxies, due to their privileged position in the center of the potential well, are expected to experience a greater number of galaxy interactions compared to satellite galaxies. In this scenario, simulations predict flat or slightly positive age gradients, due to old stars being added in the outer regions (at radii $> 2R_e$; [14]), and [α/Fe] profiles are expected to be flat as a result of massive early-type galaxies assembling via mergers with low-mass systems [15]. These predictions are in agreement with our findings: the metallicity gradients we find are shallower than those predicted by a monolithic collapse (ranging from $\Delta[Z/H]/\Delta \log(r/R_e) = -0.5$ [16] to $\Delta[Z/H]/\Delta \log(r/R_e) = -1.0$ [12]), hinting to a flattening of the gradients due to mergers. The age gradients are slightly positive (with central stars having younger ages than stars in the outskirts) and generally flat [α/Fe] gradients. However, since evidence of minor later accretions are expected at radii > 1.5-$2R_e$ and the majority of the radial profiles for our central galaxies only extend to a maximum of $2R_e$, our results point to a similar evolution path for the inner regions of both central and satellite galaxies.

The fact that our metallicity gradients for central and satellite galaxies are consistent within the standard deviation suggests that the inner regions of central galaxies (up to $2 R_e$) form in a similar fashion to similarly massive satellite galaxies. Moreover, the gradients for galaxies in high-mass halos show no trend with stellar mass. This seems to point to a similar evolution for galaxies in denser environments, regardless of their current position in the halo [17].

References

[1] Daddi, E., et al. 2005, ApJ, 626, 680
[2] Trujillo, I., et al. 2006, MNRAS, 373, 36
[3] van Dokkum, P.G., et al. 2008, ApJL, 677, 5
[4] Naab, T. et al., 2009, ApJL, 699, 178
[5] Larson, R.B., et al. 1974, MNRAS, 166, 585
[6] Thomas, T., et al. 2005, ApJ, 621, 673
[7] Oser, L., et al. 2010, ApJ, 725, 23120
[8] Hopkins, P.S., et al. 2009, ApJS, 181, 135
[9] Bryant, J.J., et al. 2015, MNRAS, 447, 2857
[10] Driver, S.P., et al. 2011, MNRAS, 413, 971
[11] Owers, M.S., et al. 2017, MNRAS, 468, 18240
[12] Kobayashi, C., et al. 2004, MNRAS, 347, 740
[13] Taylor, P., et al. 2017, MNRAS, 471, 3856
[14] Hirschmann, M., et al. 2015, MNRAS, 449, 528
[15] Gu, M., et al. 2018, ApJ, 862, 18
[16] Carlberg, R.G., et al. 1985, ApJ, 298, 486
[17] Santucci, G., et al. 2020, ApJ, 896, 75

Short CV

2016: Master in Astrophysics, University of Bologna, Italy
2022: PhD in Astrophysics, University of New South Wales, Australia

GALAXIES AND GALACTIC NUCLEI

Left image: The peculiar galaxy Centaurus A (NGC 5128). Credit: ESO
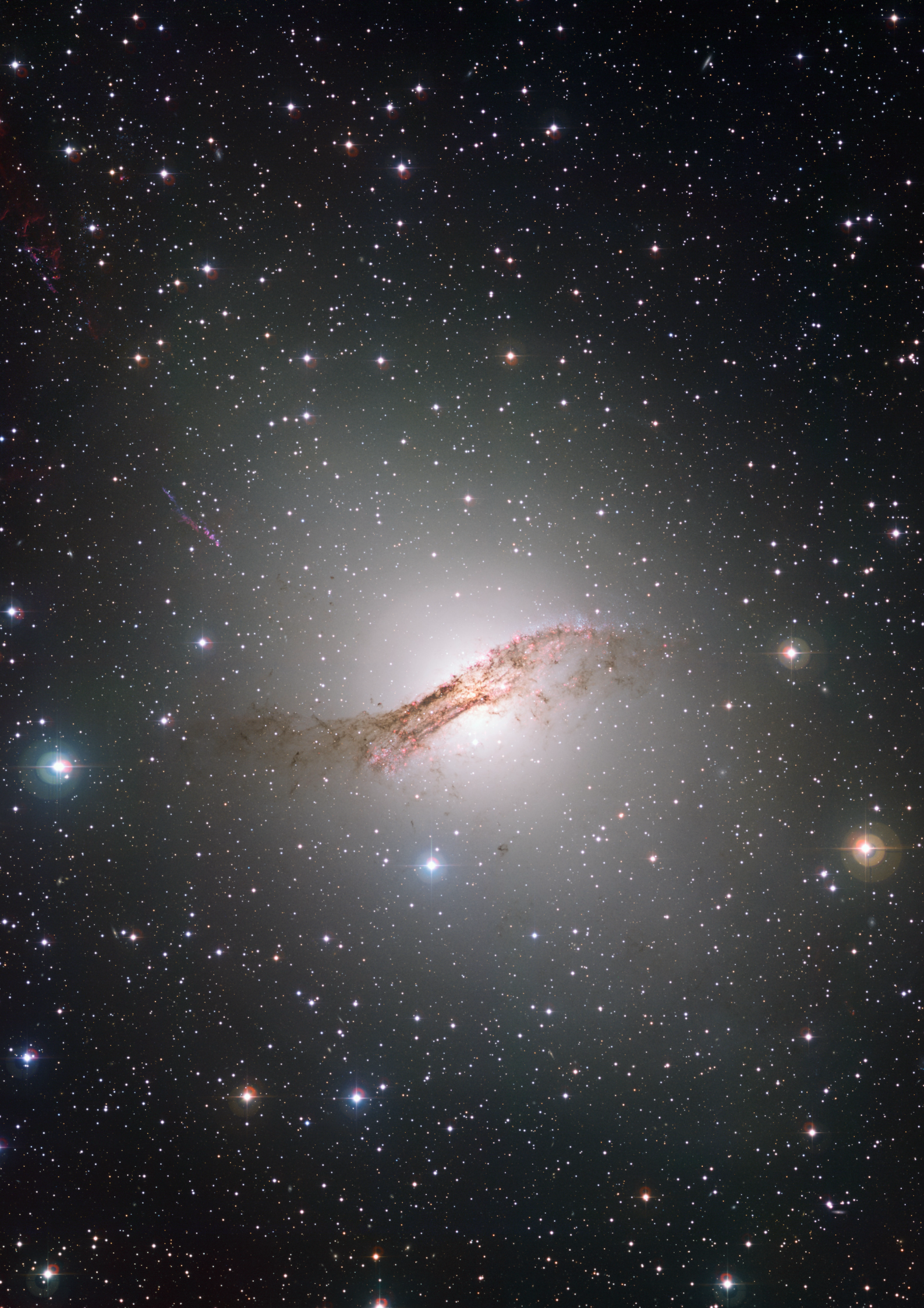
Exploring the metal-poor inner Milky Way with the *Pristine* survey

Anke Arentsen

Université de Strasbourg, CNRS, Observatoire astronomique de Strasbourg,

UMR 7550, F-67000 Strasbourg, France

Stars are excellent messengers from the distant past, since the composition of their atmospheres resembles that of the gas out of which they were born. Ancient stars which formed very early in the Universe were born with few metals, and today they can be recognised as very low-metallicity stars. These are typically searched for and found in the most metal-poor component of the Milky Way, the Galactic halo, and in the satellite dwarf galaxies. However, we also expect them to be present in the very inner regions of our Galaxy, and those are in fact likely among the oldest stars in the Milky Way. The inner Galaxy has largely been avoided in the search for metal-poor stars due to challenges with dust extinction, crowding, and the presence of an overwhelming majority of more metal-rich stars. Very efficient pre-selection methods are necessary to uncover a large number of metal-poor stars in the bulge region, allowing us to study the properties of the metal-poor inner Galaxy.

The Pristine Inner Galaxy Survey (PIGS)

One efficient method of identifying metal-poor stars is using metallicity-sensitive narrow-band photometry, for example the CFHT/MegaCam *CaHK* photometry employed by the *Pristine* survey [1]. The *Pristine* survey has been immensely successful at uncovering metal-poor stars in the halo and dwarf galaxies, and encouraged by this success we started the *Pristine* Inner Galaxy Survey (PIGS) towards the Galactic bulge. The goals of PIGS are to find many of the oldest, metal-poor stars hiding in the inner Galaxy, and to study the properties of the metal-poor tail of the bulge and inner halo.

We spectroscopically followed up metal-poor candidates selected with *CaHK* and broad-band photometry using AAOmega+2dF on the Anglo-Australian Telescope (AAT), and derived stellar parameters including metallicities for this low/intermediate-resolution AAT sample. Figure 1 presents the metallicity distribution of the spectroscopic PIGS sample [2], compared to more "typical" bulge surveys (APOGEE [3] and ARGOS [4]) and compared to the pioneer large survey of metal-poor inner Galaxy stars EMBLA [5]. It shows that the PIGS strategy has been extremely successful at targeting the metal-poor tail of the inner Galaxy, with the largest number ($N = 1900$) of very metal-poor (VMP, $[\mathrm{Fe/H}] < -2.0$) stars to date. The unique PIGS sample can be used to study many scientific questions, two of which will be touched upon in these proceedings: how do the metal-poor inner Galaxy stars move compared to their more metal-rich counter parts, and what do the chemically peculiar carbon-enhanced metal-poor stars tell us about differences between the inner Galaxy and rest of the halo?
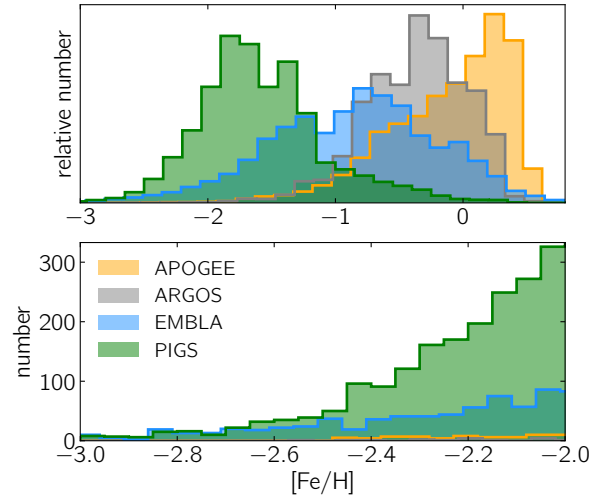

Figure 1: Top: relative metallicity distribution of PIGS compared to "typical" bulge surveys APOGEE [3] and ARGOS [4], and the dedicated metal-poor bulge survey EMBLA [5]. Bottom: absolute number of VMP stars in each of these surveys. Figure adapted from [2] and updated with additional data.

PIGS kinematics

The "normal", more metal-rich stars in the Galactic bulge have a boxy/peanut-shaped distribution and show signatures of solid-body rotation. This has been interpreted as the result of bulge formation through instabilities in the early Galactic disk, with little room for a classical, pressure-supported component [e.g., 6, 7]. There have been hints in recent years that for low-metallicity stars the rotation is slower or barely present at all [7, 8], pointing to a pressure-supported origin – a classical bulge and/or the extension of the halo. These studies were typically limited by small sample sizes.

With PIGS we have the perfect sample to study the behaviour of the (very) metal-poor tail of the inner Galaxy as function of metallicity. Figure 2 shows the rotation curve of the stars in PIGS, separated in four different metallicity bins [9]. For the first time, we clearly see a decrease in the strength of rotation with decreasing metallicity, until practically no rotational signature is left for the VMP stars. We also found that the velocity dispersion increases with decreasing metallicity [9]. These observations may point to a transition between the more metal-rich boxy bulge and the more metal-poor inner halo, but can also be related to other processes in the early inner Galaxy such as the exact process of how the boxy bulge formed and the number of metal-poor stars present in the early disk, and/or the dynamical influence of the bar on the halo.
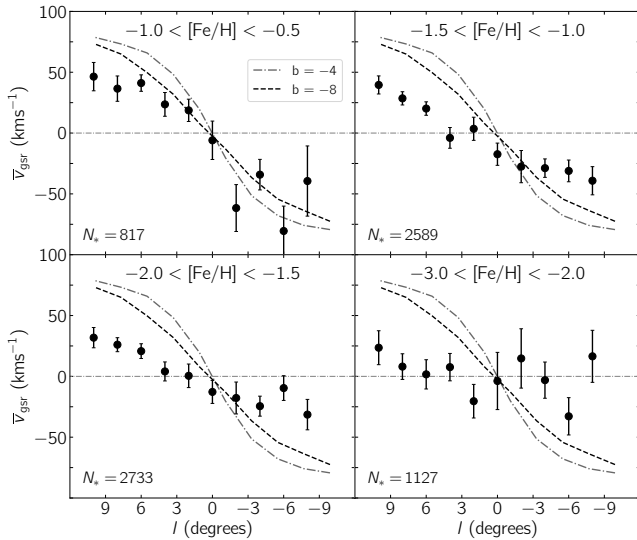
Figure 2: Rotation curve of PIGS stars as a function of metallicity, with the most metal-rich bin on the top left and the most metal-poor bin on the bottom right. Dashed and dotted lines are boxy bulge models from [6]. Based on a figure from [9] and updated with additional data.

metal-rich stars, and largely consistent for the extremely metal-poor ($[Fe/H] < -3.0$) stars. We investigated and discarded the possibility that this could be solely due to photometric selection effects, although they may play a role. Instead, the low CEMP fraction may point to a faster early chemical evolution in the (larger) building blocks that made the metal-poor inner Galaxy compared to the rest of the halo, resulting in fewer CEMP-no stars, and/or to a lower binary fraction in the inner Galaxy resulting in fewer CEMP-s stars.
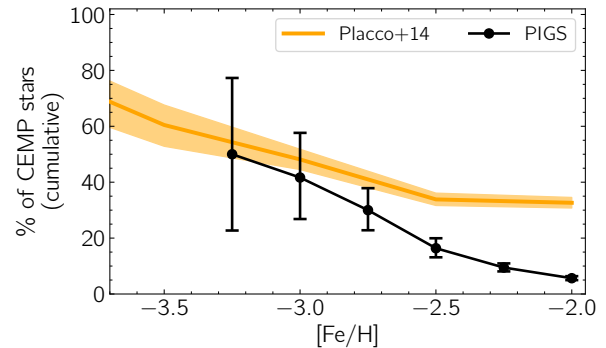
Figure 3: The fraction of CEMP stars in PIGS (black) compared to the literature halo CEMP fraction from [11] (orange). Based on a figure from [12].

PIGS CEMP stars

Besides comparing the dynamics of metal-rich and metal-poor inner Galaxy stars, we can use PIGS to compare the chemistry of VMP inner Galaxy stars to that of "typical" VMP halo stars. Of particular interest are the carbon-enhanced metal-poor (CEMP) stars – it has been recognised that many of the VMP stars in the halo have a large over-abundance in carbon, and that the relative fraction of CEMP stars increases with decreasing metallicity [e.g. 10, 11]. CEMP stars can form through interaction with a binary companion (mainly CEMP-s stars), or they could be *born* carbon-rich (mainly CEMP-no stars). The CEMP-no stars are extremely useful for learning about the early chemical enrichment in the Milky Way. Previously, only a handful of CEMP stars were known in the inner Galaxy, potentially with a much lower fraction compared to the halo.

The large sample size of PIGS, combined with the advantage that our analysis method can provide carbon abundance estimates from the AAT spectra, allows us to further investigate the inner Galaxy CEMP population. We identified 94 new CEMP stars in PIGS, increasing the known number towards the bulge by a factor of ten [12]. It is curious that the *fraction* of CEMP stars in PIGS is much lower than in the literature for the halo, as shown in Figure 3. The fraction is most discrepant for the more

Summary and outlook

With PIGS, we have successfully built a large sample of (very) metal-poor stars in the inner Galaxy. We studied the kinematics of the metal-poor inner Galaxy and investigated the occurrence of the chemically peculiar CEMP stars, leading to new insights into the ancient history of the central Milky Way. Further work will include a more extensive orbital analysis of the PIGS sample, high-resolution spectroscopic follow-up for detailed chemical abundances, and preparation for future large spectroscopic surveys such as 4MOST [13].

References
[1] Starkenburg, E., et al. 2017, MNRAS, 471, 2587
[2] Arentsen, A., et al. 2020, MNRAS, 496, 4964
[3] SDSS-IV Collaboration 2020, ApJS, 249, 3
[4] Ness, M., et al. 2013a, MNRAS, 430, 836
[5] Howes, L. M., et al. 2016, MNRAS, 460, 884
[6] Shen, J., et al. 2010, ApJ, 720, L72
[7] Ness, M., et al. 2013b, MNRAS, 432, 2092
[8] Kunder, A., et al. 2016, ApJ, 821, L25
[9] Arentsen, A., et al. 2020, MNRAS, 491L, 11
[10] Beers, T. C. & Christlieb N. 2005, ARA&A, 43, 531
[11] Placco, V. M., et al. 2014, ApJ, 797, 21
[12] Arentsen, A., et al. 2021, MNRAS, 505, 1239
[13] de Jong, R. S., et al. 2019, The Messenger, 175, 3

Short CV

2014–2016:   MSc in Astronomy, University of Groningen, The Netherlands
2016–2020:   PhD in Astrophysics, Leibniz-Institut für Astrophysik,
                      Potsdam, Germany
2020–present: Postdoc, Observatoire astronomique de Strasbourg, France

Nuclear stellar structures in barred galaxies of the TIMER survey

Adrian Bittner

European Southern Observatory, Karl-Schwarzschild-Strasse 2, 85748 Garching bei München

Bars are frequent structures in disc galaxies, especially in the local Universe where approximately 2/3 of them host bars. Although this bar fraction is decreasing with increasing redshift, there is still a substantial fraction of bars evident at $z \sim 1$ while in some massive galaxies bars have even been detected as early as redshift 2 [1, 2]. Given that bars are robust structures that are difficult to destroy [3], they interact with their host galaxies over timescales of many Gyr. This makes bars one of the major drivers of secular evolution in disc galaxies and, in fact, these stellar structures influence their host galaxies in a variety of ways. For instance, bars are promoting the inflow of gas from the main galaxy disc to its centre. This gas inflow is halted in the central regions of disc galaxies at radii a few hundred parsecs from the galaxy centre. There the gas settles and facilitates the formation of substructures, in particular nuclear discs, nuclear rings, and inner bars [4, 5].

Our goal is to better understand the formation, evolutionary history, and physical properties of these bar-built central structures in disc galaxies. To this end, we use observations with unprecedented spatial resolution, obtained with the MUSE (Multi-Unit Spectroscopic Explorer; [6]) integral-field spectrograph for a sample of 21 Milky Way-like galaxies in the local Universe. The observations were performed as part of the TIMER Survey [7] and cover the central $1\,\mathrm{arcmin}^2$ of the galaxies with a spatial sampling of $0.2\,\mathrm{arcsec}$, resulting in a data-set of approximately $90\,000$ spectra per galaxy.

Based on this unique data set, the TIMER collaboration has investigated various aspects of the central components of galaxies, including the variation of stellar population properties along and perpendicular to the major axis of main bars [8], the stellar feedback from star formation in nuclear rings [9], differences in the kinematics of young and old stellar populations [10], and the physical nature of inner bars [11, 12, 13].

In the following we summarise the results of two recent TIMER studies constraining the formation and physical properties of nuclear discs and nuclear rings by deriving their stellar kinematics and mean stellar population properties [14, 15]. To this end, we employ the modular software framework of GIST** (Galaxy IFU Spectroscopy Tool; [16]) to facilitate the efficient analysis of the data and a rich visualisation of the results.

The Nature of Nuclear Stellar Structures

The analysis of the stellar kinematics of the TIMER sample clearly shows that nuclear discs are characterised by high rotational support, i.e. they exhibit high rotation velocities, low velocity dispersion, and show signs of near-circular orbits, as indicated by a strong anti-correlation of velocity and the higher-order moment h_3 of the line-of-sight velocity distribution (see Figure 1). These results are consistent with the picture of bar-driven secular evolution in which a bar funnels gas to the galaxy centre where it settles and forms a new stellar component in a kinematically cold configuration. In addition, we find a clear correlation between the kinematic size of the nuclear discs (i.e. the radius at which v/σ peaks) and the length of the bar. As this correlation is stronger than the correlation between the size of the nuclear disc and main galaxy disc, it reinforces the strong physical connection between bars and nuclear discs.
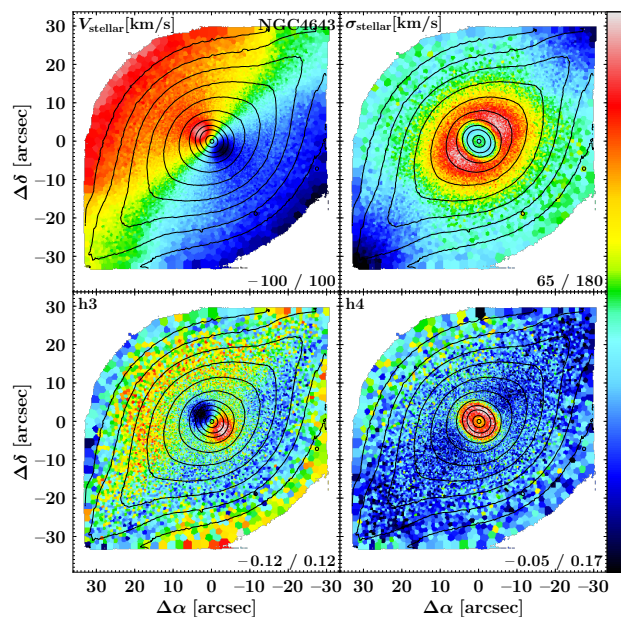
Figure 1: Spatially resolved maps of the stellar velocity, velocity dispersion, and higher-order moments h_3 and h_4 of the galaxy NGC 4643. The nuclear disc is clearly discernible as a rapidly rotating central component with low stellar velocity dispersion.

Spatially resolved maps of the stellar population properties reveal that nuclear discs are significantly younger and more metal-enriched, as compared to their immediate surroundings (see Figure 2). This is expected in the bar-driven formation scenario, as the main disc and bar would, thus, form before the nuclear disc. In addition, the low [α/Fe] abundances of the nuclear discs indicate a slow but prolonged star-formation activity, again as expected in the picture of a bar-driven formation. This finding clearly contrasts with the formation of old and kinematically hot classical bulges in violent accretion events and their typically elevated [α/Fe] abundances.
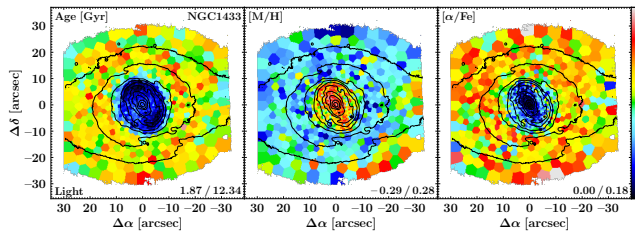

** https://ascl.net/1907.025

Figure 2: Spatially resolved maps of stellar ages, metallicities, and [α/Fe] abundances of the galaxy NGC 1433. The nuclear disc exhibits significantly lower stellar ages, high metallicities, and depleted [α/Fe] abundances, as compared to its immediate surroundings.

The Inside-out Formation of Nuclear Discs

While these young and kinematically cold nuclear discs are found in all galaxies of the TIMER sample, prominent nuclear rings are detected in only a few of them. The main difference between those galaxies hosting nuclear discs with and without nuclear rings is the availability of gas in the centre. Galaxies without nuclear rings exhibit barely any gas in their central regions. However, in galaxies with a significant amount of gas this gas is highly concentrated in a ring at the outer edges of the nuclear discs, i.e. in nuclear rings. In other words, nuclear rings can be understood as the gaseous outer edges of nuclear discs and seem to simply highlight the spatial region in which the bar-driven gas inflow is halted (see Figure 6 of [14] for a comparison of galaxies with and without nuclear rings).

Since the available gas in the galaxy centre is strongly concentrated in the nuclear rings, star formation also predominantly proceeds there. However, nuclear discs are found to be continuous stellar components that extend to the very centres of these galaxies. How is it possible that continuous stellar nuclear discs are formed if star-formation is in all cases limited to the gaseous nuclear rings at their outer edges? The explanation for this ques-

tions can be found in the co-evolution of nuclear rings and the bars that facilitate the gas inflow. More specifically, bars evolve considerably with time and tend to grow longer and stronger [17, 18]. In addition, we show that the radial extent of nuclear rings and bars is correlated, although it is still debated which precise physical process determines the radial size of nuclear rings.

In this picture, shortly after bar formation the bar is still comparably short resulting in the formation of a nuclear ring with small radius. As the bar evolves and grows longer and stronger, the nuclear rings should also grow in radius. As a result, a gaseous nuclear ring is located at each radius in the nuclear disc at any given point in time and, hence, a continuous stellar nuclear disc can be built from this series of star-forming nuclear rings with increasing radius. In fact, this inside-out formation scenario for nuclear discs is consistent with the negative gradients of stellar ages across nuclear discs (see e.g. Figure 4 in [14]) and was recently reproduced by numerical simulations [19].

References

[1] Sheth, K., et al. 2008, ApJ, 675, 1141
[2] Simmons, B. D., et al. 2014, MNRAS, 445, 3466
[3] Athanassoula, E., et al. 2005, MNRAS, 363, 496
[4] Combes, F. & Gerin, M. 1985, A&A, 150, 327
[5] Piner, B. G., et al. 1995, ApJ, 449, 508
[6] Bacon, R., et al. 2010, Proc. SPIE, 7735, 773508
[7] Gadotti, D. A., et al. 2019, MNRAS, 482, 506
[8] Neumann, J., et al. 2020, A&A, 637, A56
[9] Leaman, R., et al. 2019, MNRAS, 488, 3904
[10] Rosado-Belza, D., et al. 2020, A&A, 644, A116
[11] de Lorenzo-Cáceres, A., et al. 2019, MNRAS, 484, 5296
[12] Méndez-Abreu, J., et al. 2019, MNRAS, 482, L118
[13] Bittner, A., et al. 2021, A&A, 646, A42
[14] Bittner, A., et al. 2020, A&A, 643, A65
[15] Gadotti, D. A., et al. 2020, A&A, 643, A14
[16] Bittner, A., et al. 2019, A&A, 628, A117
[17] Athanassoula, E. 2003, MNRAS, 341, 1179
[18] Martinez-Valpuesta, I., et al. 2006, ApJ, 637, 214
[19] Seo, W.-Y., et al. 2019, ApJ, 872, 5

Short CV

2015: BSc in Physics, Ludwig-Maximilians University, Munich, Germany
2016: Scientific Visitor, European Southern Observatory, Santiago de Chile, Chile
2017: Scientific Visitor, Instituto de Astrofísica de Canarias, Tenerife, Spain
2018: MSc in Astrophysics, Ludwig-Maximilians University, Munich, Germany
2021: PhD in Astrophysics, European Southern Observatory, Munich, Germany

The star formation histories of massive quiescent galaxies

Adam Carnall

University of Edinburgh, Royal Observatory, Edinburgh EH9 3HJ, UK

The properties of the most massive galaxies provide fundamental constraints on both galaxy formation physics and cosmology. In the local Universe, it is well established that the most massive galaxies have long since shut down (quenched) their star-formation activity, exhibiting stellar population ages of order 10 billion years (Gyr). However, the extremely slow time-evolution of such ancient stellar populations prevents us from determining precise formation red-shifts (e.g., [1, 2, 3]).

Spectroscopic studies at redshift, $z = 1 - 2$ ($8 - 9$ Gyr ago) have long demonstrated that massive quiescent galaxies with ages of several Gyr already exist at this epoch, suggesting such objects trace their origins back to the first billion years of cosmic history [4, 5]. Recently, strong constraints on the properties of such objects have been achieved via full-spectral-fitting analyses that use high-SNR spectroscopy to break the age-metallicity-dust degeneracy that plagues photometric studies.

In [6, 7], we introduce a new method for fitting spectroscopic data, combining a flexible empirical model for the systematic uncertainties that arise during the observing process with a sophisticated physical model for the galaxies being observed. The method is implemented using the Bagpipes code [8]. An example galaxy fitted with this method is shown in Figure 1. The recovered star-formation history (SFH) is shown in the inset panel, demonstrating this galaxy formed at $z \sim 1.5$.

Studies such as this confirm the oldest quiescent galaxies at $z \sim 1 - 2$ had quenched by $z \sim 6$. However, even at $z \sim 2$, such objects are already too old to draw detailed conclusions about their evolution during the first billion years. These findings also highlight a clear a gap in our knowledge, between massive star-forming galaxies at $z > 6$ and already-old quiescent galaxies at $z \sim 2$.

Recent studies have begun to bridge this gap, spectroscopically confirming the first massive quiescent galaxies at $z > 3$ (e.g., [9]). Such objects provide highly valuable insights into how baryonic feedback processes first began to arrest the extremely vigorous star formation observed in the earliest galaxies. However, the rarity, faintness and red colour of these objects make spectroscopic studies with existing instrumentation highly challenging. At present, only three secure spectroscopic red-shifts exist for quiescent galaxies at $z > 3.5$ [10, 11]. These are based on low-SNR K-band data, which does not include the near-UV Balmer/4000Å break region critical for precise age determination (e.g., [12]), or the Hα emission line critical for precise SFR determination.

To make further progress there is now an urgent need for the improved sensitivity and broader, redder wavelength coverage that can only be provided by the James Webb Space Telescope (JWST). This will allow the full spectral fitting methods recently proven at $z \sim 1 - 2$ to be extended, providing strong constraints on the SFHs and stellar metallicities of the earliest and most extreme massive quiescent galaxies, opening a new window on galaxy formation during the first billion years.

My JWST Cycle 1 program [13] will obtain deep NIR-Spec spectroscopy of the highest-redshift known massive quiescent galaxy, GOODSS-9209 at $z = 4.657$ [14]. Figure 2 shows the SFH of GOODSS-9209. The top panel shows current constraints from photometric data. It can be seen that a range of different formation scenarios are consistent with photometric constraints, from slow, sustained star formation over ~ 1 Gyr to a monolithic collapse scenario over < 100 Myr. The constraints my NIRSpec data will provide are shown in the lower panel, along with mock spectroscopy from the JWST ETC. It can be seen that these new data will clearly distinguish between formation scenarios.

References
[1] Ocvirk, P., et al. 2006, MNRAS, 365, 46
[2] Carnall, A. C., et al. 2019, ApJ, 873, 44
[3] Leja, J., et al. 2019, ApJ, 876, 3
[4] Dunlop, J., et al. 1996, Nature, 381, 581
[5] Cimatti, A., et al. 2004, Nature, 430, 184
[6] Carnall, A. C., et al., 2019, MNRAS,490, 417
[7] Carnall, A. C., et al., 2021, arXiv:2108.13430
[8] Carnall, A. C., et al., 2018, MNRAS, 480, 4379
[9] Schreiber, C., et al. 2018, A&A, 618, A85
[10] Glazebrook, K., et al. 2017, Nature, 544, 71
[11] Valentino, F., et al. 2017, ApJ, 889, 93
[12] Kauffmann, G., et al., 2003, MNRAS, 341, 33
[13] Carnall, A., et al. 2021, JWST Proposal, Cycle 1
[14] Carnall, A., et al. 2020, MNRAS, 496, 695

Short CV

2011–2015: MPhys Physics and Astronomy, Durham University, UK
2015–2019: PhD Astrophysics, Edinburgh University, UK
2019–2021: Postdoctoral Research Assistant, Edinburgh University, UK
2021–2024: Leverhulme Early Career Fellow, Edinburgh University, UK
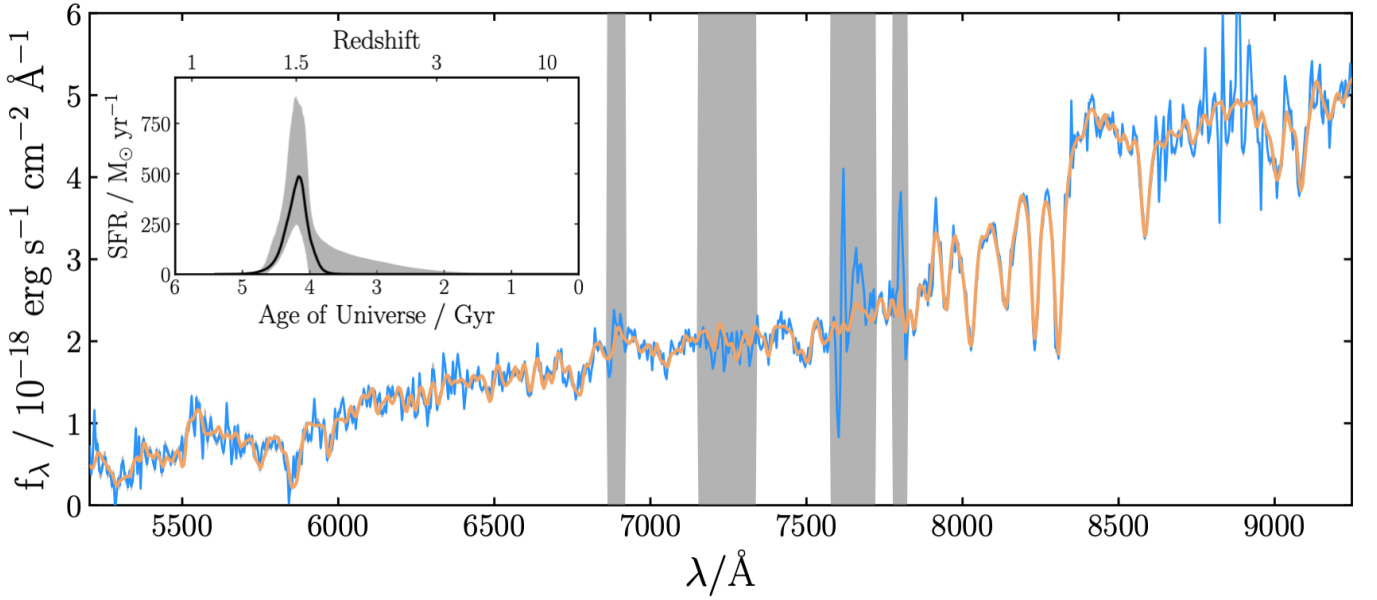
Figure 1: A spectrum for an example galaxy is shown in blue, with the best-fitting Bagpipes model overlaid in orange. This analysis allows us to recover the SFH for this galaxy (inset panel), providing insights into the processes driving its evolution. Taken from [6].
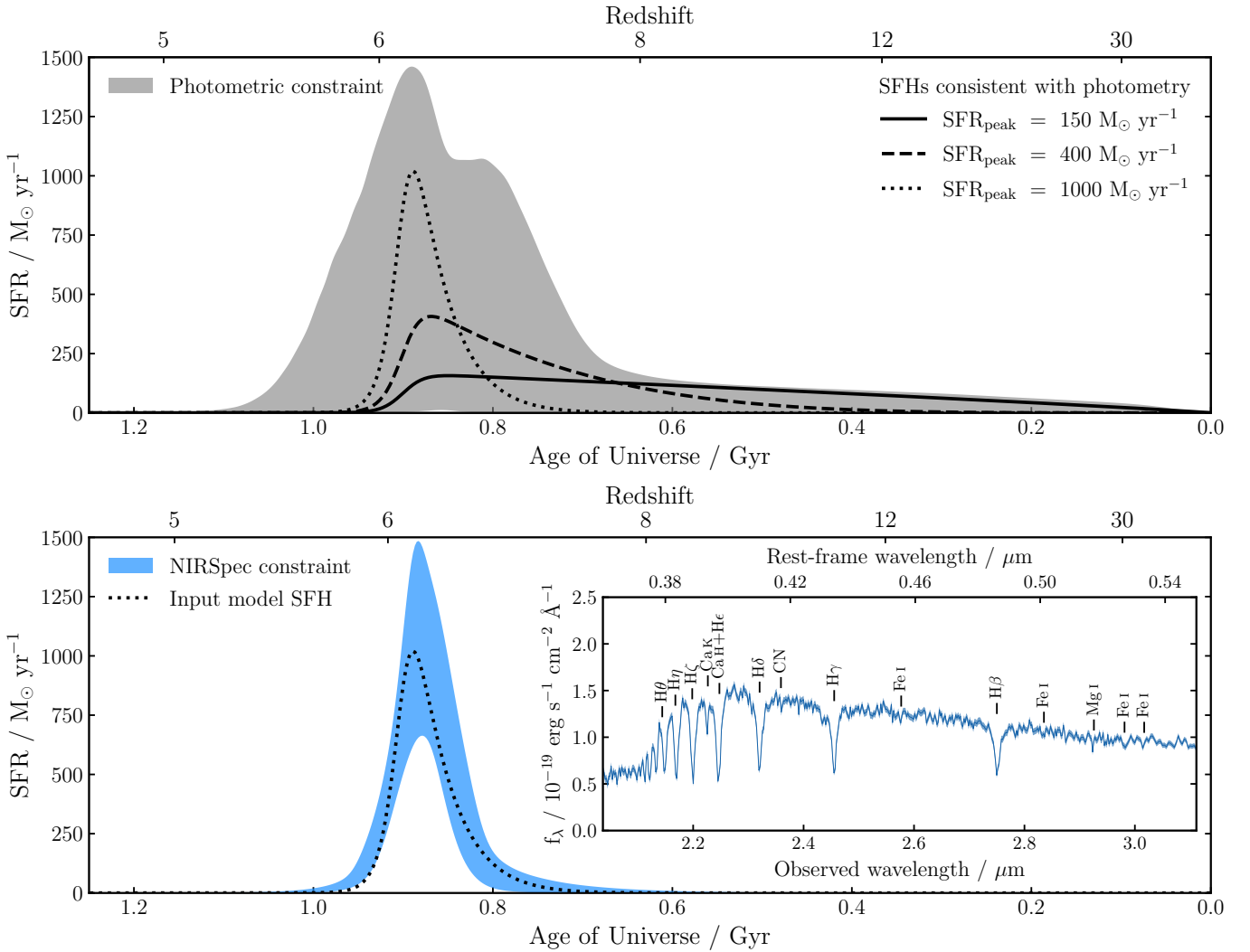
Figure 2: The SFH of GOODSS-9209. Constraints from photometry are shown in gray. The shaded region is the 95 per cent confidence interval. Constraints from Bagpipes full spectral fitting of mock NIRSpec data from my upcoming JWST program [13] are shown in blue. The mock data, shown in the inset, were generated with the JWST ETC using the dotted SFH as input. It can be seen that my NIRSpec data will clearly distinguish between rapid, SMG-like and more gradual formation scenarios.

Modelling galaxy emission-line kinematics using self-supervised learning

James Dawson

Cardiff University, The Parade, Cardiff CF24 3AA, Wales, UK

The 21-cm atomic Hydrogen (HI) line is often used by astronomers to study outermost regions of galactic discs (e.g., [1, 2, 3, 4, 5]). Marking the continuous boundary between galactic discs and their surrounding environments, measured rotation HI curves can be used to probe the properties of the dark matter halos within which galaxies are thought to reside. Within the disc, HI observations are useful in studying the gaseous content of galaxies as well as allowing astronomers to analyse the kinematic properties of substructures such as bars, warps, counter-rotating discs, and star-forming spiral arms (e.g., [6, 7, 8, 9]). Complementary observations of molecular gas (typically the CO molecule) can reveal the interplay between these gas phases and allows astronomers to build a more complete kinematic profile of galaxies. HI, typically being largely extended, allows astronomers to trace environmental properties such as extended tidal features and the existence of dwarf companions [3, 4, 5, 10, 11, 12], whereas CO is typically more centrally located within galactic discs, allowing astronomers to get a handle on the influence of central black holes on the disc kinematics (e.g., results from the mm-**W**ave **I**nterferometric **S**urvey of **D**ark **O**bject **M**asses –WISDOM– project).

The study of HI with adequate spatial and spectral resolution, requires the use of interferometers. Current state of the art interferometers collect raw data products of enormous size, and next generation interferometers are set to only be more powerful and data-hungry. Currently it is estimated that the **S**quare **K**ilometre **A**rray (SKA) will collect data on the order of hundreds of petabytes per year. This firmly pushes astronomy into the *big data era*. These kinds of data sizes are too large to exploit by hand, and are even too large to store. Therefore, astronomers should be looking to embrace a paradigm shift in which real-time models capable of efficient science are tested and deployed on incoming data. In this way physical information would be extracted from incoming data automatically, leaving the work of unravelling the prevailing science to astronomers.

A self-supervised, physics-aware, Bayesian, neural network

To this end we have developed a novel machine learning model with the primary goal of inferring the kinematic properties of gas discs in galaxies and an emphasis on extracting (simplistic) characteristics of their rotation curves. In the past decade, machine learning (ML) has become a popular solution to many *big data* challenges in galaxy evolution studies, but remains an under-utilised resource among the galaxy kinematics community. In previous work [13], we sought to address this using more conventional ML approaches. However, while conventional ML models are capable of high empirical accuracy and low testing time (e.g., [14, 15]), they are often plagued by slow training times [16] and, in some cases, poor generalisation to unseen data-sets [17, 18]. For next generation instruments like the SKA, where data cannot be efficiently stored, these qualities are unsuitable and therefore we look to use alternative methods which incorporate the benefits of ML, without the drawbacks associated with standard ML practice.
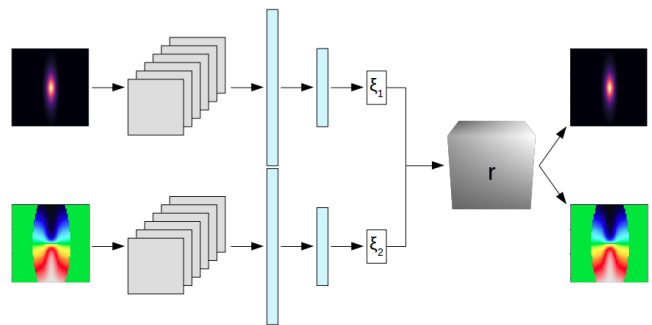

Figure 1: A simplified pictorial representation of the neural network used in this work. The model features two convolutional encoder subnets which concatenate learned features before passing them to a decoder subnet. The model receives moment maps as inputs and minimises the loss between decoder-generated moment map outputs and the inputs throughout training. In the diagram grey squares indicate convolutional layers, blue rectangles depict linearly connected layers, and the grey cube represents the auxiliary 3D cube containing the coordinate axes passed into the network.

The approach we turn to is *self-supervised learning*, whereby models train themselves, without the need for a labelled training set. This has huge benefits in that one no longer requires long training times on throwaway datasets, essentially eliminating data wastage completely. Few examples of physics-aware self-supervised learning approaches exist in astronomy (e.g., [19]) and, until now, none exist in the context of modelling galaxy kinematics.

The model itself, (shown in Figure 1), is a branched convolutional autoencoder. The encoder subnets extract lower dimensional feature representations from input images. In this case, as we are focused on models capable of working with interferometric data products, these are integrated intensity and mean velocity maps. Features are extracted from the maps using a combination of convolutional and linearly connected layers. The decoder then reconstructs the input images from the learned feature embeddings passed forward from the center of the

network. In a standard convolutional autoencoder, the decoder would make use of transposed convolution operations, however in this network the decoder is composed of analytical functions written using native `PyTorch`. By imposing this constraint, the CAE is forced to generate semantic encodings of the input images to pass to the decoder. In this way, we can be assured that the encoders are learning semantically meaningful properties of the input images and are no longer tied to traditional training methods, instead allowing the network to train on all available data (including test data) in a self-supervised manner. The model becomes *physics-aware* once the decoder functions are chosen as to reveal physically meaningful information about the input. For this work, the physics-awareness of the model refers to our focus on parameterising rotation curves and intensity profiles of galaxies. Therefore, our decoder functions explicitly take variables which describe these qualities.

Application to interferometric data

As part of our analysis, we tested the model by training on 17 galaxies observed using the **V**ery **L**arge **A**rray (VLA) as part of **T**he **H**I **N**earby **G**alaxy **S**urvey (THINGS) [20]. An example galaxy from this selection (NGC 2403) is shown in Figure 2.

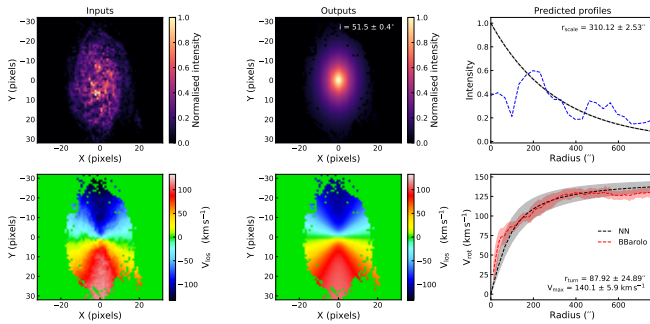**Figure 2:** NGC 2403, observed in HI and evaluated using the neural network model. The black dashed lines and grey areas show the mean and 1σ modelling errors respectively for profiles predicted by the neural network model. The blue dashed line shows a major axis cut of the input intensity map. The red dashed line and filled area show the best fit and associated errors modelled using `BBarolo`. The network predicted parameters are shown as text in the subplots.

In order to demonstrate the flexibility of this network architecture, we trained a model to recover the kinematic properties of CO line emission discs using the **A**tacama **L**arge **M**illimeter/submillimeter **A**rray (ALMA). Six galax-
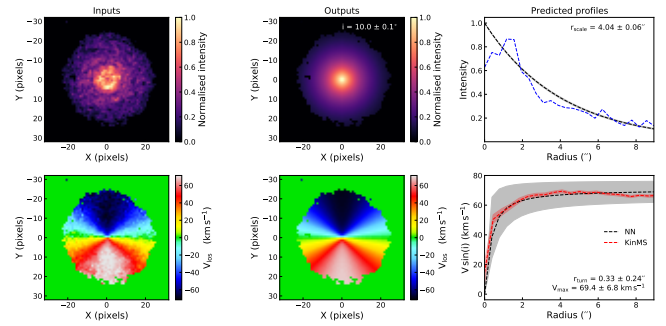

Figure 3: NGC 1387, observed in CO and evaluated using the neural network model. Figure style and layout matches that of Figure 2, with `KinMS` used for modelling comparison.

ies drawn from the WISDOM project, with high 'spatial resolution', were trained and tested on using our model.

Figures 2 and 3, show that the model is suitable for recovering rotation curves of galaxies from their kinematics. As well as removing the problem of throw-away training data-sets, our approach also overcomes the common issues associated with transfer learning when attempting to build practical models. The model architecture and training style presented in this work can be applied to a multitude of different data-sets with the possibility of architectural modifications suiting other types of data outside of interferometry (e.g., IFU data) and even astronomy.

References

[1] Warren, B. E., et al. 2004, AJ, 128, 1152
[2] Begum, A., et al. 2005, A&A, 433, 1
[3] Sancisi, R., et al. 2008, A&ARv, 15, 189
[4] Heald, G., et al. 2011, A&A, 526, 118
[5] Koribalski, B. S., et al. 2018, MNRAS, 478, 1611
[6] Józsa, G. I. G., et al. 2007, A&A, 468, 731
[7] Spekkens, K., & Sellwood, J. A. 2007, ApJ, 664,204
[8] Kamphuis, P., et al. 2015, MNRAS, 452, 3139
[9] Di Teodoro, E. M. & Fraternali, F., 2015, MNRAS, 451, 3021
[10] Hibbard, J. E., et al. 2001, ApJ, 122, 2969
[11] Serra, P., et al. 2013, MNRAS, 428, 370
[12] Bosma, A. 2016, Proc. IAU Symp., 220, 11
[13] Dawson, J. M., et al. 2019, MNRAS, 491, 2506
[14] Breiman, L. 2001, Machine Learning, 45, 5
[15] Krizhevsky, A., et al. 2012, ANIPS, 25, 1097
[16] Lim, T.-S., et al. 2000, Machine Learning 40, 203
[17] Dinh, L., et al. 2017, eprint:arXiv:1703.04933
[18] Kawaguchi, K., et al. 2017, eprint:arXiv:1710.05468
[19] Aragon-Calvo, M. A., & Carvajal, J. C. 2020, MNRAS, 498, 3713
[20] Walter, F., et al. 2012, ApJ, 136, 2563

Short CV

2013–2016:   BSc in Astrophysics, Cardiff University, UK
2016–2017:   MSc in Astrophysics, Cardiff University, UK
2017–present: PhD in Data Intensive Astrophysics, Cardiff University, UK

On the flaring of thick discs of galaxies: insights from simulations

Joaquín García de la Cruz

Astrophysics Research Institute, Liverpool John Moores University,

146 Brownlow Hill, Liverpool L3 5RF, UK

A new emerging picture for thick discs[††] is changing what was previously thought about them. Three main aspects of this new picture are: 1) large optical surveys concluded that thick discs were flat [1, 2], but more recent works have found flaring thick discs in external galaxies [3]; 2) the concept of thick discs as being red, old, and metal poor components of the galaxy is being replaced by one which allows thick discs to have both variety and complexity in their age structure, i.e., age gradients [4]; 3) the MW's thin and thick disc are not distinct components but form a continuum in terms of their structure and stellar populations [5, 6] but this is unknown for external galaxies. For this last point, it is worth mentioning that this transition could change depending on how the thin and thick disc are defined [7, 8].

Furthermore, it has been shown that while different Mono-Age Populations (MAPs) can have different levels of flaring, because of their radial surface density distribution, a flat thick disc can be recovered when all these stellar populations are superposed [9]. This also contributes to the idea that thick discs are indeed complex and probably do not form in a single event.

Here, we analyse in depth 27 galaxies from a sample of galaxies simulated in their cosmological context [10] to find the different flaring configurations of MAPs and their connection to the three aspects mentioned above. On top of that, we also look at the connections with the merger history of these simulated galaxies [11]. The peculiarity of these simulated galaxies is that they share many features with the MW. Their dark matter halos range masses between 2.7×10^{11} and 2×10^{12} $M_\odot$ and they live in relatively isolated environments, both agreeing with what we know of the MW. However, the sample also shows a large diversity of thick disc properties, which allowed us to study the connection between the formation history of a galaxy and its present day structure, and to place the MW in the context of the larger population of spiral galaxies.

Galaxies with flat thick discs

Flat thick discs or with minimal level of flaring form when MAPs barely flare or when, due to inside-out formation, the flared MAPs do not carry a lot of surface density at the flaring radii compared to younger, less flared MAPs. This is in agreement with previous studies [9] and an example of this can be found on the top panel of Figure 1. On Figure 2, the age gradient in the thick disc is represented against the slope of the thick disc for all the galax-

ies in our sample. The marker shapes indicate whether the thin and thick disc are different structures, and they are colour-coded by different galaxy features. It can be seen that when all galaxies in the sample are compared, galaxies with flat thick discs – occupying the most left part of Figure 2 – have some common features: they all have radial age gradients, and the thin and thick disc are a continuum as found in the MW [6, 12]. These galaxies also have have quiescent merger histories in the past 9 Gyrs, with the exception of galaxy g106 which had a merger at very early times −∼8 Gyr ago. This galaxy has been used in other studies for being the most MW-analog out of the galaxy sample [13].
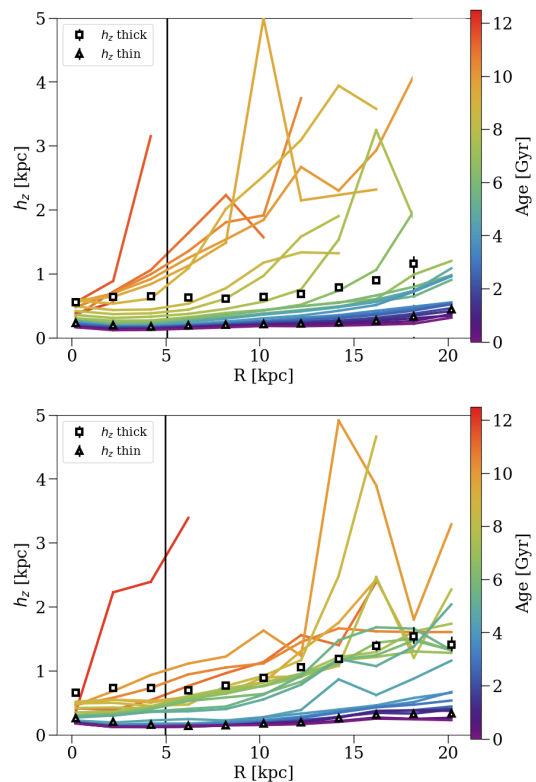
Figure 1: A galaxy with a flat thick disc on the top panel and a galaxy with a flared thick disc on the bottom panel. Values of the scale-height against radius for the thin disc (triangles), thick disc (squares), and MAPs (solid lines) colour-coded by age. MAPs from 9 to 11 Gyr and from 11 to 13 Gyr are binned together, every other MAP spans 0.5 Gyr. The vertical black line on the left represents the division between bulge and disc.

[††]Although very often the terms thin and thick disc refer to the α-poor and α-rich components of the Milky Way's (MW) disc respectively, hereafter we use them to refer to the thin and thick disc in geometrical terms, that is, a distinction based on the vertical distribution of the stellar density.

Although the number of galaxies is not high enough to do a proper statistical analysis, these results indicates that galaxies within certain mass range, disc thickness, age radial gradients in their thick disc, and the thin and thick disc forming a continuous structure, have quiescent merger histories. This is in agreement with what we know about the MW, including the discovery of the last major building block of the Galaxy, merging at early cosmological times.

Figure 2: Radial age gradient as a function of thick disc gradient, colour-coded by the mass ratio of the most massive merger in the la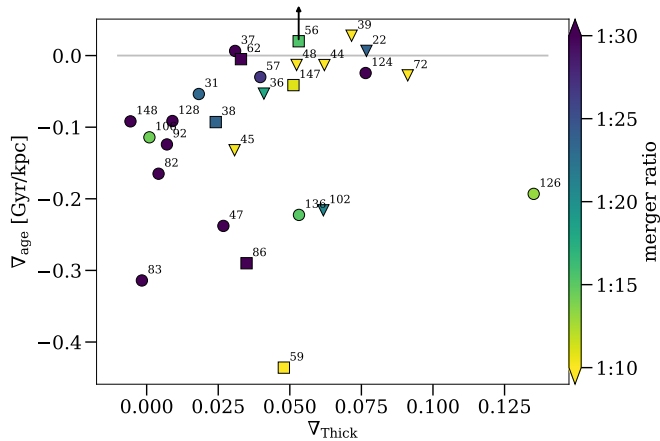st 9 Gyr. The marker shape represent whether there is no bimodality (circles), mild (squares), or strong bimodality (triangles).

Galaxies with flared thick discs

On the other hand, flared thick discs form when MAPs carry a significant amount of surface density where they flare. The flaring of the global thick disc can be driven by a sequence of different flaring MAPs at different radii, by only a few MAPs spanning a couple of Gyrs if those MAPs dominate the surface density throughout the disc, or if a group of MAPs share the same scale-heights. If one of the two last cases happens, then a bimodal structure is created and thin and thick disc are distinct components in terms of the stellar populations inhabiting them. An example of the third case can be seen in the bottom panel for Figure 1. This effect is directly related with the merger history [14]. Flared thick discs are more diverse than their flat counterparts in terms of age radial profiles as seen in Figure 2, although a high fraction of them show small or flat age radial profiles. We also found that galaxies that underwent massive mergers or with high mass ratios tend to have flat age radial profiles as seen in 2).

Conclusions

These results can help us understand the emerging picture where thick discs are more varied and complex than previously thought and many of their features are connected. Likewise, as data on nearby galaxies are becoming more abundant and detailed, it is becoming more important to connect and compare what we know about the MW with what we find in galaxies in our neighbourhood. Thus, theoretical studies like this one help to understand findings in nearby galaxies as well as find links between the MW and those galaxies. Ultimately, this will establish the place the MW within the context of its neighbouring spiral galaxies.

References
[1] Yoachim, P. & Dalcanton, J. J. 2006, ApJ, 131, 226
[2] Comerón, S., et al. 2011, ApJ, 741, 28
[3] Mosenkov, A., et al. 2020, MNRAS, 494, 1751
[4] Martig, M., et al. 2016, ApJ, 831, 139
[5] Bovy, J., et al. 2012, ApJ, 751, 131
[6] Mackereth, J. T., et al. 2017, MNRAS, 471, 3057
[7] Recio-Blanco, A., et al. 2014, A&A, 567, 5
[8] Hayden, M. R., et al. 2017, A&A, 608, 1
[9] Minchev, I., et al. 2015, ApJL, 804, L9
[10] Martig, M., et al. 2012, ApJ, 756, 26
[11] García de la Cruz, J., et al. 2021, MNRAS, 501, 5105
[12] Bovy, J., et al. 2012, ApJ, 753, 148
[13] Minchev, I., et al. 2016, ApJ, 834, 27
[14] Martig, M., et al. 2014, MNRAS, 443, 2452

Short CV

2015:	Degree & Master in Physics, Universidad de Granada, Spain
2017:	Teaching assistant, Pomona College, USA
2020:	Placement in Data Science, eDreams Odigeo, Barcelona, Spain
2017–present:	PhD in Astronomy, Liverpool John Moores University, UK

How do nuclear star clusters form?

Katja Fahrion

European Southern Observatory, Karl-Schwarzschild-Strasse 2, 85748 Garching bei München

As their name suggests, nuclear star clusters (NSCs) are dense star clusters located in the nuclei of galaxies. NSCs have masses between $10^5 - 10^8$ M$_\odot$ and half-light radii of $3 - 10$ pc (see the recent review [1] and references therein), making them among the densest stellar systems in the Universe with densities that can even surpass those of globular clusters (GCs).

Photometric studies of large samples of galaxies have established that at least 70% of all galaxies have an NSC in their centre (e.g., [2, 3, 4]). This nucleation fraction is a function of galaxy mass and peaks at $M_{\rm gal} \approx 10^9$ M$_\odot$, where more than 80% of all galaxies are nucleated, while less than 10% of galaxies with masses below 10^6 M$_\odot$ or above 10^{11} M$_\odot$ host an NSC [5, 6].

NSCs often co-exist with supermassive black holes, for example in the Milky Way, and they seem to follow similar scaling relations that connect their properties to properties of the host galaxy (e.g., [7, 8, 9, 10, 5]). The existence of such relations connecting vastly different spatial scales hints towards a connected evolution of the NSC and its host galaxy, but the formation mechanisms of NSCs and their dependence on galaxy properties are debated.

Formation mechanisms

In general, two pathways for NSC formation are discussed: the in-situ formation scenario, where the NSC forms at the galaxy's centre from infalling pre-enriched gas (e.g., [11, 13]), and the gas-free merger of GCs that spiral inwards due to dynamical friction (e.g., [14, 15, 16]). Also composite scenarios have been proposed and most likely both channels are realised in Nature [17, 1], but their relative contributions in different galactic environments are still unclear.

The two NSC formation channels impart different expectations for the stellar population properties of the NSC in comparison to the host galaxy and the GCs. In the GC accretion scenario, the NSC should reflect the stellar populations of the accreted GCs, explaining the old, metal-poor stellar populations of NSCs in some dwarf early-type galaxies [18, 19]. In contrast, the in-situ formation channel is usually invoked to explain the presence of young stars, extended star formation histories with multiple star forming episodes and metal-rich populations that exceed the metallicity of the host galaxy [20]. Constraining the dominant NSC formation channel therefore requires a panoramic view of the stellar population properties (ages, metallicities, star formation histories) of the NSC in comparison to the stellar body of the host galaxy and the GCs. The Multi Unit Spectroscopic Explorer (MUSE), an integral-field spectrograph mounted at ESO's Very Large Telescope in Chile, allows such a simultaneous study of all the involved components.

Comparing a massive and a dwarf galaxy

To explore NSC formation in different galactic environ-ment, it is illustrative to first consider individual case studies. Here, we compare the massive early-type galaxy FCC 47 ($M_{\rm gal} \approx 10^{10}$ M$_\odot$) in the Fornax galaxy cluster ($D \approx 20$ Mpc) to the dwarf galaxy KK197 ($M_{\rm gal} \approx 10^7$ M$_\odot$) which is a satellite of Centaurus A at a distance of ≈ 4 Mpc. Both galaxies span roughly the same extent on the sky and are nucleated, but the NSC in FCC 47 has a mass of $\approx 7 \times 10^8$ M$_\odot$, while KK197 hosts a low-mass NSC with $M_{\rm NSC} \approx 10^6$ M$_\odot$.

Analysis of the MUSE data of both galaxies shows further differences (see [21] and [18]). FCC 47 shows a peculiar kinematic structure and its massive NSC is kinematically decoupled, while KK197 only exhibits low-amplitude rotation. In addition, both galaxies show different radial metallicity profiles (Figure 1). While the NSC in FCC 47 is the most metal-rich component in the galaxy, the NSC of KK197 is significantly more metal-poor than the galaxy and shares the low metallicity of a nearby GC.
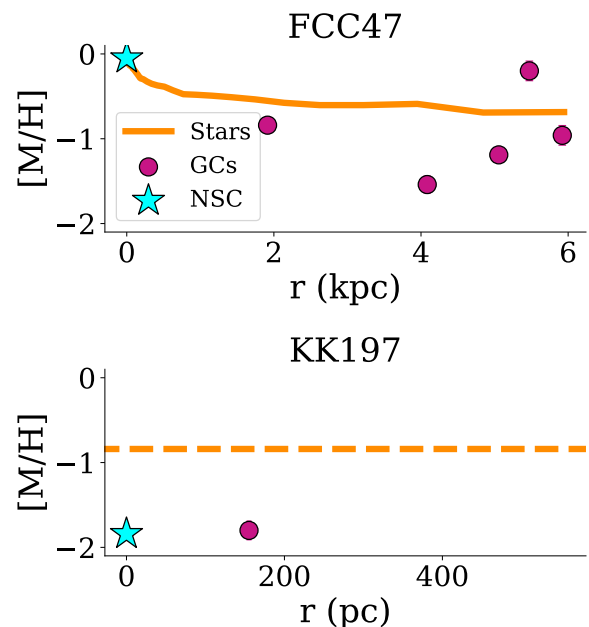
Figure 1: Radial metallicity profiles of FCC 47 (top) and KK197 (bottom), showing the metallicities of NSCs (blue stars) and GCs (pink circles) in comparison to the stars (orange). The data quality of KK197 was insufficient to get a profile, so the dashed line shows the average value. Adapted from [21] and [18].

These results indicate that these two NSCs were formed through different formation processes. The low-mass, metal-poor NSC shares many of its properties with typical metal-poor GCs and, hence, is likely the product of the GC accretion scenario. In contrast, forming the massive, metal-rich and kinematically decoupled NSC of FCC 47 through metal-poor, low-mass GCs seems unlikely. It is probable the result of efficient in-situ star formation, although the kinematically decoupled nature indi-

cates that this NSC was further shaped by a merger process that has altered the kinematic structure of FCC 47.

A trend with galaxy mass?

The two case studies therefore illustrate that both processes are realised in Nature, but possibly in different galactic environments. Hence, to test whether there exists a dependence of the dominant NSC formation channel with galaxy properties, we can investigate a larger sample of 25 early-type galaxies in the Fornax and Virgo galaxy clusters with similar techniques (see [22]).

A background-cleaned extraction of the NSC spectra enables us to compare their stellar population properties to the underlying host galaxy. Metallicity profiles similar to those presented in Figure 1 can be used to identify metal-poor NSCs and by including also information on stellar ages, young populations indicative of ongoing in-situ formation are detected. In addition, star formation histories (SFHs) of the NSCs reveal more detail in comparison to the host galaxies (Figure 2). For example, while the SFHs of the massive galaxy FCC 170 and its NSC only show a single old and metal-rich component, the NSC SFH of the dwarf galaxy FCC 202 shows a minor metal-rich and young population in addition to a dominating old and metal-poor component. These two populations directly indicate that both NSC formation channels have acted in the assembly of this NSC.
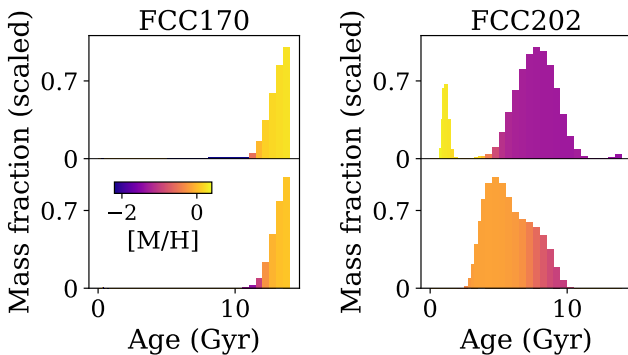

Figure 2: SFHs of the NSCs (top) and the host galaxy (bottom) of two galaxies, FCC 170 and FCC 202. Each bin is coloured by the mean metallicity. Adapted from [22].

Based on such stellar population analysis, it is possible to explore trends of the dominant NSC formation channel with galaxy and NSC mass, as shown in Figure 3. This figure clearly reveals that the dominant NSC formation channel changes from GC accretion to in-situ star formation with increasing galaxy and NSC mass. Low-mass NSCs in low-mass galaxies form predominantly through the merger of GCs as evident from their

low metallicities, whereas high-mass NSCs located in massive galaxies assembled most of their mass through in-situ processes. This transition appears to happen at NSC masses $\approx 10^7$ $M_\odot$ and galaxy masses of $\approx 10^9$ $M_\odot$, and there are several galaxies at intermediate masses where both channels appear to have played a significant role in the formation of their NSC.
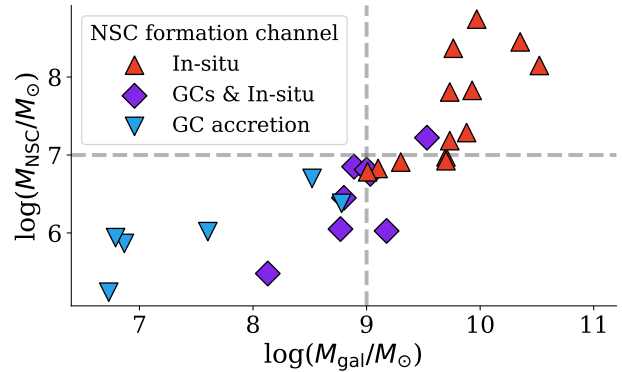

Figure 3: Galaxy versus NSC mass for the studied galaxies. Symbols indicate the dominant NSC formation channel as identified from stellar population analysis. Adapted from [22].

Although restricted to a small sample of 25 early-type galaxies, these results are fundamental for understanding NSC formation and their potential as unique probes of the evolutionary history of galaxy centres. The work presented in this talk lay the basis for future studies exploring NSC in different environments or galaxy types.

References

[1] Neumayer, N., et al. 2020, A&ARv, 28, 4
[2] Côté, P., et al. 2006, ApJS, 165, 57
[3] Turner, M. L., et al. 2012, ApJS, 203, 5
[4] Carlsten, S. G., et al. 2021, arXiv:2105.03440
[5] Sánchez-Janssen, R., et al. 2019, ApJ, 878, 18
[6] Hoyer, N., et al. 2021, arXiv:2107.05313
[7] Ferrarese, L., et al. 2006, ApJL, 644, L21
[8] Scott, N. & A. W. Graham 2013, ApJ, 763, 76
[9] Georgiev, I. Y., et al. 2016, MNRAS, 457, 2122
[10] Ordenes-Briceño, Y., et al. 2018, ApJ, 860, 4
[11] Mihos, J. C. & Hernquist L. 1994, ApJL, 437, L47
[12] Milosavljević, M. 2004, ApJL, 605, L13
[13] Bekki, K. 2007, PASA, 24, 77
[14] Tremaine, S. D., et al. 1975, ApJ, 196, 407
[15] Antonini, F., et al. 2012, ApJ, 750, 111
[16] Schiavi, R., et al. 2021, MNRAS, 503, 594
[17] Guillard, N., et al. 2016, MNRAS, 461, 3620
[18] Fahrion, K., et al. 2020, A&A, 634, A53
[19] Johnston, E. J., et al. 2020, MNRAS, 495, 2247
[20] Kacharov, N., et al. 2018, MNRAS, 480, 1973
[21] Fahrion, K., et al. 2019, A&A, 628, A92
[22] Fahrion, K., et al. 2021, A&A, 650, A137

Short CV

2012: Bachelor in Physics, Ruprecht-Karls Universität Heidelberg, Germany
2016: Master in Physics, Ruprecht-Karls Universität Heidelberg, Germany
2021: PhD in Astronomy, European Southern Observatory, Germany

Gamma rays from fast black-hole winds

Chris Karwin

Clemson University, Clemson, South Carolina 29634, USA

Black-hole winds from active galactic nuclei (AGN), also known as ultra-fast outflows (UFOs), are thought to contribute significantly to galaxy evolution and feedback, namely, the evolution of the bulge, the star formation, and the black hole growth [1]. The outflowing gas of a UFO may generate shock waves through interactions with the surrounding interstellar medium, which may subsequently produce γ-ray emission [2, 3, 4]. In this work we search for the γ-ray emission from UFOs using data collected by the Large Area Telescope (LAT; [5]) on board the *Fermi Gamma-ray Space Telescope*. Models of the γ-ray emission from UFOs [2, 4] show them to be weak emitters, with γ-ray luminosities of $\approx 10^{40}$ erg s^{-1}, which explains why UFOs have not yet been detected by the LAT. Here, we adopt a different strategy and search for the collective γ-ray emission from a sample of UFOs using a stacking technique.
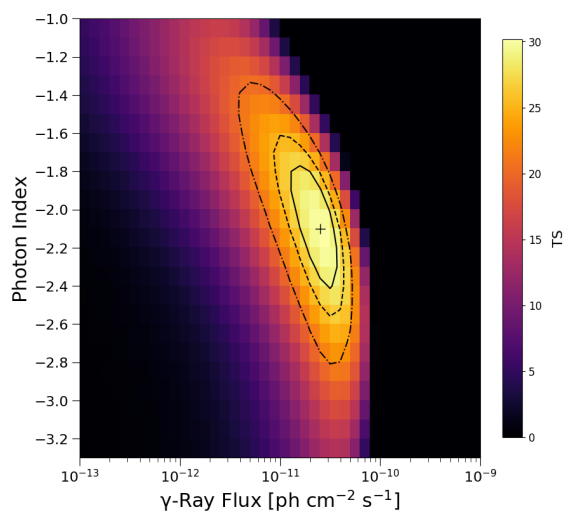

Figure 1: Stacked TS profile for the sample of UFOs. The color scale indicates the TS, and the plus sign indicates the location of the maximum value, with a $\mathrm{TS} = 30.1$ (5.1σ). Significance contours (for 2 degrees of freedom) are overlaid on the plot showing the 68%, 90%, and 99% confidence levels, corresponding to $\Delta\,\mathrm{TS} = 2.30$, 4.61, and 9.21, respectively.

Our sample consists of all nearby $(z < 0.1)$ UFOs with a mildly relativistic wind velocity $(v > 0.1c)$. The stacking technique we employ has been developed previously and has been successfully employed for multiple studies, i.e. upper limits on dark matter interactions [6], detection of the extragalactic background light [7], extreme blazars [8], and star-forming galaxies [9]. We evaluate the significance of each source using the test statistic (TS), which is defined as TS = -2log(L_0/L), where L_0 is the likelihood for the null hypothesis (i.e. no gamma rays

emitted from the UFO source), and L is the likelihood for the alternative hypothesis (i.e. γ-rays emitted from the UFO source). 2D TS profiles are generated for the spectral parameters of each UFO source. We scan photon indices from –1 to –3.3 with a spacing of 0.1 and total integrated photon flux (between 1–800 GeV) from 10^{-13} to 10^{-9} ph cm^{-2} s^{-1} with 40 logarithmically spaced bins. The TS profiles for all sources are added to obtain the stacked profile, which gives the statistical significance for the combined signal.

The stacked profile for our UFO sample is shown in Figure 1. The maximum TS is 30.1 (5.1σ), corresponding to a best-fit index of -2.1 ± 0.3 and a best-fit photon flux (1–800 GeV) of $2.5^{+1.5}_{-0.9} \times 10^{-11}$ ph cm^{-2} s^{-1}. The 68%, 90%, and 99% significance contours are overlaid on the map, and as can be seen the spectral parameters are well constrained.

We repeat the analysis with a sample of 20 low redshift $(z < 0.1)$ radio-quiet AGN that do not have UFOs. The sources were selected from the samples of [10] and [11] for which no UFO was found. The sample of [10] is based on absorption features, while the sample of [11] uses the excess variance method. No signal is detected from the control sample, with a maximum TS of 1.1. Using the profile likelihood method and a photon index of -2.0, the upper limit on the flux (1–800 GeV) at the 95% confidence level is 8.8×10^{-12} ph cm^{-2} s^{-1}. We have also shown that the γ-ray emission observed in the UFOs is a factor of $\sim$40 larger than what we would expect for star-formation activity, and that it's highly unlikely the UFO emission results from weak jets. This supports the interpretation of the γ-ray emission being due to the outflow rather than other processes in AGN.

The γ-ray luminosity from UFOs is predicted to scale with the AGN bolometric luminosity. To test this relationship we calculate the stacked profile in bins of bolometric luminosity. Additionally, we calculated the stacked profile in terms of efficiency, defined as $\epsilon_{\mathrm{Bol}} = L_\gamma / L_{\mathrm{Bol}}$. Results for this are shown in Figure 2. Indeed, we do find a scaling relation, and we measure the best-fit efficiency to be $(3.2 \pm 1.5) \times 10^{-4}$.

The physical model for the UFO SED is calculated by assuming that the γ-ray emission is dominated by hadronic processes resulting from diffusive shock acceleration. The observed γ-ray SED indicates a firm detection of cosmic ray (CR) protons with energies reaching at least as high as $\approx 10^{12-13}$ eV. Within our hadronic emission model we derive that on average the forward shock has traveled $\sim 20 - 300$ pc ($\sim 65 - 980$ light years) away from the supermassive black hole and that the maximum energy of protons accelerated at the forward shock is $\approx 10^{17}$ eV. This makes AGN winds a potential source of CRs with energies beyond the 'knee' of the CR spectrum (i.e., 3×10^{15} eV) and also likely contributors to the IceCube neutrino flux [13].
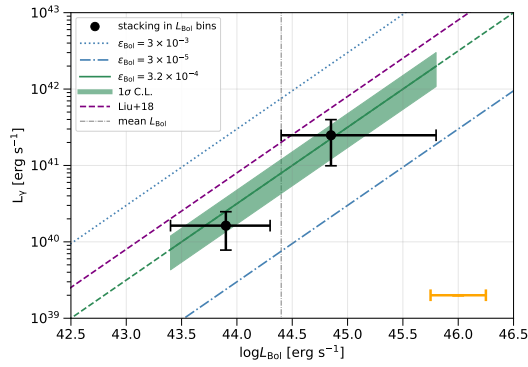
Figure 2: γ-ray luminosity versus bolometric luminosity. The black data points result from stacking in γ-ray luminosity, and the uncertainty in the x-axis corresponds to the bin widths. The grey dash-dot vertical lines show the value used to divide the bins. The solid green line shows the best-fit resulting from stacking in efficiency, with the green band showing the 1σ confidence level. For reference, the blue lines show a range of efficiencies within roughly an order of magnitude of the best fit. The orange bar shows the average one-sided uncertainty in individual measurements of AGN bolometric luminosity. We also overlay the predicted efficiency derived from [12] (dashed purple line).

References

[1] Tombesi, F., et al. 2013, MNRAS, 430, 1102
[2] Wang., X., & Loeb., A. 2016, 12, 1116
[3] Lamastra, A., et al. 2016, A&A, 596, A68
[4] Lamastra, A., et al. 2017, A&A, 607, A18
[5] Atwood, W.B., et al. 2009, ApJ, 697, 1071
[6] Ackermann, M.,et al. 2011, PhRvL, 107, 241302
[7] Abdollahi, S., et al. 2018, Sci, 362, 1031
[8] Paliya, V.S., et al. 2019, ApJ, 882, L3
[9] Ajello, M., et al. 2020, ApJ, 894, 88
[10] Tombesi, F., et al. 2010, A&A, 521, A57
[11] Igo, Z., et al. 2020, MNRAS, 493, 1088
[12] Liu, R.Y., et al. 2018, ApJ, 858, 9
[13] Aartsen, M.G., et al. 2013, Sci, 342, 1242856

Short CV

2013:	BSc, Physics, University of Colorado, Colorado Springs, USA
2017:	MSc, Physics, University of California, Irvine, USA
2019:	PhD, Physics, University of California, Irvine, USA
2019–present:	Postdoctoral Fellow, Clemson University, USA

(Re)solving reionisation with high-redshift analogues at cosmic noon

Jorryt Matthee

Department of Physics, ETH Zürich, Wolfgang-Pauli-Strasse 27, 8093 Zürich, Switzerland

Thanks to its intrinsic brightness and rest-frame UV wavelength, the Lyman-α line (Lyα, $\lambda_0 = 1215.67$ Å) is a key observable in studies of galaxies in the early Universe. Thousands of so-called Lyα emitters (LAEs) have been identified over $z \approx 2 - 7$ thanks to their strong Lyα emission, typically with wide-field narrow-band surveys or in IFU data-sets (e.g., [1, 2]). However, the role of the LAE population, for example their contribution to the cosmic star formation density or the cosmic ionising emissivity) is relatively unknown due to uncertainties and complexities in the Lyα radiative transfer that impact the fraction of produced Lyα photons that reach our telescopes.

Due to the high cross section, Lyα photons resonantly scatter in the presence of neutral hydrogen. This increases the travelled path length and therefore the possibility of dust absorption. The precise magnitude of this effect depends on the velocity field and column density distribution and clumpiness of neutral gas and dust in a complex way. This leads to the uncertainties in the escape fraction. However, another consequence is that the detailed properties of the Lyα line such as its line-profile offer the opportunity to trace the HI in and around galaxies. In particular, the Lyα line-profile can be used to constrain properties as the escape fraction of ionising photons (e.g., [3, 4]).

Empirically, however, the Lyα production rate, the escape fraction and the line-profile are poorly understood at high-redshift. This is due to the typical limited spectral resolution and the lack of rest-frame optical spectra required to measure the intrinsic luminosity and systemic redshift. Addressing these issues is the key motivation for undertaking the X-SHOOTER Lyman-α survey at $z = 2$ (XLS-$z2$; [5]).

The X-SHOOTER Lyman-α survey at $z = 2$

Currently, cosmic noon ($z \sim 2$) is the ideal redshift to study LAEs in detail. This is because i) a clean selection-function of LAEs is challenging to obtain at lower redshift as space-based UV spectroscopy is required, ii) redshift $z \approx 2$ is the highest redshift where Hα is observable from the ground, as it shifts out of the K_s band at $z > 2.5$. Without Hα, it is practically challenging to infer the nebular dust attenuation and therefore the intrinsic line-luminosity and iii) the age of the Universe is relatively short at $z \approx 2$, which makes the range of allowed star formation histories (SFHs) of LAEs comparable to the SFHs of very high-redshift galaxies.

We have undertaken the XLS-$z2$ survey using deep VLT/X-SHOOTER observations of 35 LAEs at $z \sim 2$. The typical exposure times are 3.5 hours and the X-SHOOTER data cover rest-frame wavelengths from $\lambda_0 \approx 1000 - 7000$ Å with a resolution $R \approx 4000 - 7000$.

The LAEs have primarily been selected using wide-field narrow-band surveys in well-known extra-galactic fields as COSMOS and UDS (see [5] for details). They are representative of the relatively bright (> 0.2 L*) LAEs that are commonly found in deep narrow-band surveys (e.g., [2]) or IFU observations (e.g., [1]). The typical stellar mass of the LAEs is 10^9 M$_\odot$, which is lower than the mass of continuum-selected star-forming galaxies that are commonly studied at $z \approx 2$. Systemic red-shifts are measured from rest-frame optical lines for 33/35 sources. The Lyα lines are observed with high S/N, see Figure 1 for a few examples. We find that the majority of Lyα lines (≈ 75 %) show a double-peaked profile with a dominant red peak.
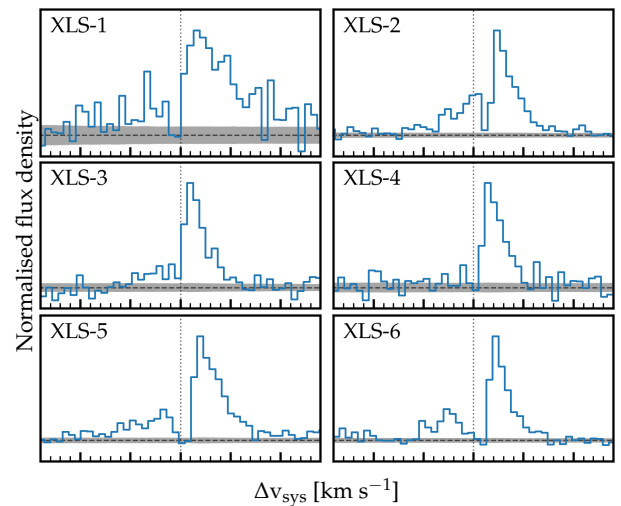
Figure 1: A few example Lyα profiles of XLS-$z2$ LAEs with a resolution of R≈ 4000 (adapted from [5]). Blue lines show the data and the grey shaded region illustrates the 1σ noise level. The velocity range of the spectra are centred on their measured systemic red-shifts. Lyα lines are characterised by a red-dominant double-peaked profile.

What makes galaxies LAEs?

The first fundamental question that we addressed with XLS-$z2$ is "What makes galaxies' LAEs?". This is of importance in order to extrapolate results on LAEs to the general galaxy population. Owing to the faintness of the individual LAEs, we used stacking techniques to obtain a detailed view of the average LAE [5]. The wide-band coverage of X-SHOOTER allowed measurements of faint absorption features from interstellar absorption lines (e.g., SiII), UV emission lines (e.g., HeII, CIV, OIII]), rest-frame optical lines ([OIII], [NeIII], Hβ, [OIII], Hα) that we used to infer the typical properties of LAEs at $z \approx 2$. We further used high-resolution rest-frame UV imaging data from *HST*/ACS. We find that:

- LAEs are characterized by an interstellar medium with little dust, a low $\approx 1/10$ $Z_\odot$ gas-phase metallicity, and a high ionization state.

- The ionizing sources in LAEs are young (≈ 10 Myr) hot stars that power the high equivalent widths of emission lines in the optical and high-ionization lines in the ultraviolet.

- The rest-frame UV morphology is clumpy. LAEs show outflowing kinematics with blue-shifted SiII absorption, a broad [O III] component, and a red-skewed Lyα line.

- Typically, 30 per cent of the Lyα photons escape, and a quarter of these photons escape on the blue side of the systemic velocity.

Figure 2: Illustration of the relevant properties that determine whether galaxies are observed as LAEs (left) or not (right). LAEs have young stars (blu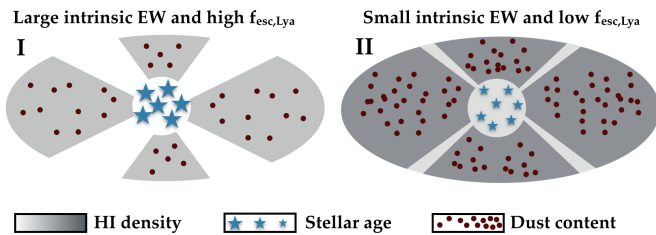e), a low dust content (red dots), a low HI column density (grey shade), and, possibly, HI-free channels (white channels). These conditions are more often present in low-mass galaxies than in high-mass galaxies at $z \approx 2$.

Figure 2 summarises a physical picture of the properties that we identify to determine whether galaxies are observed as LAEs. A low dust content and an on-going starburst are prerequisite in order to be a LAE. These conditions are common in relatively low-mass galaxies and this therefore explains – to first order – why LAEs have lower masses than typical continuum-selected galaxies. However, at fixed mass, LAEs are not particularly dust-free, nor are the stars particularly young. Therefore, we conclude that especially the *effective* HI column density determines the apparent Lyα luminosity of a galaxy. This could be either related to outflows that disperse the gas and create HI-free channels, or due to a fortunate viewing angle. Future comparable observations of carefully-matched samples (i.e. in mass, attenuation and star formation activity) of non-LAEs can distinguish which of these effects is most important.

Ongoing work to (re)solve reionisation

In [5], we argue, based on luminosity functions and Lyα statistics, that the conditions that facilitate Lyα escape are relatively rare at $z \approx 2$, but appear more common in the very early Universe (i.e. $z > 6$). It is therefore of interest to measure the contribution of LAEs to the ionising emissivity, which particularly requires us to know their escape fraction of ionising photons (LyC photons). In ongoing work, we are analysing the variety in the Lyα line-profiles (e.g., Figure 1) as a way of indirectly inferring the LyC escape fraction [3]. While this is admittedly indirect, we note that such measurement of the escape fraction is not subject to the stochasticity in sightlines through the intergalactic medium that plagues direct LyC measurements in individual galaxies at high-redshift.

Our tentative results are very promising: we find that half the LAEs at $z \approx 2$ have line-profiles suggestive of a high (> 20 %) escape fraction of ionising photons, while few ionising photons escape from other LAEs. The LyC-leaking subset of LAEs *simultaneously* shows remarkably different properties in the ISM and stellar populations, with a lower dust attenuation, weaker interstellar absorption, gas that is optically thin to MgII photons and younger and (much) hotter stellar populations [6]. This demonstrates that the phase during which galaxies have an ISM structure that allows the leakage of ionising photons coincides with the time when the hottest stars shine their ionising photons.

Thanks to the well-defined selection function of XLS-$z2$ we can place these results into a cosmological context. If we assume the ionising properties (i.e. production and escape) of LAEs to be redshift-invariant, bright LAEs form the sub-population of the star-forming galaxy population that dominates the ionising emissivity at early times and, together with quasars, explains the evolution of the ionising background over $z \approx 2-8$. A small fraction of the total galaxy population is thus an effective ioniser, and the LAE statistics allow us to explain how this fraction increases strongly with redshift (with the population-averaged escape fraction increasing by $\propto (1+z)^3$ from $z \approx 2-8$). Simultaneously, a Lyα-luminosity linked ionising contribution yields an optimal stellar mass of $\approx 10^8$ M$_\odot$ of the galaxies that are contributing most to the emissivity [7]. In the future, we aim to test this LAE-framework by extending observations to fainter luminosities and higher red-shifts. This will particularly benefit from joint spectroscopic observations of VLT/MUSE and the *James Webb Space Telescope* tracing the rest-frame ultraviolet and optical of galaxies at $z > 3$, respectively.

References
[1] Herenz, C., et al. 2019, A&A, 621, 107
[2] Sobral, D., et al. 2018, MNRAS, 476, 4725
[3] Izotov, Y., et al. 2018, MNRAS, 478, 4851
[4] Verhamme, A., et al. 2015, A&A, 578, 7
[5] Matthee, J., et al. 2021, MNRAS, 505, 1382
[6] Naidu, R.P. et al., in prep.
[7] Matthee, J., et al., in prep.

Short CV

2014: Master in Astronomy, Leiden University, The Netherlands
2018: PhD in Astronomy, Leiden University, The Netherlands
2018–present: Zwicky Fellow, ETH Zurich, Switzerland

Unveiling the chemical composition of the Small Magellanic Cloud

Alice Minelli

Dipartimento di Fisica e Astronomia - Alma Mater Studiorum Università degli Studi di Bologna

Via Gobetti 93/2, I-40129 Bologna, Italy

INAF - Osservatorio di Astrofisica e Scienza dello Spazio di Bologna

Via Gobetti 93/3, I-40129 Bologna, Italy

The Small Magellanic Cloud (SMC) is an excellent laboratory to investigate the chemical enrichment history of a galaxy that has experienced strong gravitational interactions with other systems, since it is in an early stage of a minor merger event with the Large Magellanic Cloud. Despite its proximity ($\sim$ 60 kpc) and the possibility to resolve its stellar content, the chemical composition of the SMC is still poorly known. In order to fill this gap and to accurately reconstruct the chemical evolution of the stellar populations in the SMC, we analysed FLAMES@VLT high-resolution spectra of about 200 red giant stars belonging to the SMC field. Additionally, we analysed stars that are members of three SMC clusters with different ages ($\approx$11, $\approx$6, and $\approx$1 Gyr), covering the entire range of ages of the SMC clusters system. This data-set allows to reconstruct the role played by the different contributors to the chemical enrichment, i.e. Type II and Ia supernovae, hypernovae, and AGB stars. In particular, most of the stars (both in the field and in clusters) have solar-scaled [α/Fe] ratios, indicating that they formed from a gas already polluted by Type Ia supernovae. Among the field stars, we identified a bunch of rare SMC metal-poor stars ([Fe/H]<-2.0) that allow to study the early chemical enrichment of the galaxy. Finally, we found evidence of a metallicity gradient within the SMC, with metallicity decreasing moving outward.

The Small Magellanic Cloud

The SMC is on a early stage of a minor merger with the Large Magellanic Cloud (LMC) [1] and, together, they are on a first approach to the Milky Way (MW) [2]. These gravitational interactions influence the star formation of the galaxy with numerous bursts connected to the close passages between the Clouds [3]. The star formation is still ongoing in the SMC.

Analysed targets

We analysed both field and globular clusters (GCs) stars in the SMC. About 200 field stars have been observed around three GCs located in different regions of the galaxy. The stars were picked from the Gaia CMDs, selecting those located in the bright portion of the red giant branch. The three GCs were chosen in order to cover the entire range of ages of the SMC GCs, and 20 stars are observed among them. Both field and cluster samples have been obtained with high resolution FLAMES@VLT spectra. The two samples give complementary information, since field stars provide high statistics and the metallicity in different locations of the galaxy, allowing us to study the evolution of the chemistry with the po-

sition. Instead, GCs provide simultaneously the age and the metallicity of the stars, allowing us to study the evolution of the chemistry with the time.

Spectral analysis

The spectral analysis was made in a homogeneous way for both samples, in order to erase the presence of systematics due to different methods. This means that the analysis was made using the same approach to derive the chemical abundances, the same atomic data and model atmosphere and the same solar value. In this way, a difference in the chemical abundances had to be attributed to a real difference in the chemical composition of the stars.

Results

The study of the field stars sample leads to the following results:

(1) the total metallicity distribution (Figure 1) shows a peak at [Fe/H] ≈ -1 dex, as previously derived from low resolution study [5], with a tail at low metallicity;

(2) the metallicity distribution changes with the location in the galaxy, in particular the peak value remains nearly constant, but moving toward the external region of the galaxy, the fraction of metal poor stars increases;

(3) 12 stars with [Fe/H] < -1.5 dex are detected;

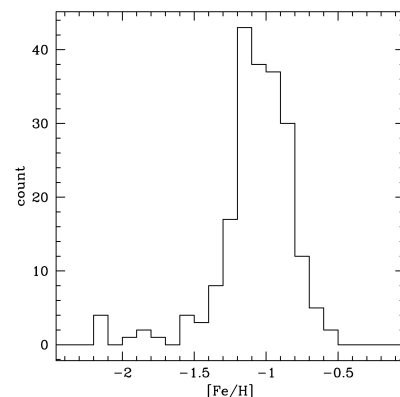**Figure 1:** Total metallicity distribution of the field stars.

(4) the α-elements abundance ratios of the SMC field stars (Figure 2) are lower with respect to the MW stars with similar metallicity. This difference is explained by a slower star formation rate of the SMC in comparison to the MW. Moreover, the hydrostatic α-elements (O and Mg), synthesized in stars with masses M > 30 $M_\odot$, are

more depleted than the explosive α-elements (Si, Ca and Ti), produced in stars with masses 15 M$_\odot$ < M < 25 M$_\odot$. The difference is explained with a lower contribution by massive stars in the chemical enrichment history of the SMC in comparison to the MW.

The results obtained from the chemical abundances of stars belonging to the three GCs of different ages are:
(1) the metallicity of the stars, combined with their ages, confirms the age-metallicity relation previously derived theoretically by [4]. In particular, in the first 2 Gyr, the SMC reached a metallicity of about -1.2 dex, keeping this value constant at least until 6 Gyr ago. Then, the metallicity started to increase, reaching a value of -0.6 dex, 1.5 Gyr ago.
(2) The three GCs have solar scaled α-elements abundances, another indication of a slower star formation rate of the SMC with respect to the MW.
(3) No evidence of multiple stellar populations is found from Na and O abundances of the analysed targets.

From the comparison between the metallicity of the field stars and the ones of the GCs, we can suppose that the most metal poor stars were formed in the first 1-2 Gyr (green shadow in Figure 3). From these stars, we can derive information on the early chemical enrichment history of the SMC. Moreover, the bulk of the field stars sample, peaked at -1 dex, were likely formed around 3-4 Gyr ago (green shadow in Figure 3), the epoch of the first encounter between the Clouds [1], which probably reactivated the star formation in the SMC.
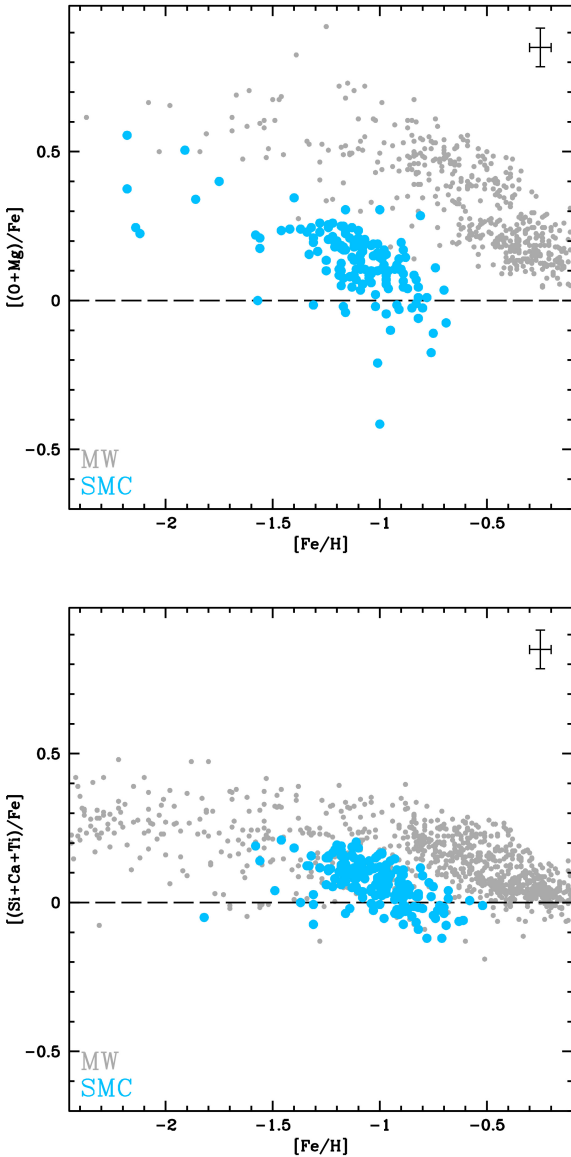
Figure 2: Behaviour of the hydrostatic and explosive [α/Fe] abundance ratio (top and bottom panel, respectively) as a function of [Fe/H] for SMC field stars (light blue) and MW literature data (grey).
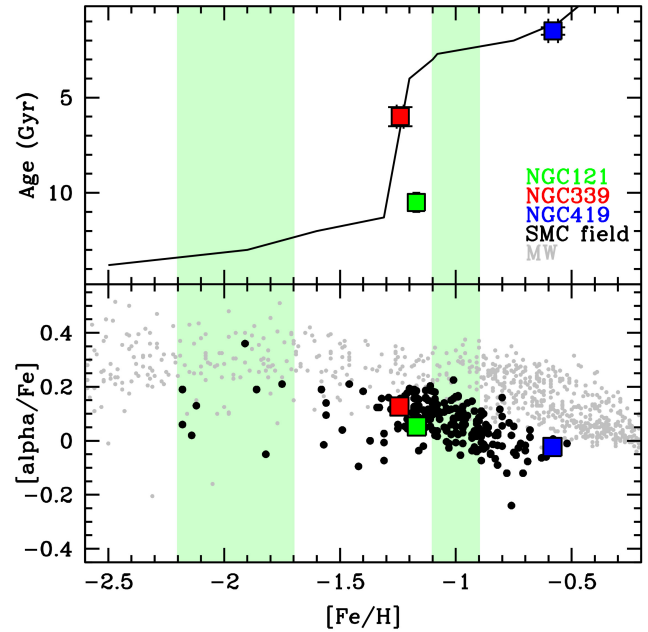
Figure 3: Age-metallicity relation in the top panel for SMC GCs compared with the theoretical model of [4]. In the bottom panel, [α/Fe] abundance ratio as a function of the [Fe/H] for the SMC GCs (colored squares), SMC field stars (black dots) and MW literature data (grey dots).

References
[1] Bekki, K., & Chiba, M. 2005, MNRAS, 356, 680
[2] Besla, G., et al. 2007, ApJ, 668, 949
[3] Harris, J., & Zaritsky, D. 2009, AJ, 138, 1243
[4] Pagel, B. E. J., & Tautvaisiene, G. 1998, MNRAS, 299, 535
[5] Parisi, M. C., et al. 2016, AJ, 152, 58

Short CV

2016:   Bachelor degree in Astronomy, University of Bologna, Italy
2018:   Master degree in Astrophysics and Cosmology, University of Bologna, Italy
2018–present: PhD in Astrophysics, University of Bologna, Italy

47

Evidence of a dynamically evolving Galactic warp

Eloisa Poggio

Université Côte d'Azur, Observatoire de la Côte d'Azur, CNRS, Laboratoire Lagrange, France

Osservatorio Astrofisico di Torino, Istituto Nazionale di Astrofisica (INAF), I-10025 Pino Torinese, Italy

The Galactic disc exhibits a large-scale distortion of the outer parts with respect to the inner parts [1], commonly known as *the Galactic warp* (Figure 1). While numerous models have been proposed to explain its origin and dynamical nature (including intergalactic magnetic fields [2], a misaligned infall of gas [3], the influence of a satellite galaxy [4], a torque from the dark matter halo of the Galaxy [5]), which mechanism is actually at work remains unclear. Thanks to the unparalleled wealth of astrometric information from the Gaia satellite [6, 7, 8, 9], stellar kinematics in the Galactic disc can be analysed, with the aim of constraining the warp's dynamical nature.

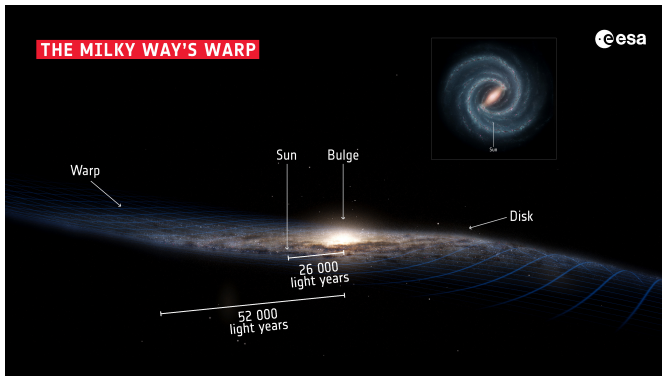**Figure 1:** The structure of our Galaxy, the Milky Way, with its warped galactic disc. This figure has been created for the ESA press release of the paper presented here [10]. Credit: Stefan Payne-Wardenaar; Inset: NASA/JPL-Caltech; Layout: ESA. ESA press release: `https://www.esa.int/Science_Exploration/Space_Science/Gaia/Milky_Way_s_warp_caused_by_galactic_collision_Gaia_suggests`.

The temporal evolution of the Galactic warp

Using the collisionless Boltzmann equation, a simple model of how the warp orientation changes with time can be constructed. In general, the modelled warp can vary its amplitude and line-of-nodes (see Figure 2 and animated version, details in [10]) as a function of time. Depending on the magnitude and direction of such variations, different signatures are expected in the present-day vertical velocities of stars. When the warp figure is frozen in time, and only the line-of-nodes is changing its azimuthal angle, the kinematic signature manifests itself as systematic vertical velocities along the line-of-nodes toward the outer parts of the disc. The variation of the warp line-of-nodes is sometimes called in the literature warp *precession* (or warp angular speed), and we therefore call this model the *long-lived precessing warp*. If we, instead, set to zero all temporal variations, we obtain the so-called *static* warp model. Taking advantage of *Gaia* data, it is now possible to tackle outstanding questions about how (and if) the warp is evolving as a function of time. As discussed in the following, observational constraints on the warp kinematics would be particularly useful to learn more about the evolutionary history of the Galactic disc.
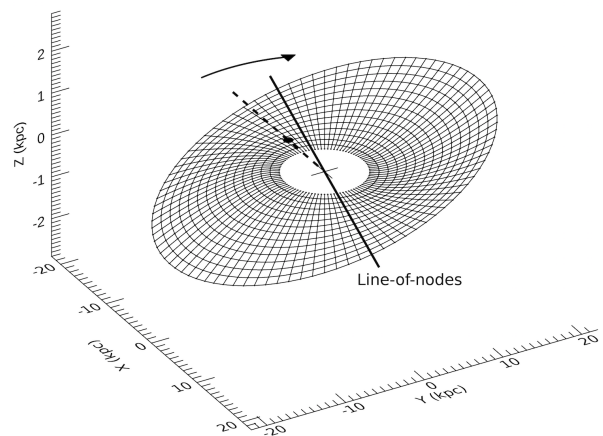
Figure 2: Three-dimensional representation of the precessing warp model. The Sun's position is shown by the dot, the Galactic Centre by the black cross and the direction of Galactic rotation by the arrow. The angle between the warp's line of nodes (bold solid line) and the Sun's azimuth ($\phi = 0^o$, dashed line) is the warp phase angle at the present time. Taken from Fig. 2 of ref. [10]. An animated version is available in Supplementary Video 1 of ref. [10].

Measuring the warp precession

Using astrometric information from Gaia Data Release 2 [8] for 12 million giant stars (details on the sample in [11]), together with a model for the structure and kinematics of the Galactic disc (including the above-discussed warp model), astrometric uncertainties and survey selection function, we measured the warp precession rate. For a given set of parameters, the estimated value of warp precession is degenerate with some of the assumed parameters, e.g., the mean azimuthal stellar velocity, the assumed parallax zero-point for Gaia data [12], and the assumed warp amplitude. For this reason, we tested several values of these parameters available in the literature. Specifically, for the warp amplitude, we explored spatial geometries from [13], which [14] found in good agreement with their distribution of RGB (red giant branch) stars, a stellar population similar to the one we adopted; we also used the model from [15] based on red-clump stars at $R \lesssim 13$ kpc (according to the spatial limitation of that model); we tested the parametrisations from [16],

based on 2MASS star counts, and the stellar model from [17]. Additionally, we tested the geometry from [18] based on Cepheids, a stellar population different from the one we adopted, but for which precise distance estimates can be obtained. Indeed, the geometry of the Galactic warp is quite uncertain for several reasons: part of this uncertainty comes from the fact that different stellar populations might have intrinsically different amplitudes, and part is due to the different techniques used to derive distance estimates/reconstruct the three-dimensional distribution of stars in the Galaxy (which can imply different results even for the same stellar population). According to all the geometric parametrisations tested above, the estimated warp precession is significantly different from zero (thus in disagreement with the static warp model). The final measurement that we report for the warp precession is 10.86 ± 0.03 (stat) ± 3.20 (syst) km s^{-1} kpc^{-1} in the direction of Galactic rotation, about one-third the angular rotation velocity at the Sun's position in the Galaxy. Recently, [19] obtained a consistent value of $13.57^{+0.20}_{-0.18}$ km s^{-1} kpc^{-1} using Starhorse distances [20], supporting the scenario of a significantly prograde warp precession.

Implications

The Galactic disc is a complex structure, whose evolution is driven by several evolutionary processes. Signatures in the structure and kinematics of the Galactic disc can be left by both internal (e.g., secular evolution processes) and external (e.g., interaction with satellite galaxies) mechanisms. In this context, observational constraints play a fundamental role, as they can shed light on the possible scenarios available to date, and help us to better understand the evolutionary history of our own Galaxy. Using N-body simulations of a Milky Way-like galaxy [21], we analysed the response of the Galactic disc to the repeated impacts of a satellite galaxy (whose properties are similar to the Sagittarius dwarf galaxy, commonly considered as one of the major perturbers of the Galactic disc). We find that a significantly prograde warp precession rate is a natural consequence of an interaction with a satellite, giving a possible interpretation to the measurements presented in [10, 19]. On the other hand, in the semi-quiescent phases, the warp precession is close to zero (which, according to the model presented above, would be more consistent with the static case).

The experiment performed with N-body simulations suggests that the warp precession rate can be an important parameter, whose measurement, in the context of a Milky Way-satellite system, has a constraining power on the dynamical state of interaction [22].

Limitations and future prospects

The simple model presented here only represents a first step toward our understanding of the disc's dynamical evolution. For example, it would be interesting to explore more sophisticated models including differential precession and/or additional Fourier vertical distortions (e.g., the azimuthal term $m = 2$). Moreover, future data-sets from the Gaia satellite and other ground-based surveys will presumably shed further light on the warp precession, being based on more precise astrometric measurements, covering larger portions of the Galactic disc, and providing additional information for stellar astrophysical parameters. We are living in the Golden Age of Galactic studies: present and future data-sets, combined with more realistic models, will surely reveal key information on the evolutionary history of the Galactic disc, and the role played by its environment.

References

[1] Kerr F. J. 1957, AJ, 62, 93
[2] Battaner, E., et al. 1990, A&A, 236, 1
[3] Lopez-Corredoira, M., et al. 2002, A&A, 394, 883
[4] Kim, J. H., et al. 2014, ApJ, 789, 90
[5] Sparke, L. S., & Casertano, S. 1988, MNRAS, 234, 873
[6] Gaia Collab., Prusti, T., et al. 2016, A&A, 595, A1
[7] Gaia Collab., Brown, A. G. A., et al. 2016, A&A, 595, A2
[8] Gaia Collab., Brown, A. G. A., et al. 2018, A&A, 616, A1
[9] Gaia Collab., Brown, A. G. A., et al. 2021, A&A, 649, A1
[10] Poggio, E., et al. 2020, Nature Astronomy, 4, 590
[11] Poggio, E., et al. 2018, MNRAS, 481, L21
[12] Lindegren, L., et al. 2018, A&A, 616, A2
[13] Yusifov, I., et al. 2004, in The Magnetized Interstellar Medium (eds Uyaniker, B. et al.), 165
[14] Momany, Y., et al, 2006, A&A, 451, 515
[15] López-Corredoira, M., et al. 2002, A&A, 394, 883
[16] Reylé, C., et al. 2009, A&A, 495, 819
[17] Drimmel, R., et al. 2001, AJ, 556, 181
[18] Chen, X., et al. 2019, Nature Astronomy, 3, 320
[19] Cheng, X., et al. 2020, AJ, 905, 49
[20] Queiroz, A. B. A., et al. 2020, A&A, 638, A76
[21] Laporte, C. F. P., et al. 2018, MNRAS, 481, 286
[22] Poggio, E., et al. 2021, MNRAS, 508, 541

Short CV

2018:   PhD in Physics and Astrophysics, Università degli Studi di Torino, Italy
2018–2020:   Post-doctoral Fellow, Osservatorio Astrofisico di Torino, Italy
2020–present: CNES Post-doctoral Fellow, Observatoire de la Côte d'Azur, France

From quenched to gas-rich to star-forming: the diversity of faint dwarf galaxies

Martin P. Rey

Beecroft fellow, Sub-department of Astrophysics, University of Oxford, United Kingdom

Department of Astronomy and Theoretical Physics, Lund University, Sweden

In the past fifteen years, advances in wide-sky, photometric imaging have more than doubled the number of known, faint dwarf galaxies around the Milky Way (see [1] for a review; Figure 1). Thanks to their low masses and shallow potential wells, these faint systems are highly sensitive probes of the nature of dark matter – for example providing leading constraints on models modifying the abundance of small structures [2] – and of the physics of star formation and how stars "feedback" and affect their surrounding interstellar medium [3, 4, 5].

This new abundance of data, and the prospect of further discoveries and more detailed characterisations with next-generation wide, deep surveys (e.g., LSST, Euclid, the Nancy Roman Space Telescope) provides us with a unique opportunity to drastically improve our understanding of these physical processes. However, interpreting these observations requires accurate theoretical predictions, that pinpoints the properties of a population of faint dwarf galaxies in both its expected mean and scatter. Such requirement implies modelling a large number of objects, to sample many different histories and masses. This is however in direct conflict with the need to accurately resolve internal, astrophysical processes within these small objects. In this Hypatia colloquium, I present work addressing this challenge using a new approach [6, 7], part of the EDGE collaborative effort first introduced in [5].

We start by using high-resolution cosmological, galaxy formation simulations to compute each galaxy's observables. These hydrodynamical simulations are capable of resolving individual supernova explosions, thus significantly reducing uncertainties in the modelling of supernova feedback [5]. We then combine them with the genetic modification approach [8, 9, 10], which allows us to efficiently scan through possible cosmological mass growth histories. Genetic modifications create alternative, cosmological initial conditions for a given galaxy, modifying a specified aspect of its mass growth over time, while recreating the same large-scale structure and environment. Evolving each modified initial condition with our hydrodynamical setup then enables controlled, comparative experiments, building a causal account of how histories shape the dwarf's final observables.

This dual ability is key to our presented results, allowing us to cleanly isolate how (i) different early histories drive scatter in the stellar masses and sizes of field ultra-faints at fixed halo mass today (Section 1 and [6]); and (ii) how different late assemblies allow the re-accretion of gas and the re-ignition of very low-levels of star formation, similar to observed systems like Leo T and Leo P (Section 2 and [7]).
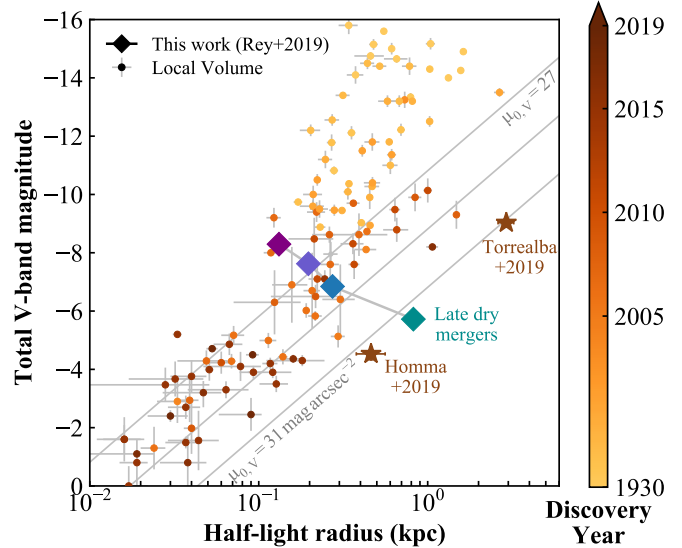

Figure 1: Response of the $z = 0$ total V-band magnitude and half-light radius of an ultra-faint dwarf when modifying its early growth history. Increasingly earlier-forming dwarfs (turquoise to purple) have larger stellar masses (smaller total V-band magnitude) and more compact sizes. Our latest forming history (turquoise) assembles through late, dry mergers, inflating its size and making it more diffuse (grey lines) than currently observed systems (points). Reproduced from Figure 3 in [6].

Generating scatter in stellar masses and surface brightnesses of ultra-faint dwarfs

We start with a series of four "genetically modified" initial conditions for a single object, varying its accretion history up to the time of cosmic reionization, while fixing its $z = 0$ dynamical mass. Figure 1 shows the response of the central galaxy's total V-band magnitude and half-light radius to these modifications.

By making this system systematically earlier forming (from turquoise to purple in Figure 1), we see that the dynamical mass assembled before reionization directly maps onto the final stellar mass of an ultra-faint. Earlier-forming galaxies begin forming stars when the universe was younger, and have a more vigorous star formation rate at a given time. They therefore assemble systematically higher stellar masses (smaller total magnitude), before further gas accretion is hampered by the build-up of cosmic photo-ionizing radiation as the Universe is reionized, leading to their permanent quenching [11]. Since by construction, all our histories converge to the same dynamical mass today, we cleanly show how the diversity of possible early histories leads to an extended scatter (1 dex) in the relation between stellar mass and halo mass of ultra-faints at $z = 0$.

Furthermore, our scan through histories reveals a highly diffuse dwarf (turquoise), arising from an early truncation of in-situ star formation due to reionization, but a later growth by dry mergers. These mergers deposit stars on wide orbits, vastly growing the final half-light radius. Such extremely diffuse systems lack counterparts in currently observed systems (points), but the recurring improvement toward lower surface brightnesses (grey lines; observations coloured by discovery year) should enable near-future surveys to test their existence.

Re-igniting star formation in faint dwarf galaxies

Extending from the previous results, we then focus on a suite of four faint dwarf galaxies hosted in dark matter halos with mildly increasing mass at $z = 0$ ($1.5 \times 10^9 \leq M_{200} \leq 3 \times 10^9\,M_\odot$). All dwarf galaxies in our suite are still sufficiently small to be quenched by the reduction of gas inflows once cosmic reionization has heated their surrounding medium (Figure 2).

However, the two more massive objects both experience a re-ignition of star formation after $z = 1$. We link this rejuvenation to a slow re-accretion of gas after reionization ($z \leq 2$), steadily increasing the central gas mass of the dwarf until star-forming densities are eventually reached (Figure 2, blue). This re-accretion is triggered by a late growth in dynamical mass, which allows leftover gas within the halo to reach sufficient densities to cool and condense efficiently.

However, because of the low gas masses within these dwarfs, we find that small energy inputs from old stars (Type Ia explosions and winds from AGB stars) can balance the cooling of gas and lengthen the quiescent period by several billion years (brown). Furthermore, we show that this feedback barrier strongly interacts with the given assembly of the dwarf. We, for example, achieve to restart star formation in a quiescent object by either reducing feedback strength or growing its final dynamical mass using genetic modifications.

Neutral gas in faint dwarfs

We have shown examples of (i) gas-rich, low-mass dwarfs with ongoing star formation (e.g., blue in Figure 2), (ii) low-mass dwarfs caught in transition, exhibiting an exclusively old stellar population but a sizeable gas content (e.g., brown in Figure 2), and (iii) gas-poor, quenched low-mass dwarfs (e.g., black in Figure 2). All three galaxies have stellar and dark matter halo masses within a factor of two, demonstrating extended scatter in gas content and stellar ages within low-mass dwarfs due to the coupling between feedback and late assemblies.

This uncovered diversity strongly motivates a quantification of the neutral gas observables across our simulated suite of dwarf galaxies. In fact, matching radio observations with deep imaging has already provided evidence for both star-forming and non-star-forming, gas-rich faint dwarfs [12, 13]. The prospect of combining ever-deeper photometric facilities with next-generation radio facilities (e.g., SKA) further warrants investigating the relationship between stellar and HI content at the faint end. Presenting preliminary results, I showed how the diversity of histories and final masses in our suite leads to order-of-magnitude scatter in neutral gas content at fixed stellar mass today.
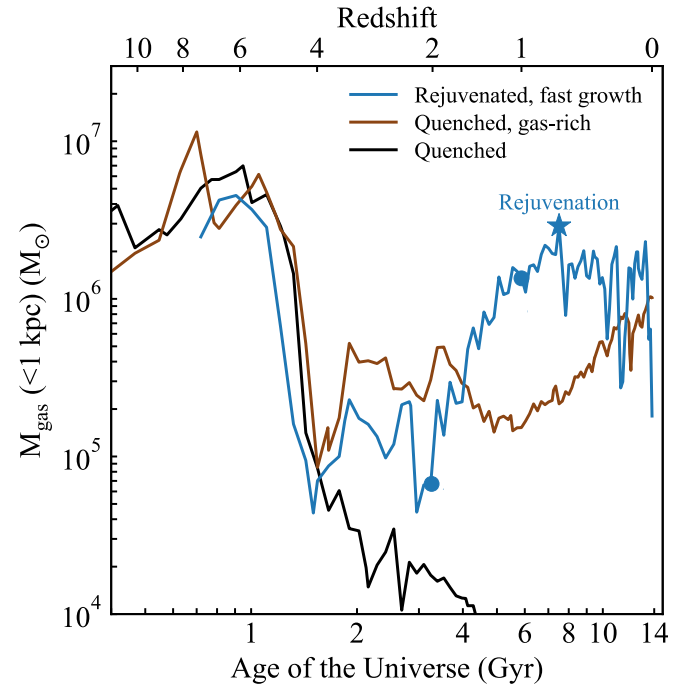
Figure 2: Evolution of the central gas mass for three simulated dwarfs with increasing halo mass today (black to brown to blue). All dwarfs see their gas inflows heavily reduced following reionization ($z \approx 4$), but a late growth in dynamical mass triggers slow re-accretion of gas (blue and brown). If rapid enough, this accretion allows the re-ignition of star formation before $z = 0$ (blue, but not brown). Reproduced from Figure 2 in [7].

References
[1] Simon, J. 2019, ARAA, 57, 375
[2] Nadler, E., et al. 2020, ApJ, 893, 48
[3] Munshi, F.. et al. 2019, ApJ, 874, 40
[4] Smith, M., et al. 2020, MNRAS, 506, 3882
[5] Agertz, O., et al. 2020, MNRAS, 491, 1656
[6] Rey, M., et al. 2019, ApJl, 886, L3
[7] Rey, M., et al. 2020, MNRAS, 497, 1508
[8] Roth, N., et al. 2016, MNRAS, 455, 974
[9] Rey, M., & Pontzen, A. 2018, MNRAS, 474, 45
[10] Stopyra, S., et al. 2020, ApJS, 252, 28
[11] Efstathiou, G. 1992, MNRAS, 256, 43
[12] McQuinn, K., et al. 2015, ApJ, 812, 158
[13] Janesh, W. 2019, AJ, 157, 183

Short CV

2014–2015:   Master in Physics, Imperial College London, United Kingdom
2015–2016:   Master in Aerospace Engineering, ISAE Supaéro, France
2016–2019:   PhD in Astronomy, University College London, United Kingdom
2019–2021:   Postdoctoral Fellow, Lund University, Sweden
2021–present: Beecroft Fellow in Cosmology, Oxford, United Kingdom

Expanding the supermassive black hole scaling relations with dynamical modelling

Sabine Thater[‡‡]

University of Vienna, Türkenschanzstrasse 17, 1180 Wien, Austria

Massive black holes (MBH) reside in the centers of most galaxies. While MBH are invisible, their masses (M_{BH}) can be estimated by dynamically tracing their gravitational potential (e.g., with stars or gas). Tight scaling relations between such derived M_{BH} and different properties of their host galaxies suggest that they have grown in tandem with each other [1]. To understand this co-evolution between MBH and their host galaxies, it is crucial to populate the scaling relations with precise and accurate measurements. Until now, robust M_{BH} have been determined dynamically for about 150 galaxies. However, this sample is highly heterogeneous as M_{BH} from different methods, different dynamical tracers and different instruments are compiled together (see Figure 1 in [2]). The different methods are limited and can often only be applied for certain galaxy types. Therefore, detailed cross-checks are valuable and will help to understand the intrinsic scatter in the scaling relations.
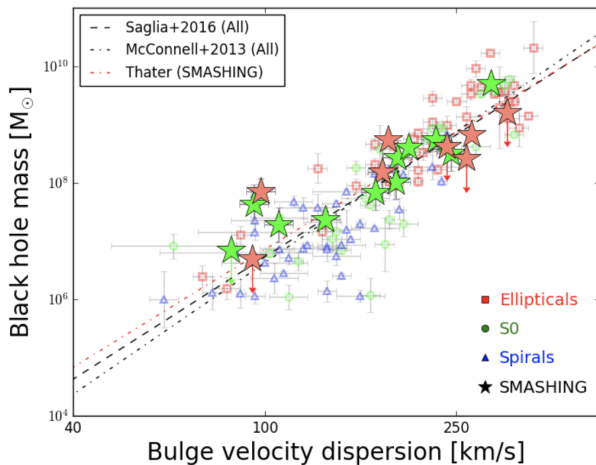
and obtained robust and homogeneously measured M_{BH} spread from the low- to the high-mass end (see Figure 1).

Our SMASHING sample greatly complements the literature sample as we not only add 19 new measurements but can also analyse a very homogeneously measured M_{BH} sample. While most of our measurements are within the scatter of the scaling relations, two low-mass galaxies show unusually over-massive black holes. The galaxies at the lower mass-end also indicate that generally more massive MBHs reside in early-type galaxies (ETG) than in late-type galaxies (LTG) for constant velocity dispersion. When fitting only the SMASHING sample, the scaling relation becomes slightly shallower but is consistent with scaling relations from the literature. This suggests that the shape of the scaling relation is not strongly influenced by the intrinsic scatter of the M_{BH} sample.

Figure 1: Black hole scaling relation over-plotted with our SMASHING galaxies (stars). Literature M_{BH} were taken from [3]. Fitting only SMASHING galaxies, the relation becomes shallower.
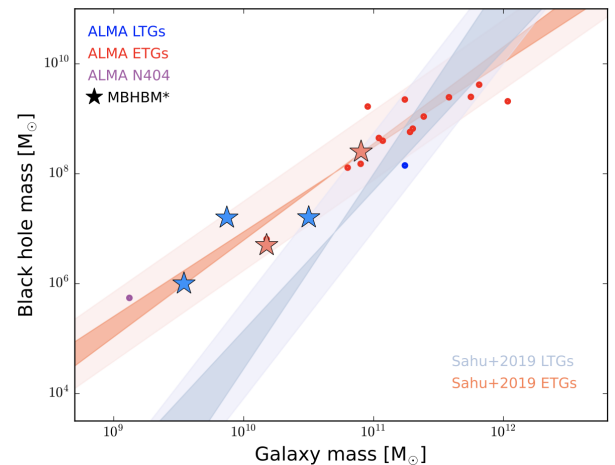
Figure 2: Black hole scaling relations for LTGs and ETGs based on stellar and (non-ALMA) gas measurements. Overplotted are the ALMA molecular gas-based M_{BH} from the literature (dots) and our MBHBM* (stars).

Stellar kinematics

About 40 per cent of robust M_{BH} have been estimated from stellar dynamics. However, even when only using stars as kinematic tracers, the results of different measurement methods can differ significantly. In the SMASHING project, we made use of high-resolution adaptive-optics assisted SINFONI and NIFS observations to derive M_{BH} for 18 early-type galaxies and one late-type galaxy [4, 5, 6, 7]. We created both dynamical Jeans and Schwarzschild models for all SMASHING galaxies

Molecular gas kinematics

About one quarter of ETGs harbour compact molecular gas disks in their centers [8]. These disks often reach within the MBH sphere-of-influence and undergo acceleration by the gravitational potential. Utilizing high-resolution ALMA observations it is possible to measure this central rise in velocity. With the "Measuring BHs below the Milky-Way-mass galaxies" (MBHBM*, PI: D.D. Nguyen), we use the kinematic information of these molecular gas disks and derive robust M_{BH} for low-mass galaxies. So far, we have finished the analysis for 5 targets [9, 10, 11, 12], another 15 targets are planned to be observed. Since 2013, 20 M_{BH} have been measured with this method by different teams. In Figure 2, we com-

---

[‡‡]In collaboration with Davor Krajnović, Dieu D. Nguyen, Shelley-Anne D. Harrisberg

pare the measurements using molecular gas kinematics with measurements from other tracers, to check if there are systematic differences between those M_{BH} samples.

The measurements from molecular gas kinematics are shown as points or stars (our measurements) and are color-coded by the morphology of the host galaxy. The shaded regions show the scaling relations derived for M_{BH} measured from other tracers for ETGs and LTGs from [13]. It is immediately visible that the main trend of the ETG scaling relations for ALMA molecular gas-based M_{BH} and other measurements are consistent. ALMA LTG on the other hand show a different picture. There have been only four measurements so far, but they seem to be significantly offset to the measurements from other kinematic tracers.

Direct cross-checks between the different tracers

Finding galaxies for which multiple methods can be applied and cross-compared is very difficult. An early-type galaxy harbouring a molecular gas disk is a prime target for such a study. We obtained adaptive-optics assisted MUSE and ALMA observations and derived the black hole mass in the early-type galaxy NGC 6958 using stars and molecular gas as kinematic tracers. Our dynamical models inferred $3.6 \times 10^8 M_\odot$ and $4.5 \times 10^8 M_\odot$ from stellar kinematics and molecular gas, respectively [14]. While this cross-check for NGC6958 shows a good consistency between the results of the two methods, that is not the case for other galaxies (Figure 3). Very often the gas measurement is about a factor of 2 smaller than the stellar-based measurement. The difference seems to become more significant for black holes more massive than $5 \times 10^8 M_\odot$. The most famous example is the case of M87. For M87, stellar- and gas-based methods returned a discrepancy of a factor 2 in black hole mass [15]. New constraints could be given by the Event Horizon Telescope measurement [16] which supported the more massive stellar-based MBH for M87. Additional cross-checks are needed in the future to understand the systematic differences between the measurement methods and decrease the intrinsic scatter of the scaling relations.

Conclusion

Testing the robustness of M_{BH} estimates is crucial to better understand the scaling relations. A first consistency check reveals that within a factor of 2-3, most methods give consistent results. However, to decrease this factor, one needs to take special care of the systematics of dynamical modeling methods. We have also added 25 masses to the scaling relations ranging from the low- to the high-mass range. Our measurements are generally consistent with the scaling relations, which shows

that the in-homogeneity in M_{BH} is likely not a significant problem for the overall trend. We also find over-massive outliers from the relations which might indicate more violent merger histories for those galaxies. In the future, the analysis of the galaxy orbital distribution will provide further implications about the formation and growth of the MBHs. Furthermore, additional measurements for low-mass galaxies are needed in the future to confirm our conclusions.
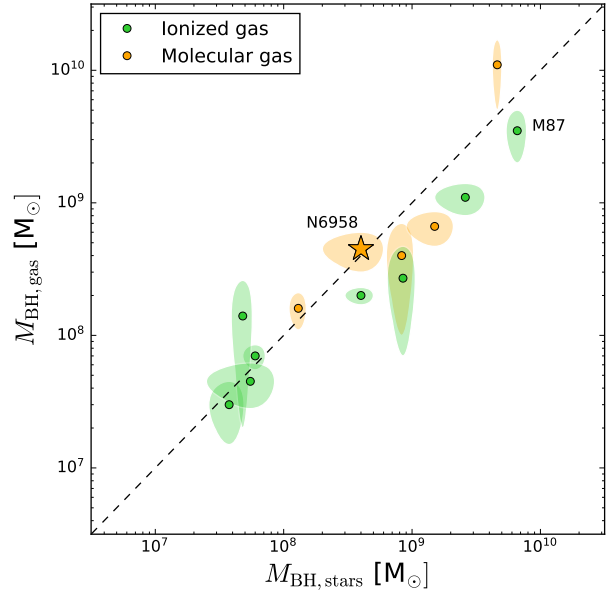
Figure 3: Cross-check between stellar- and gas-based M_{BH} for ionized gas molecular gas. Our measurement is indicated as star. The dashed line is the one-to-one line where the measurements should ideally be located.

References
[1] Kormendy, J., & Ho, L. C., 2013, ARA&A, 51, 511
[2] van den Bosch, R. C. E. 2016, ApJ, 831, 134
[3] Saglia, R. P., et al. 2016, ApJ, 818, 47
[4] Thater, S., et al. 2017, A&A, 597, A18
[5] Krajnović, D., et al. 2018, MNRAS, 477, 3030
[6] Thater, S., et al. 2019, A&A, 625, A62
[7] Thater, S., et al. 2021, in prep.
[8] Davis, T. A., et al. 2014 MNRAS, 443, 1
[9] Nguyen, D. D., et al. 2020 ApJ, 892, 68
[10] Nguyen, D. D., et al. 2021 MNRAS, 504, 3
[11] Nguyen, D. D., et al. 2021, subm.
[12] Nguyen, D. D., et al. 2021, in prep.
[13] Sahu, N., et al. 2019, ApJ, 887, 10
[14] Thater, S., et al. 2021, subm.
[15] Walsh, J., et al. 2013, ApJ, 770, 86
[16] Event Horizon Telescope Collaboration 2019, ApJ, 875, L6

Short CV

2014: Diploma in Physics, University of Potsdam, Germany
2019: PhD in Astronomy, University of Potsdam, Germany
2019: Postdoctoral Researcher in Astronomy, University of Vienna, Austria

53

Galaxy evolution in dense environments: a study of the cold ISM in the Fornax cluster

Nikki Zabel

Kapteyn Astronomical Institute, University of Groningen, The Netherlands

Often galaxies do not live alone, but in groups or clusters that can harbour up to thousands of galaxies, bound together by a dark matter halo. Galaxies residing in clusters are surrounded by an extremely hot plasma ($T \approx 10^8$ K, e.g., [1]): the "intracluster medium" (ICM). Their relative velocities are high (velocity dispersions are typically several hundreds of km s^{-1}). This means that galaxy clusters are turbulent environments, not unlike swarms of moths attracted to a light source (in this case the brightest cluster galaxy; BCG). As a result, the evolution of cluster galaxies is more complicated than that of their more isolated counterparts. Galaxy clusters harbour a relatively high fraction of elliptical galaxies, suggesting that the star formation (SF) in cluster galaxies is quenched more rapidly than in similar systems in the field (e.g., [2]).

There are various environmental mechanisms that can affect the evolution of cluster galaxies. For example, ram pressure stripping (RPS, [3]) is the "headwind" a galaxy experiences as it moves through the ICM. The ICM can also prevent accretion of fresh gas onto galaxies (e.g. by removing the circum-galactic medium). This is referred to as strangulation/starvation [4]. While field galaxies often merge when they encounter each other, the high velocity dispersion in clusters ensures that most encounters result in relatively brief and violent interactions instead [5]. Even in the absence of violent encounters, the proximity of peers can result in tidal interactions. Both types of interactions can have a severe impact on galaxies' stellar distributions and interstellar media (ISM).

Exactly how these processes result in the premature quenching of star formation in cluster galaxies is not yet well understood. They are often studied through galaxies' HI discs, which are very suitable for this because of their wide extent, making them susceptible to environmental effects. However, it is the molecular gas that is the direct fuel for star formation, occupying an important step between the atomic gas phase and actual star formation. If we aim to understand environmental quenching in more detail, it is crucial to study how environmental processes affect the more tightly bound and centrally located molecular gas in cluster galaxies.

The molecular gas content of Fornax cluster galaxies

To this end, we have studied the molecular gas reservoirs of all 30 galaxies in the Fornax cluster that were detected in HI (with the Australia Telescope Compact Array, [6]) or the far infrared (with the *Herschel* Space Telescope, [7]). The Fornax cluster is the smaller but equally nearby sibling of the Virgo cluster ($M = 7 \times 10^{13}$ M$_\odot$, [8] and $D = 19.95$ Mpc, [9]). The ^{12}CO(1-0) line in these galaxies was observed and mapped using the Atacama Millimetre/submillimetre Array [10]. We detected CO in 15/30

galaxies. In 8/15 of these galaxies, the molecular gas is morphologically and kinematically disturbed. Examples of galaxies with regular and disturbed CO emission are shown in figure 3 and 4 of [10], respectively.

In Figure 1, molecular gas fractions of galaxies in the Fornax cluster are compared to a field sample from the Extended CO Legacy Database for GASS (xCOLD GASS, [14]). Fornax galaxies, especially those with disturbed/asymmetric molecular gas reservoirs, are molecular gas deficient compared to xCOLD GASS galaxies. Since the molecular gas discs of Fornax galaxies are also disturbed and/or truncated compared to those of field galaxies, this is likely the result of the environment.
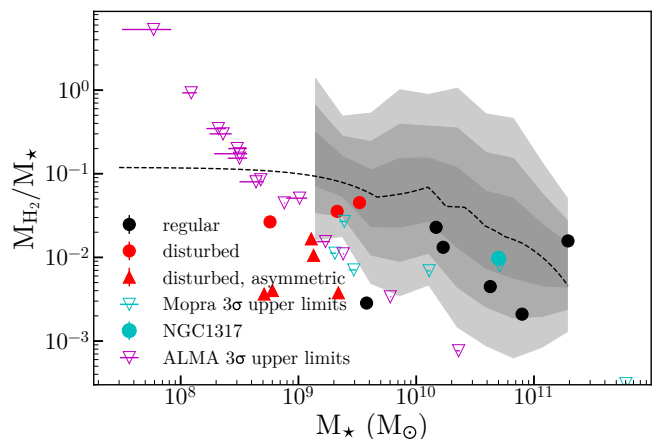

Figure 1: Molecular gas fractions as a function of stellar mass. Black dots represent Fornax galaxies with regular molecular gas reservoirs, whereas red markers indicate galaxies with disturbed molecular gas reservoirs. Triangular markers indicate asymmetric CO emission. Upper limits are shown as magenta open triangles. Within the shaded area, the dashed line represents the median molecular gas fraction from xCOLD GASS. The three shades of grey indicate the 1, 2, and 3 σ levels (from dark to light) of that sample. Outside the shaded area the dashed line is based on linear extrapolation (in log space). Fornax galaxies have systematically lower H$_2$ fractions than xCOLD GASS galaxies, especially the galaxies with disturbed/asymmetric H$_2$ reservoirs. This figure includes H$_2$ fractions from additional data taken with Mopra, shown in cyan. This Figure is an adaptation of Fig. 8 in [10].

The star formation relation in the Fornax cluster

For 9 of the 15 CO detected Fornax galaxies, Hα maps from the Multi Unit Spectroscopic Explorer (MUSE) are available from the Fornax3D project [15], allowing us to calculate the resolved star formation relation (Σ_{H_2} vs. Σ_{SFR}, where Σ_{SFR} is estimated from the Hα emission). This will reveal whether the depletion times of (disturbed) molecular gas reservoirs in Fornax galaxies are affected by environmental processes, or if star formation is (still) as efficient as in field galaxies.
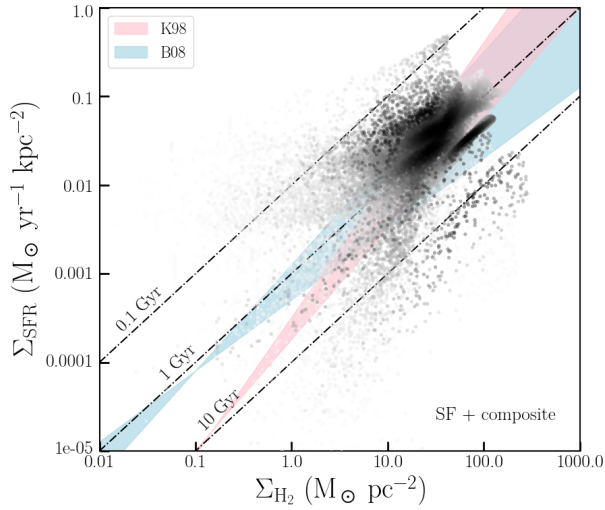
Figure 2: Star formation relation of Fornax cluster galaxies that were detected in both CO and Hα. The shades of the markers indicate their local densities, determined using Gaussian kernel density estimation (KDE). The dash-dotted lines are lines of constant depletion time. For comparison, the K98 and B08 relations are shown in pink and blue, respectively. Fornax galaxies have normal to short depletion times compared to the K98 and B08 relations. This Figure is an adaptation of Fig. 3 in [12].

The resolved star formation relation of these Fornax galaxies is shown in Figure 2. Here we can see that depletion times of Fornax galaxies ($\Sigma_{H_2}/\Sigma_{SFR}$) are comparable to or slightly shorter than star formation relations from the literature (K98 [16], pink, and B08 [17], blue). This means that the molecular gas in Fornax galaxies is still forming stars at least as efficiently as field galaxies, despite (or perhaps because of) the observed disturbances and deficiencies. The slightly decreased depletion times could be a result of the galaxies experiencing slight starbursts as they enter the cluster.

Molecular gas-to-dust ratios in the Fornax cluster

Dust plays an important role in the star formation process: it catalyses the formation of H_2, and shields it from radiation. Because dust and molecular gas are linked, we might expect them to be removed from cluster galaxies simultaneously. This has previously been observed in the Virgo cluster [19, 20]. Here we study H_2-to-dust ratios in the Fornax cluster to investigate whether this is also the case in Fornax.

Dust masses were obtained from SED fits to *Herschel* data from DustPedia (DP, [18]). In Figure 3, H_2-to-dust ratios are shown as a function of stellar mass, and compared to a field sample and a Virgo cluster sample from DP. Compared to field galaxies, Fornax galaxies have suppressed H_2-to-dust ratios at fixed stellar mass, whereas those of Virgo galaxies are enhanced. Possible explanations for this include the more efficient stripping
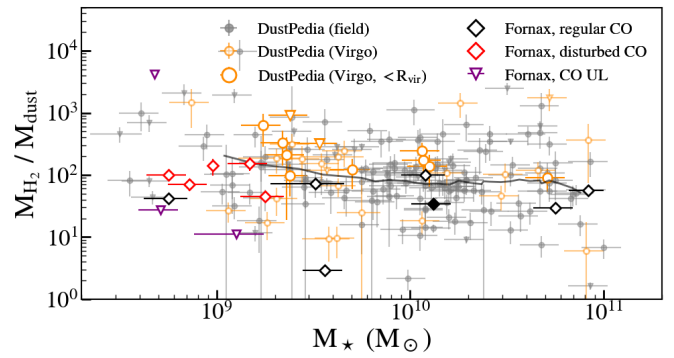

Figure 3: Molecular gas-to-dust ratios of Fornax galaxies compared to the DP sample. DP field galaxies are shown in grey, and DP Virgo galaxies in orange. DP Virgo galaxies inside the virial radius are indicated with larger markers. The median of the DP field sample is indicated with a solid grey line. Markers are similar to those in Figure 1, and explained in the legend. Fornax galaxies have systematically suppressed molecular gas-to-dust ratios, whereas those of Virgo galaxies are systematically increased compared to the DP field sample. This Figure is an adaptation of Fig. 3 in [13].

of H_2 compared to dust, and the more efficient enrichment of dust in the star formation process compared to H_2 in the Fornax cluster.

Fornax cluster galaxies detected in CO are systematically H_2 deficient compared to field galaxies at fixed stellar mass, and half of them have disturbed H_2 reservoirs. However, this gas is still forming stars at least as efficiently as field galaxies. H_2-to-dust ratios are suppressed, suggesting that either molecular gas is affected more strongly by environmental effects than dust, or that dust is replenished more efficiently in the SF cycle.

References

[1] Takisawa, M., et al. 1998, ApJ, 509, 579
[2] Dressler, A. 1980, ApJ, 236, 351
[3] Gunn, J. E., & Gott, III, J. R. 1972, ApJ, 176, 1
[4] Larson, R. B, et al. 1980, ApJ, 237, 692
[5] Moore, B., et al. 1996, Nature, 379, 613
[6] Loni, A., et al. 2021, A&A, 648, 18
[7] Davies, J. I., et al. 2013, MNRAS, 428, 834
[8] Drinkwater, M. J., et al. 2001, ApJ, 548, L139
[9] Tonry, J. L., et al. 2001, ApJ, 546, 681
[10] Zabel, N., et al. 2019, MNRAS, 483, 2251
[11] Peletier, R., et al. 2020, eprint arXiv:2008.12633
[12] Zabel, N., et al. 2020, MNRAS, 496, 2155
[13] Zabel, N., et al. 2021, MNRAS, 502, 4723
[14] Saintonge, A., et al. 2017, ApJS, 233, 20
[15] Sarzi, M., et al. 2018, A&A, 616, 23
[16] Kennicutt, Jr., R. C. 1998, ApJ, 498, 541
[17] Bigiel, F., et al. 2008, ApJ, 136, 2846
[18] Davies, J. I., et al. 2017, PASP, 129, 044102
[19] Cortese, L., et al. 2010, A&A, 518, L49
[20] Pappalardo, C., et al. 2012, A&A, 545, A75

Short CV
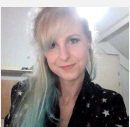
2016: Master of Science "Research in Astronomy", Leiden University, The Netherlands
2021: PhD in Astronomy, Cardiff University, UK
Present: Postdoctoral Researcher, University of Groningen, The Netherlands

Constraining dark matter with ultra-faint dwarf galaxies

Sebastiaan L. Zoutendijk

Leiden Observatory, Leiden University, P.O. Box 9513, 2300 RA Leiden, The Netherlands

Constraining the nature and properties of dark matter is a long-running, but important effort. In the ΛCDM paradigm, dark matter is the dominant component at the scale of galaxies and for a large part of cosmic history was also the dominant component for the entire Universe. Understanding dark matter is therefore very important to understand the evolution of galaxies and of the Universe as a whole. Understanding what dark matter is also has the potential to revolutionize physics. If dark matter is found to be a new, yet unknown particle, we have proof of physics beyond the Standard Model. Conversely, if dark matter is found to be the apparent effect of a modification to the theory of gravity, we will have to revise a fundamental law of physics. Furthermore, the nature and history of the Universe are profound questions of science with philosophical value.

Different theories of dark matter predict different dark-matter density profiles. However, baryonic feedback can alter those profiles, either contracting the profile or forming a core, obscuring the original profile and its dark-matter physics along with it. Additionally, baryonic processes can create spectral features that obscure possible spectral signatures of dark matter. Ultra-faint dwarf galaxies (UFDs) are the most dark-matter dominated galaxies known and are expected to host so few baryons that their density profiles remain pristine (for a review, see [1]). For this reason UFDs are one of the best classes of objects for the constraining of the nature and properties of dark matter.

In this contribution, I will discuss constraints on a few different types of dark matter, which can phenomenologically be broadly divided into three categories. In cold dark matter (CDM), gravity is the only significant interaction between a dark-matter particle and any other particle and the density profile will be the cuspy Navarro–Frenk–White (NFW) profile in the absence of baryons. This kind of dark matter includes both proposed elementary particles, such as the axion or axion-like particles (ALPs), and massive compact halo objects (MACHOs), such as primordial black holes. If there is a significant interaction between dark-matter particles, then we are in the territory of self-interacting dark matter (SIDM). Different kinds of self-interaction have been proposed, including scattering and annihilation. These interactions result in a cored profile. Lastly, in fuzzy dark matter (FDM), the dark-matter particles are ultra-light bosons (which could be, but not necessarily are, ultra-light ALPs) with de Broglie wavelengths of astronomical sizes. This causes an alteration of the density profile by large-scale quantum-mechanical effects and might explain the cores of classical dwarf galaxies if the boson mass is $\sim 10^{-22} \, \mathrm{eV} \, c^{-2}$.

Several constraints on dark matter from UFDs are already available in the literature. Examples include the following: the mass and abundance of MACHOs has been constrained by the survival of the star cluster in the UFD Eridanus 2 (Eri 2) and by the stellar distribution of the UFD Segue 1, because the disruptive effects of mass segregation between MACHOs and stars are not observed [2, 3]. Also in Eri 2, the mass and abundance of FDM is constrained in a similar way as those of MACHOs, because the quantum-mechanical density fluctuations would also destroy the cluster [4, 5]. Another example is the non-detection of γ-ray signatures from Segue 1 and other dwarf galaxies; this absence constrains the cross section of dark-matter annihilation [6].

Here, I report on results obtained from MUSE-Faint [7], a survey of UFDs with MUSE. Because MUSE is an integral-field spectrograph, it is possible to measure velocities from stellar spectra in the centres of these very dense stellar systems, which would not be possible with fibre spectrographs. Additionally, the field of view of MUSE is large enough to cover the half-light radii of most UFDs with one or a few pointings. Over the entire 100-hour guaranteed-time survey, MUSE-Faint will collect data for ten UFDs, UFD candidates, and other faint dwarf galaxies, with a range of half-light radii and absolute magnitudes. The results presented here are based on the completed observations of Eri 2 and Leo T, both having ~ 100 member stars after combining the MUSE-Faint velocities [8; Vaz et al. in prep.] with literature data [9, 10] from larger radii.

Results

The literature constraints [2] on MACHOs based on the cluster of Eri 2 are based on the assumption that this cluster is at the centre of that UFD. At the time, no spectroscopy of cluster stars was available, therefore it was not known whether the cluster was associated with Eri 2 or merely seen in projection. The first results [7] of MUSE-Faint showed that the systemic velocity of the cluster and the bulk of Eri 2 are very similar, $79.7^{+3.1}_{-3.8} \, \mathrm{km \, s^{-1}}$ and $76.0^{+3.2}_{-3.7} \, \mathrm{km \, s^{-1}}$, respectively. This is consistent with an association between the two. With the new velocities of cluster members and stars in the centre of Eri 2, we could update the MACHO constraints on mass and abundance. If one assumes MACHOs constitute all dark matter, we find MACHOs must be less massive than $44 \, M_\odot$ (95% confidence level).

Observations of Leo T from MUSE-Faint have been used in a study [11] to constrain the properties of ALPs decaying into photons. Such a process would create an emission line coming from the dark-matter halo. The strength and wavelength of the line are related to the coupling strength and the ALP mass. Finding no detection, we placed an upper limit to the coupling strength of a few times $10^{-13} \, \mathrm{GeV^{-1}}$ (95% confidence level) for masses

that produce an emission line visible with MUSE, ~ 2.5–$5.5\,\mathrm{eV}\,c^{-2}$. This constraint is over two orders of magnitude stronger than previous results [12, 13] for this mass range. I note that this is a very different mass regime than that of ultra-light ALPs in FDM.

Finally, through a Jeans analysis, the stellar velocities can constrain the dark-matter density profiles of UFDs. By fitting and comparing different profile models, we can constrain dark-matter properties and compare different dark-matter theories. In Figure 1, I show the result of this analysis [8] for Eri 2, with models for CDM, annihilating SIDM, and FDM. The overall agreement between the models is good, though in the centre, where data are sparse, the models start to diverge. The models can be compared using Bayesian evidence, which favours FDM the most and SIDM the least. The difference in evidence between FDM and SIDM is substantial, but not significant, therefore none of the models can be ruled out.
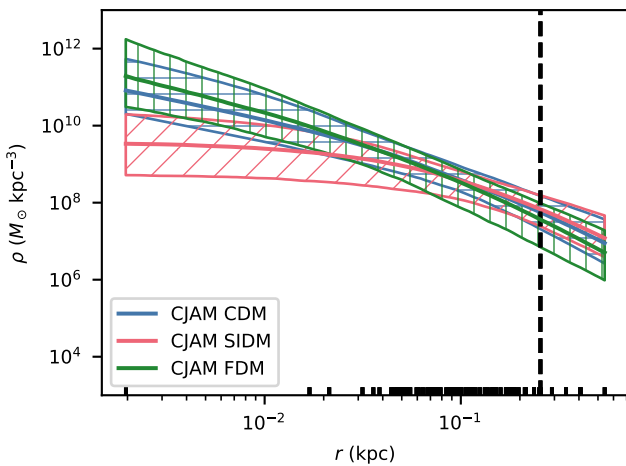

Figure 1: Recovered dark-matter density profiles of Eridanus 2. Displayed are the median density and its 68% confidence interval as a function of radius from the centre. The projected half-light radius is indicated with the vertical dashed line and the projected locations of the stars used to trace the dark matter are indicated with markers along the bottom axis. Reproduced from [8].

From the shape of the SIDM and FDM models we can also derive constraints on dark-matter properties. Annihilating SIDM lowers the density in the centre of the profile, where interactions are the most frequent, thus creating a core of constant density. In FDM, the quantum-mechanical behaviour of the dark matter results in a quantum pressure that prevents a gravitational collapse into a cusp. This creates a core in the very centre, but at intermediate radii the density increases steeply. The altered part of the profile is known as the soliton.

For the SIDM model we do not detect a core [8], but there is a limit to the scales we can probe. The upper limit to the core radius corresponds to an interaction rate that translates into a cross section per unit mass of $\sim 10^{-36}\,\mathrm{cm}^2\,\mathrm{eV}^{-1}\,c^2$ (95% confidence level). This is not as strong as the γ-ray results of [6], but our constraint has the benefit of being valid for all dark-matter particle masses and all annihilation products.

Similarly, we can place an upper limit to the soliton radius, which corresponds to a lower limit of $10^{-20.40}\,\mathrm{eV}\,c^{-2}$ (95% confidence level) on the mass of the ultra-light boson [8]. This is inconsistent with the $\sim 10^{-22}\,\mathrm{eV}\,c^{-2}$ required to explain the cores in more massive dwarf galaxies (e.g., [14, 15]). This discrepancy is problematic for FDM, because the boson mass should be the same in every galaxy. One possibility is that, although an FDM profile can fit these dwarf galaxies, FDM is not the cause of their cores, but rather baryonic processes. These would be almost absent in UFDs, resulting in the non-detection of cores.

Outlook

The three MUSE-Faint studies I have presented here were each based on a single galaxy, with only two different galaxies in total. The strength of the results can be improved by analysing the full MUSE-Faint sample that will span ten galaxies once completed. The larger sample would add robustness due to being less sensitive to possible anomalous galaxies in the sample, and will also enable the improvement of the constraints though a joint analysis. It may also be possible to observe trends in galaxy or halo properties over the range of half-light radii and absolute magnitudes.

References

[1] Bullock, J. S., & Boylan-Kolchin, M. 2017, ARA&A, 55, 343
[2] Brandt, T. D. 2016, ApJ, 824, L31
[3] Koushiappas, S. M., & Loeb, A. 2017, Phys. Rev. Lett., 119, 041102
[4] Marsh, D. J. E., & Niemeyer, J. C. 2019, Phys. Rev. Lett., 123, 051103
[5] El-Zant, A. A., et al. 2020, MNRAS, 492, 877
[6] MAGIC collaboration (Ahnen, M. L., et al.) 2016, JCAP, 02, 039
[7] Zoutendijk, S. L., et al. 2020, A&A, 635, A107
[8] Zoutendijk, S. L., et al. 2021, A&A, 651, A80
[9] Li, T. S., et al. 2017, ApJ, 838, 8
[10] Simon, J. D., & Geha, M. 2007, ApJ, 670, 313
[11] Regis, M., et al. 2021, Phys. Lett. B, 814, 136075
[12] Grin, D., et al. 2007, Phys. Rev. D, 75, 105018
[13] Ayala, A., et al. 2014, Phys. Rev. Lett., 113, 191302
[14] Chen, S.-R., et al. 2017, MNRAS, 468, 1338
[15] Broadhurst, T., et al. 2020, Phys. Rev. D, 101, 083012

Short CV

2015: Bachelor of Science in Physics and in Astronomy, Leiden University, NL
2017: Master of Science in Astronomy (Cosmology), Leiden University, NL
2017–present: PhD candidate, Leiden Observatory, Leiden University, NL

INTERSTELLAR MEDIUM, STAR FORMATION, PLANETARY SYSTEMS

Under pressure: observational determination of the pressures in HII regions across the Galactic centre and nearby galaxies

Ashley. T. Barnes

Argelander-Institut für Astronomie, Universität Bonn, Auf dem Hügel 71, 53121, Bonn, Germany

Young (pre-SNe) stellar feedback

High-mass stars are fundamentally important for driving the evolution of galaxies across cosmic time, due to the large amount of energy and momentum – stellar feedback – that they inject into the interstellar medium (ISM) during their relatively short lifetimes. This is crucial, as in the absence of any stellar feedback, the ISM would rapidly cool and form stars at a high efficiency, consuming most of the available gas in the galaxy on a short timescale incompatible with observations (see, e.g., [1, 2, 3, 4] for key open questions relating to massive star formation). Recent simulations and observational evidence suggest that feedback in the early (pre-supernova) stages of high-mass stars plays a critical role in destroying molecular clouds, and hence producing the low star formation efficiencies inferred for giant molecular clouds (GMCs) in the Milky Way and many other nearby galaxies [5]. Moreover, it appears the stellar feedback may be a fundamental regulator in the mass and energy cycles within galactic nuclei; including the Milky Way [6].

Much progress has been made by studying stellar feedback within regions that are observationally accessible in the local Universe, which are characterised by relatively low gas pressures ($P/k \sim 10^{4-5}$ K cm^{-3}). Studies including a larger dynamical range in external pressures are, however, currently lacking within the literature. These are particularly important towards highly pressured environments, where the ambient gas pressure plays a major role in the molecular cloud life-cycle – setting the initial conditions for star formation, the subsequent star formation efficiency, and the impact of stellar feedback. In addition, such studies have significant implications for high-z star formation, as the ISM pressures observed at the peak of the cosmic star formation history are several orders of magnitude higher than those observed in disc galaxies today. I discuss the fundamental question of how the physics of star formation and feedback vary across environments.

Observationally quantifying stellar feedback

To quantify the relative importance of young (pre-SNe) stellar feedback, we place observational constraints on the main internal feedback mechanisms driving the expansion of a large sample of HII regions. In [4, 7, 8], we consider the following pressure terms thermal gas pressure (P_{therm}), direct (and trapped) radiation pressure (P_{rad}), wind (or shocked gas) pressure (P_{wind}). We compare the total internal pressure, $P_{\mathrm{tot}} = P_{\mathrm{therm}} + P_{\mathrm{rad}} + P_{\mathrm{wind}}$, to the confining pressure of their host environments (P_{de}).
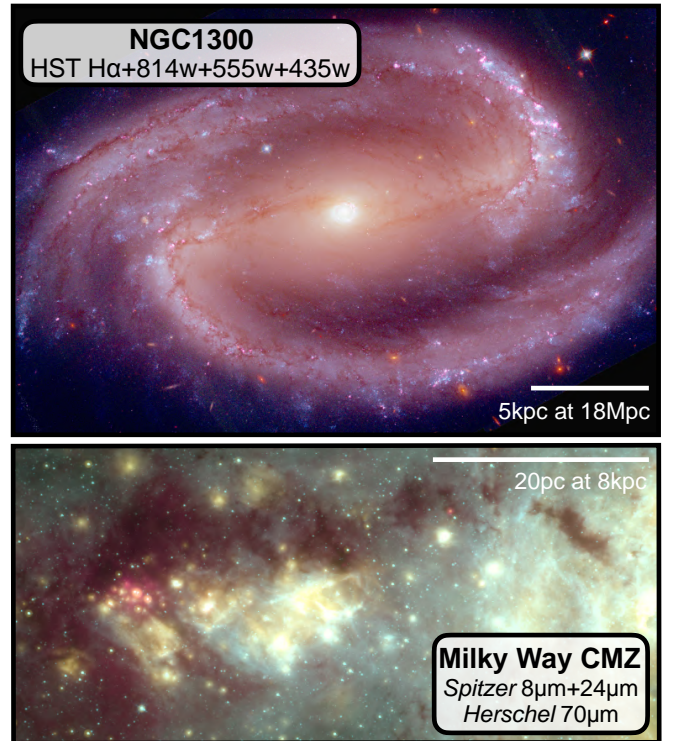

Figure 1: An example of a nearby disc galaxy and the Milky Way Central Molecular Zone (CMZ), which were used to study the effects of stellar feedback, and variations as a function of environment. *Upper panel:* Composite three-colour image towards the nearby disc galaxy NGC 1300, taken using HST observations as part of the PHANGS survey [9] (see also [10, 11]). *Lower panel:* Composite three-colour image of the CMZ, taken using the *Spitzer* and *Herschel* telescopes [2, 4, 12].

Stellar feedback across whole galaxy discs

As presented in [7, 8], we investigate the role of early stellar feedback across the whole disc of 19 nearby (< 20 Mpc) spiral galaxies on the main sequence of star-forming galaxies (stellar masses in range $\log(M_\star/\mathrm{M}_\odot)= 9.4 - 11$). To do so, we use the sample of ~ 6000 HII regions identified from the PHANGS-MUSE survey (see Figure 1; [10]). The combination of these optical spectroscopic maps, and the data products provided by PHANGS-ALMA [11] and PHANGS-HST [9], are essential to constrain many fundamental internal (e.g., electron density, temperature, radiation field) and external (e.g., dynamical equilibrium pressure, environment) properties of the HII regions.

We find that for these *unresolved* (10 pc scale) HII regions, the P_{therm} is mildly dominant pressure term. We find that the majority of HII regions are over-pressured,

$P_{\rm tot}/P_{\rm de} > 1$, and expanding, yet there is a small sample of compact HII regions with $P_{\rm tot}/P_{\rm de} < 1$ ($\sim$1% of the sample). These under-pressured HII regions mostly reside in galaxy centres (galactocentric radii <1 kpc), or, more specifically, environments of high gas surface density (measured on kpc-scales). Using higher resolution observations from HST to investigating the effect of the environment on these regions represents an interesting avenue of investigation [7].

Zooming in on Centre of the Milky Way

In [4], we investigate the effect of higher ambient density and pressure host environments on the *resolved* physical properties and evolution of stellar feedback. For this, we focus on the inner few hundred parsecs of the Milky Way, the "Central Molecular Zone" (CMZ), which is known to host several HII region complexes – e.g., Sgr B2 and B1 regions (see Figure 1; e.g., [2, 12]).

The CMZ is a particularly interesting extreme environment. The average gas densities, gas temperatures, ambient pressures, turbulent velocity dispersion, interstellar radiation fields and cosmic ray ionisation rate factors of a few to several orders of magnitude larger than observed in typical Milky Way disc and SMC/LMC star-forming systems, making it more similar to starburst and high redshift galaxies at the epoch of peak star formation density at $z \sim$ 1-3 [13].

We find that the HII regions are dominated by the direct radiation pressure on only the smallest scales (<0.01 pc), and at all larger scales they appear to be dominated by the thermal pressure of the ionised gas (>0.01-10 pc). There is evidence for a modest contribution from trapped IR radiation or hot stellar wind gas early in the expansion.

Stellar feedback as a function of environment

Comparing the CMZ HII regions to the extragalactic sample (see Figure 2), and samples taken from the literature, we find that the radius at which HII regions reach pressure balance with their environments is $\sim 2-3$ pc in the Galactic Centre, versus > 10 pc in the extragalactic sample. Interestingly, we see that the maximum sizes of HII regions in the Galactic Centre match the radius at which the internal pressure matches the ambient ISM pressure for most environments. This suggests that the smaller HII region within the CMZ are limited by the point of pressure equilibrium with the more highly pressured ambient medium.

Stellar feedback regulated star formation

Given the remarkable similarity between the HII region radii and the radius at which the region pressure drops to the ambient pressure, we suggest a scenario where
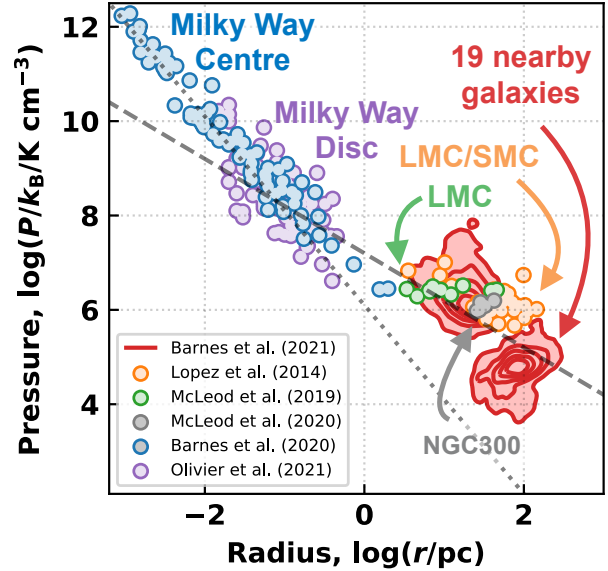

Figure 2: Literature compilation of the internal pressures of the HII regions. The total internal pressures as a function of the HII region sizes, ranging from the Milky Way centre from [4] to nearby disc from [8] (see also [14, 15, 16, 17, 18]). The dashed diagonal lines show linear and power of two relations between the pressure and sizes.

star formation can proceed until the gas accretion can be halted, irrespective of the environment. In this case, star formation and feedback self-regulate such that each cloud attains the integrated star formation efficiency required for a blowout, which happens when the developing stellar population can drive the HII region radius to the cloud (or gas disc) scale height.

References

[1] Barnes, A. T., et al. 2016, MNRAS, 458, 1990
[2] Barnes, A. T., et al. 2017, MNRAS, 469, 2263
[3] Barnes, A. T., et al. 2020a, MNRAS, 497, 1972
[4] Barnes, A. T., et al. 2020b, MNRAS, 498, 4906
[5] Chevance, M., et al. 2020, MNRAS, 493, 2872
[6] Sormani, M.C., et al. 2020, MNRAS, 497, 5024
[7] Barnes, A. T., PHANGS, et al. 2021c, in prep.
[8] Barnes, A. T., et al. 2021b, MNRAS, subm.
[9] Lee, J. C., et al. 2021, arXiv:2101.02855
[10] Emsellem, E., et al. 2021, subm.
[11] Leroy, A. K., et al. 2021, arXiv:2104.07739
[12] Barnes, A. T., et al. 2019, MNRAS, 486, 283
[13] Kruijssen, J. M. D., et al. 2013, MNRAS, 435, 2598
[14] Lopez, L. A., et al. 2011, ApJ, 731, 91
[15] Lopez, L. A., et al. 2014, ApJ, 795, 121
[16] McLeod, A. F., et al. 2020, ApJ, 891, 25
[17] McLeod, A. F., et al. 2019, MNRAS, 486, 5263
[18] Olivier, G. M., et al. 2021, ApJ, 908, 68

Short CV

2010–2014:   Bachelor/Master in Astronomy, University of Leeds, UK
2014–2018:   PhD in Astronomy, Liverpool John Moores University, UK
2014–2018:   PhD in Astronomy, Max Planck Institute for Extraterrestrial Physics, DE
2018–present: Postdoctoral position, Argelander-Institut für Astronomie, DE

Nitrogen isotopes in the interstellar medium: a chemical journey across the Galaxy

Laura Colzi

Centro de Astrobiología (CSIC-INTA), Ctra. de Ajalvir Km. 4, 28850, Torrejón de Ardoz, Madrid, Spain

One of the most important tools to investigate the chemical history of our Galaxy and our own Solar System is to measure the isotopic fractionation of chemical elements. This is the process that distributes the less abundant stable isotopes of an element in different molecular species. The isotopic ratios are governed by two main processes: 1. local fractionation effects; 2. chemical evolution of the whole Galaxy due to stellar nucleosynthesis.
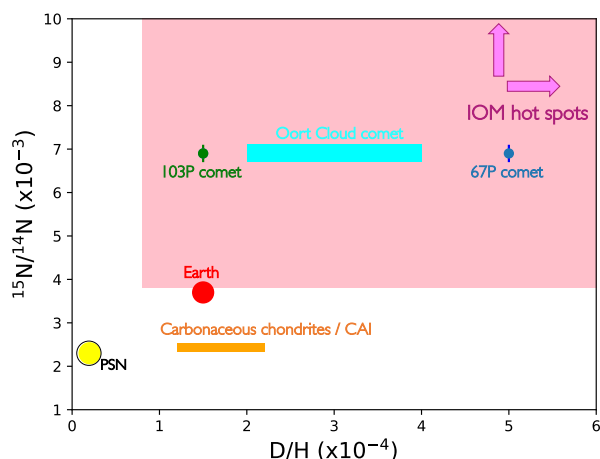

Figure 1: $^{15}N/^{14}N$ vs D/H ratios measured in comets, chondrites, hot spots in insoluble organic matter (IOM) of meteorites, Earth and the proto-Solar nebula (PSN).

Introduction

Pristine Solar System materials, like comets and carbonaceous chondrites in meteorites, present very different hydrogen and nitrogen isotopic ratios (D/H$\sim10^{-4}$ and $^{14}N/^{15}N$=50–200, e.g., [1, 2, 3] and see Figure 1) with respect to those measured for the proto-Solar nebula (PSN), in which our Sun was born (D/H$\sim2\times10^{-5}$ and $^{14}N/^{15}N$=441; [4, 5]). Star-forming regions also present a variety of isotopic ratios, with a lower enrichment of the heavier isotopes with respect to the one present in pristine Solar System materials (e.g., [6, 7, 8]; see Figure 2 for $^{14}N/^{15}N$ ratios). Nowadays observations and theoretical works about hydrogen fractionation (D/H ratios) agree about the processes that enrich deuterium with respect to hydrogen during star-formation. These processes are related to the cold phases ($T < 20$ K) of star-forming regions, where the CO freeze-out on grain surfaces and, because of this, gas-phase molecules are enriched in deuterium thanks to the so-called isotopic-exchange reactions [9]. These reactions exchange one of the hydrogen of a molecule with a deuterium. However, similar reactions cannot explain nitrogen fractionation ($^{14}N/^{15}N$ ratios). In fact, chemical models that only includes these reactions are not able to reproduce the spread of $^{14}N/^{15}N$ ratios for the different molecules and

in the different physical conditions of the observed targets (e.g., [10, 11, 12].) This indicates that other physical and/or chemical processes are needed to explain the observed values.

Today, there is growing evidence supporting the idea that our Sun was born in a stellar cluster including also massive stars, with masses higher than 8 M$_\odot$ (e.g., [13]). For this reason, the study of the chemical content of massive star-forming regions can give us crucial information about the chemical heritage of our Solar System.
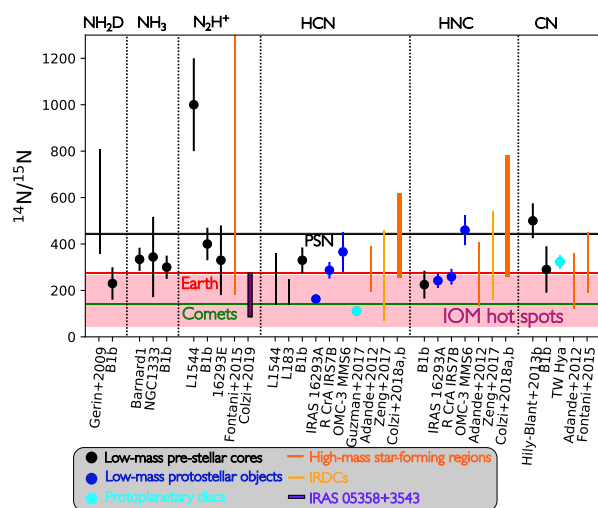

Figure 2: $^{14}N/^{15}N$ ratio derived for different molecules and towards different star-forming regions, as indicated in the legend. The horizontal yellow and red solid lines represent the PSN value of 441 and the terrestrial atmosphere (TA) value of 272, respectively. The green horizontal line denotes the average value measured in comets. Moreover, the pink area represents measurements in carbonaceous chondrites, where the lower ones are the so-called "hot spots".

The role of Galactic chemical evolution

The isotopic ratios measured in interstellar molecular clouds not only depends on local chemical fractionation effects, but also on the chemical evolution of the whole galaxy due to stellar nucleosynthesis. In particular, the $^{14}N/^{15}N$ elemental ratio is a good indicator of stellar nucleosynthesis since the two elements are not produced in the same way (e.g., [14]). In this context, we have studied N-fractionation towards a statistically significant sample of 87 massive star-forming regions located at galactocentric distances (D_{GC}) from 2 up to 12 kpc. We have derived the $^{14}N/^{15}N$ ratios for HCN and HNC as a function of the galactocentric distance, and compared the results with Galactic chemical evolution (GCE) model predictions ([15, 16]; see Figure 3). These models predict a linear positive $^{14}N/^{15}N$ ratio up to 8 kpc, and a flattening

trend for higher distances. This behavior is mainly due to the production of ^{15}N in nova outbursts [14, 17]. The results we have obtained shows an agreement between models and observations, confirming the importance of nova outbursts for the ^{15}N enrichment along the Galactic disc. Furthermore, we have found a local ^{14}N/^{15}N ratio of $\sim$375, consistent with a local chemical evolution due to stellar nucleosynthesis. Thus, stellar nucleosynthesis processes can explain, on average, the observed ^{14}N/^{15}N values, which are lower than the PSN value, but are not able to reproduce the different values from region to region, and from molecules to molecule.
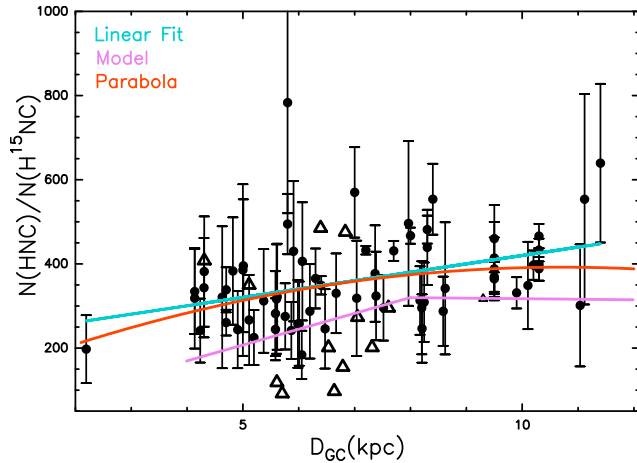

Figure 3: ^{14}N/^{15}N ratios for HNC as a function of the galactocentric distance (D_{GC}). The cyan solid line is the linear regression fit computed for the two data sets, the red parabola is the results from the parabolic analysis described in detail in [16], and the pink solid line represents the GCE model of [14].

Local chemical effects

To investigate more in detail the processes that could enrich ^{15}N in molecules during the star-formation process, we have studied high-angular resolution observations (3", i.e. $\sim$6200 au) from the IRAM NOEMA interferometer of the massive protocluster IRAS 05358+3543 [18]. In particular, we have resolved for the first time the spatial distribution of the ^{15}N-isotopologues of N$_2$H$^+$ at core scales (about 0.03 pc, Figure 4). The spatial resolution of these observations is one order of magnitude higher than previous works, allowing to distinguish the emission of dense cores inside a more diffuse envelope in which they are embedded. The maps of ^{15}NNH$^+$ and N^{15}NH$^+$ shows that the ^{14}N/^{15}N ratio of N$_2$H$^+$ is lower in the inner denser cores ($\sim$100–200) with respect to the more diffuse gas ($>$250). This result highlights the importance of local effects, and in particular it demonstrates that isotope-selective photodissociation of N$_2$ should be introduced in chemical models to explain ^{15}N-enrichment in star-forming regions (e.g., [18, 19, 20]).
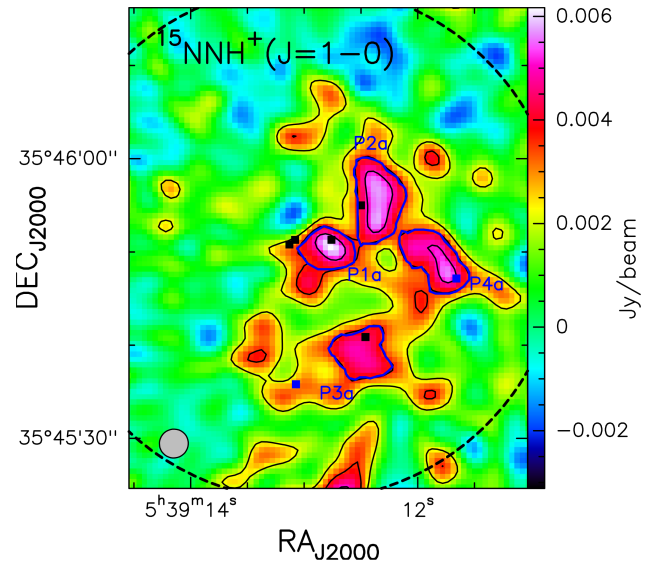

Figure 4: First interferometric maps of the J=1−0 transition of ^{15}NNH$^+$. The black contour levels are 3, 5 and 7 times the 1σ of the map (0.72 mJy beam^{-1}). The blue contours correspond to the 5σ of the map, from which the ^{14}N/^{15}N ratios have been derived. The black and blue squares indicate the positions of the continuum sources and other N$_2$H$^+$ peak positions, respectively. The dashed circle represents the NOEMA field of view and the synthesized beam is the ellipse indicated in the lower left corner.

References

[1] Hartogh, P., et al. 2011, Nature, 478, 218
[2] Bonal, L., et al. 2009, Met. Planet. Sci. Suppl., 72, 5178
[3] Manfroid, J., et al. 2009, A&A 503, 613
[4] Zavarygin, E. O., et al. 2018, MNRAS, 477, 5536
[5] Marty, B., et al. 2010, Geoch. et Cosmoch., 74, 340
[6] Hily-Blant, P., et al., 2013a, Icarus, 223, 582
[7] Daniel, F., et al. 2016, A&A, 592, A45
[8] Redaelli, E., et al. 2018, A&A, 617, A7
[9] Caselli, P., & Ceccarelli, C., 2012, A&ARv, 20, 56
[10] Roueff, E. et al. 2015, A&A, 576, 99
[11] Wirström, E., Charnley, S. B. 2018, MNRAS, 474, 3720
[12] Loison, J-C. et al. 2019, MNRAS, 484, 2747
[13] Adams, F. C. 2010, ARA&A, 48, 47
[14] Romano, D., et al. 2017, MNRAS, 470, 401
[15] Colzi, L., et al. 2018a, A&A, 609, A129
[16] Colzi, L., et al. 2018b, MNRAS, 478, 3693
[17] Romano, D., et al. 2019, MNRAS, 490, 2838
[18] Colzi, L., et al. 2019, MNRAS, 485, 5543
[19] Heays, A. N., et al. 2014, A&A, 562, A61
[20] Furuya, K., & Aikawa, Y. 2018, ApJ, 857, 105

Short CV

2013: Bachelor in Physics and Astrophysics, University of Florence, Italy
2016: Master in Physical and Astrophysical Sciences, University of Florence, Italy
2020: European PhD (Doctor Europaeus) in Physics and Astronomy, University of Florence, Italy
2021: Postdoctoral researcher, Centro de Astrobiología, Torrejon de Ardoz, Madrid

The "shocking" interaction between supernova remnants and molecular clouds

Giuliana Cosentino

Department of Space, Earth and Environment, Chalmers University of Technology, SE-412 96 Gothenburg, Sweden

Massive stars (M$\geq$8 M$_\odot$) drive powerful stellar feedback that profoundly affects the evolution and star formation efficiency (SFE) of the hosting galaxies. Among these mechanisms, feedback driven by supernova explosions (SNe) are some of the most energetic [1] and long-lasting [2, 3], and therefore among the most effective. As the remnant (SNR) expands, the hot plasma pushes and compresses outwards the atomic and molecular gas in contact with the remnant [4] and injects energy, mass and momentum into the interstellar medium (ISM), profoundly affecting its physical and chemical properties [5]. At the typical cloud spatial scales ($<$10 pc), SNRs drive slow shock compression that impact onto nearby pre-existent molecular clouds and locally enhance the density of the molecular material [6, 7]. This increases the gas turbulence and eventually triggers the formation of new stars [8, 9]. It has been shown that SNR-cloud interactions can enhance cloud SFE in nearby galaxies up to $>$40% [10]. It is thus important to observationally investigate the effects that supernova feedback has on the molecular phase of the ISM, i.e., the material that primarily fuels star formation in galaxies. The study of SNR-cloud interactions can enable a better understanding of the star formation enhancement and suppression in the ISM.
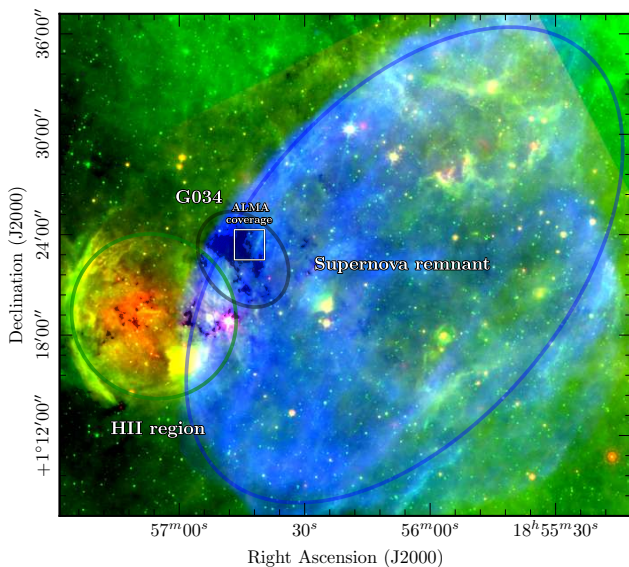

Figure 1: Three-color image showing the position of W44 (blue circle) with respect to G034.77-00.55 (black circle). A nearby Hii region is also indicated (green circle). Red is 24 μm emission (Spitzer MIPSGAL) [11], green is 8 μm emission (Spitzer GLIMPSE) [12], and blue shows a combined JVLA +GBT 21 cm continuum map (THOR survey) [13]. The white square indicates the ALMA mosaic area.

The W44-G034 shock interaction.

Among the best known sites of SNR-cloud interaction is the one occurring between the SNR W44 and the nearby Infrared Dark Cloud (IRDC) G034.77-00.55 (hereafter, G034) [14, 15, 16]. In Figure 1, the relative location of W44 and G034 is shown. The expansion of the 20k years old core-collapse SNR pushes away the surrounding molecular material that interacts with the pre-existing IRDC [6]. Towards this region, we have used the silicon monoxide SiO(2-1) emission at 86.6 GHz, to study the morphology, dynamic and kinematics of the shocked molecular gas [17, 6]. SiO is a unique shock tracer, whose abundance is usually very low in quiescent regions, but becomes extremely enhanced in the presence of shocks, where dust sputtering occurs [18, 19, 20].
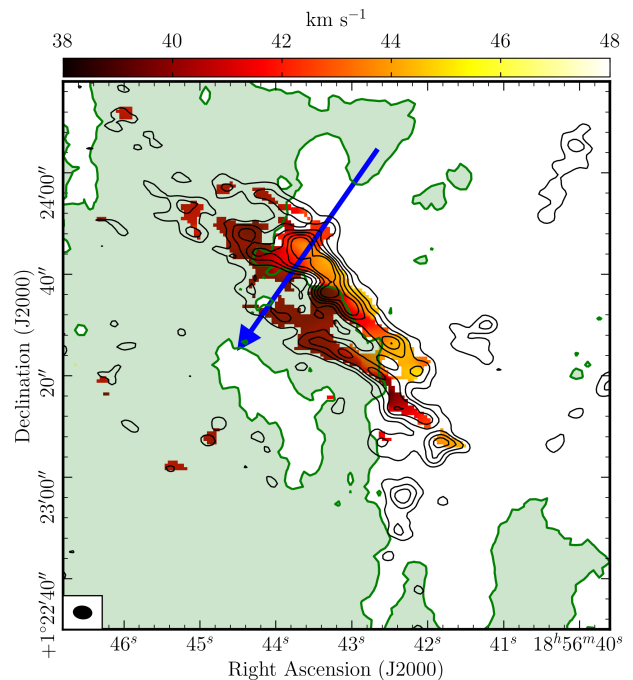
Figure 2: SiO integrated intensity map (black contours; velocity range 36.6$-$47.6 km s^{-1}) toward G034 superimposed on its first moment velocity map (red scale). Contours are from 3σ (σ=0.016 Jy km s^{-1}) by steps of 3σ. The Av$>$20 mag dense material in the IRDC is indicated as green contour and shadow [21]. The beam size is indicated as a black ellipse in the bottom left corner.

The SiO emission toward the W44-G034 interactions site is shown in Figure 2 as mapped at high-angular resolution with the Atacama Large Millimetre/sub-millimetre Array (ALMA). The shocked gas emission is organised into two elongated structures caught in the act of decelerating (from $\sim$46 km s^{-1} to $\sim$39 km s^{-1}) and plunging into

a dense ridge at the edge of G034. This behaviour is similar to that of a see wave (the shocks) plunging and breaking into a sandy shore (the cloud dense ridge). Towards the dense ridge, no signature of ongoing star formation activity that may account for the observed SiO emission are found. As seen from multiple $C^{18}O$ transitions (IRAM-30m), the shock propagation enhances the gas density within the ridge to values $n(H_2)>10^5$ cm^{-3}, compatible to those required to enable star formation [22]. The momentum injected into the dense shocked gas is estimated to be $\sim$20 $M_\odot$ km s^{-1} [6].

Figure 3: Logo of the SHREC survey. Credit: Giulia Zora.

SHREC: SHock interaction between supernova REmnants and molecular Clouds

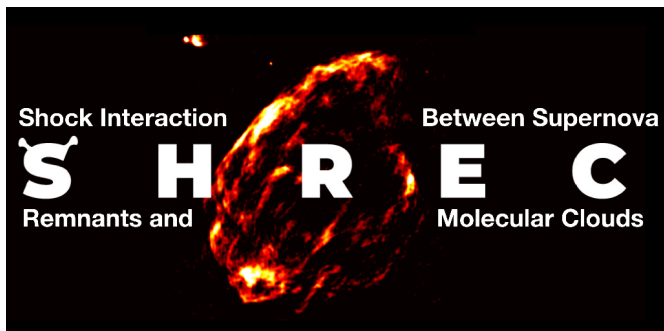In order to extend the study of feedback driven by SNRs in molecular clouds, we have initiated the exploratory ESO-ARO large program SHREC i.e. SHock interactions between supernova REmnants and molecular Clouds (P.I. Cosentino; Figure 3). SHREC uses the 12m antenna at the Arizona Radio Observatory (ARO) to detect SiO(2-1), $H^{13}CO^+$(1-0) and $HN^{13}C$(1-0) emission towards a sample of 27 SNRs. These sources are located relatively nearby (kinematic distance $\leq$ 6 kpc) and show previous evidence of interaction with the surrounding molecular material [23, 24], i.e., enhanced X-ray emission, the presence of OH maser emission, and enhanced CO(2-1)/CO(1-0) ratios [5]. The final goal of SHREC is to identify sites of large-scale interactions driven by SNRs and to investigate how these affect the star formation potential and dispersal of the surrounding molecular material (Cosentino et al., in prep.).

Conclusions

We have used the unique capability of ALMA to investigate the morphology, dynamic and kinematic structure of the shocked gas emission toward the W44-G034 interaction site. We find that the shocked gas morphology resemble that of plane-parallel shock front driven by W44 and plunging into the dense ridge at the edge of the cloud. The shock propagation through the molecular material efficiently compress the gas, increasing its densities to values comparable to those required for the formation of massive stars. The high-angular resolution achieved also allows to pierce into the internal physical structure of the shock, providing optimal tools to test our current MHD shock theories. It is therefore necessary to extend the sample of SNR-cloud interaction sites seen by shock molecular tracers to evaluate their relevance in setting the initial conditions for star formation in the ISM.

References

[1] Bally, J. 2011, Computational Star Formation, 270, 247
[2] Leitherer, C., et al. 1999, ApJS, 123, 3
[3] Agertz, O., et al. 2013, ApJ, 770, 25
[4] Chevalier, R. A. 1974, ApJ, 188, 501
[5] Slane, P., et al. 2016, Multi-scale Structure Formation and Dynamics in Cosmic Plasmas, 187
[6] Cosentino, G., et al. 2019, ApJL, 881, L42
[7] Dell'Ova, P., et al. 2020, A&A, 644, A64
[8] Inutsuka, S., et al. 2015, A&A, 580, A49
[9] Klessen, R. S., & Glover, S. C. O. 2016, Saas-Fee Advanced Course, 43, 85
[10] Rico-Villas, F., et al. 2020, MNRAS, 491, 4573
[11] Carey, S. J., et al., 2009, PASP, 121, 76
[12] Churchwell, E., et al., 2009, PASP, 121, 213
[13] Beuther, H., et al. 2016, A&A, 595, 21
[14] Wootten, H. A. 1977, ApJ, 216, 440
[15] Sashida, T., et al. 2013, ApJ, 774, 10
[16] Cardillo, M., et al. 2014, A&A, 565, A74
[17] Cosentino, G., et al. 2018, MNRAS, 474, 3760
[18] Martín-Pintado, J., et al. 1992, A&A, 254, 315
[19] Schilke, P., et al. 1997, A&A, 321, 293
[20] Jiménez-Serra, I., et al. 2005, ApJL, 627, L121
[21] Kainulainen, J., & Tan, J. C. 2013, A&A, 549, 28
[22] Parmentier, G., et al. 2011, MNRAS, 416, 783
[23] Ferrand, G., & Safi-Harb, S. 2012, Adv. Space Res., 49, 1313
[24] Green, D. A. 2019, JAA, 40, 36

Short CV

2013: Bachelor in Physics, University of Palermo, Italy
2015: Master in Physics and Astronomy, University of Palermo, Italy
2018: ESO Visiting PhD student, European Southern Observatory, Germany
2019: PhD in Astronomy, University College London, UK
2019: CICO Origins Postdoctoral Fellow, Chalmers University of Technology, Sweden

From clouds to crust:
Cloud diversity and surface conditions in atmospheres of rocky exoplanets

Oliver Herbort

St Andrews Centre for Exoplanet Science

Schools of Physics and Astronomy & Earth and Environmental Science, University of St Andrews, UK

The surface composition of rocky planets outside of our solar system is very hard to be determined, especially if the planet has a cloud layer, which can potentially cover the entire planet. However, future observations will allow the investigation of the high atmospheric gas composition and can provide insights to the composition of potential clouds that are present. We want to link our understanding of these higher atmospheric conditions to the conditions at the surface. In other words: what can we learn about the crust composition from the clouds?

Bottom to top atmospheric model

In order to investigate this question, we build a quick and simple bottom to top atmospheric model, which is in contact with the crust underneath. This allows the study of atmosphere based on various surface conditions (Pressure, temperature, and composition).

Figure 1: Schematic view of the atmospheric model presented here. The bottom to top atmosphere is in chemical phase equilibrium with the surface. Thermally stable condensates are taken out of the atmosphere and the atmosphere is depleted with respect to the effected elements. [3]

Our model is based on a crust-atmosphere interaction layer, which is assumed to be in chemical and phase equilibrium [1]. The model is part of the equilibrium chemistry model GGchem [2]. Based on the total element abundance ϵ_{tot}, surface temperature T_{surf} and surface pressure p_{surf}, the crust rock composition ϵ_{cond} is determined as well as the gas composition in the near crust atmosphere $\epsilon_{gas}(0)$. This gas composition provides the first layer for the atmospheric model.

Based on this atmosphere-crust interaction layer, we build a bottom to top atmosphere under the assumption of a polytropic atmosphere in hydrostatic equilibrium [3]. In each atmospheric layer i, we solve the chemical phase equilibrium ($\epsilon^0(i) = \epsilon^{gas}(i) + \epsilon^{cond}(i)$). All thermally stable condensates are removed, which depletes the atmosphere above with respect to the effected elements (see also Figure 1). The remaining gas phase abundances are forming the total element abundances of the atmospheric layer above $\epsilon^0(i+1) = \epsilon^{gas}(i)$.

Water as part of the crust composition

One of the major questions with respect to astrobiology is, whether a planet has liquid water at its surface. In [1], we show that the formation of liquid water is inhibited by the formation of phyllosilicates. These hydrated rocks incorporate OH into their lattice structure. Before water is a stable condensate, all pyhllosilicates have to have formed.

Cloud diversity

Figure 2 shows the most abundant thermally stable condensates for models based on Bulk Silicate Earth and CI chondrite composition, for surface pressures of 1 bar and surface temperature ranging from 300 K to 1000 K. The thermally stable condensates can be separated into two different categories, high and low temperature condensates. The only condensate that is stable in both temperature regimes is graphite (C[s]).

For atmospheres with liquid water at the surface, water clouds are thermally stable throughout the atmosphere. However, models without water condensates as part of the crust still show conditions with thermal stability of water in higher parts of the modelled atmospheres. This shows that water clouds themselves are not necessarily indicative for water at the surface of the planet. A major constraint on the atmospheric height of the water cloud base is the hydration level of the models crust.
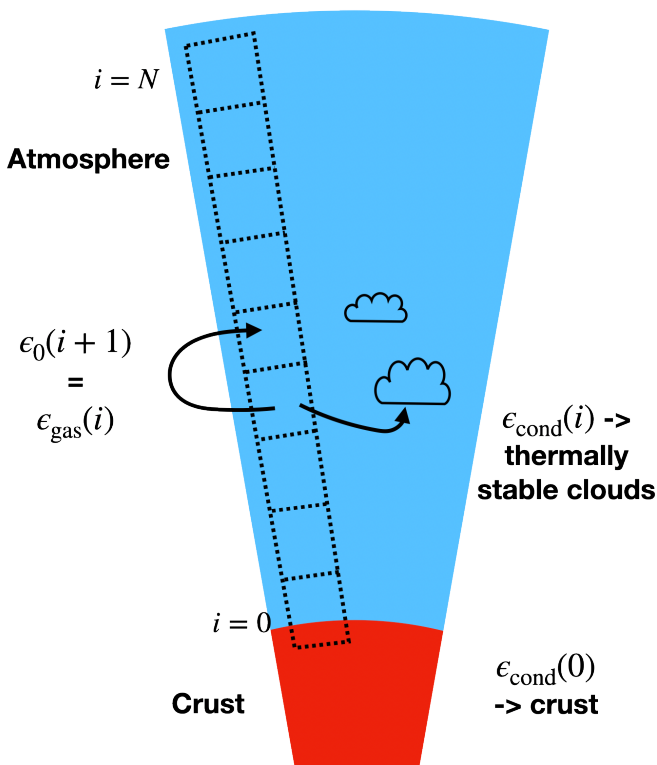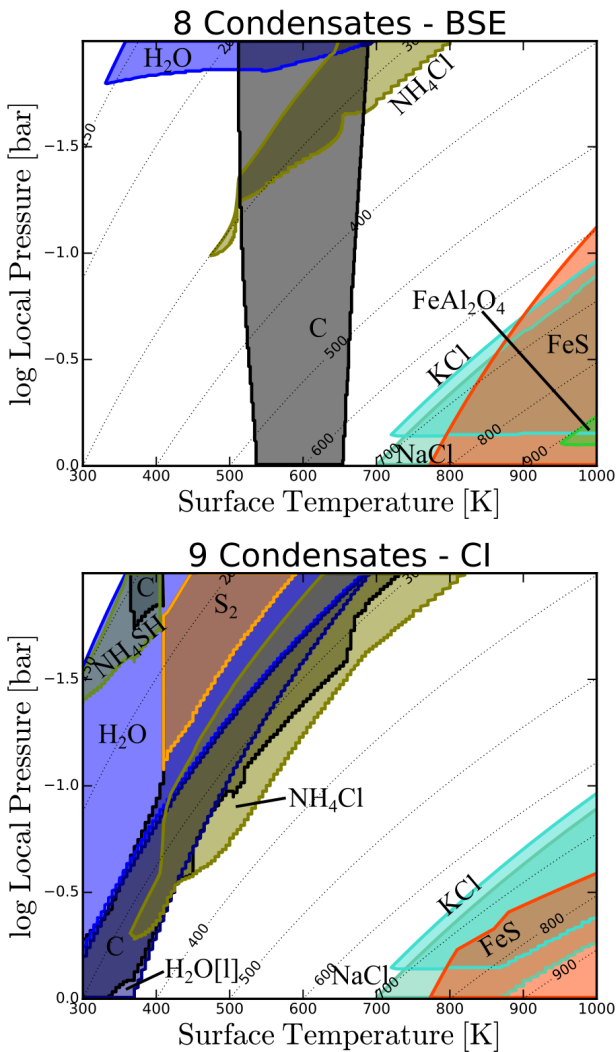
Figure 2: Most abundant thermally stable cloud condensates in the atmospheric models for Bulk Silicate Earth (top) and CI chondrite (bottom) total element abundances.

	Type A	Type B	Type C
H_2O	✔	✔	✔
CO_2	✘	✔	✔
CH_4	✔	✘	✔
O_2	✘	✔	✘
H_2	✔	✘	traces
$H_2O[l,s]$	✔	✔	✔
$C[s]$	✘	✘	✔

Figure 3: Atmospheric types in the CHO space with overplotted atmospheric models for Bulk Silicate Earth models. The Table lists the important molecules and condensates for the atmospheric types [4].

Atmospheric composition

In [4], we showed that the gas phase composition of atmospheres containing CHNO can be categorized into three different atmospheric types. The three resulting atmospheric types (triangle in Figure 3 top) show distinctive gas phase compositions (table Figure 3). These atmospheric types are independent of pressure, temperature (below 600 K) and overall Nitrogen content.

Although the atmospheric composition changes with increasing height, the atmospheric type in which the entire atmosphere falls is determined by the atmospheric type set by the near crust atmospheric composition. The atmospheric type does not change due to condensation in the atmosphere. However, significant changes in surface pressure and surface temperature can result in a change of an atmospheric type for the entire atmosphere.

Summary

The fast and simple atmospheric model presented provides the opportunity to investigate the influence of changes in total element abundances on atmospheric composition and thermally stable cloud condensates.

Water can only form as a condensate at the planetary surface if the phyllosilicates are saturated. In the atmosphere above such a surface, water clouds are thermally stable in the crust-atmosphere contact layer as well as the atmospheric layers above, the water cloud base touches the ground. Models without water at the surface still show thermal stability of water in their respective atmospheres. This underlines that the presence of water condensates in the atmosphere does not necessarily imply water at the surface of the planet.

References

[1] Herbort, O., et al., 2020, A&A, 636
[2] Woitke, P., et al. 2018, A&A, 614
[3] Herbort, O., et al. submited to A&A
[4] Woitke, P., et al. 2021, A&A, 646

Short CV

2013–2016: Bachelor in Physics, Georg August Universität, Göttingen
2016–2018: Master in Physics, Georg August Universität, Göttingen
2018–2022: PhD in Astrophysics and Geology, St Andrews Centre for Exoplanet Science, UK

Probing the effects of environment on star and brown dwarf formation

Karolina Kubiak

CENTRA, Faculdade de Ciências, Universidade de Lisboa, Portugal

Brown dwarfs (BDs) are substellar objects not massive enough to sustain hydrogen fusion. Following this definition, we consider 75 M_{Jup} (0.072 $M_\odot$, the hydrogen-burning limit) as an upper mass limit for BDs. The lower mass limit is not as clear, since objects with masses below 13 M_{Jup} (0.012 $M_\odot$, deuterium-burning limit) not orbiting stars have been found already.

Young brown dwarfs can have effective temperatures and luminosities in the stellar range and be spectroscopically M type, then age into L dwarf regime, to end up with the temperatures of T dwarfs or massive Jovian planets [1]. BDs overlap in temperature and luminosity with both low-mass stars and planets; they also share properties with each realm. BDs not only are self-luminous, hosts to planets, discs, and outflows, but also share mass and multiplicity distributions with stars. All known BDs have similar radii (within a factor of 2) and present ultra-cool atmospheres similar to giant planet.

With such a vast combination of characteristics, BDs become one of the hot topics of modern astronomy. The question "How do such low-mass and abundant objects form?" can be naively answered in one of three possible ways: as stars, like planets or neither way. BDs can be born in the same way as very-low-mass stars through the gravitational fragmentation of infalling gas into stellar clusters [2]. Pre-stellar cores may form companion BDs in a similar way to giant planets via disk fragmentation and ejection [3]. Stellar embryos can be ejected from multiple systems during formation and thus cut-off from their accretion reservoir and evolving only into a substellar object [4]. Another viable channel for BD formation has been suggested by [5], where powerful ionisation fronts from OB stars can gradually destroy the outer layers of massive pre-stellar core, leaving a small fragment.

The current consensus is that most brown dwarfs form like stars, at least in the case of more massive BDs. Nevertheless, still, some unresolved questions in the formation of BDs need to be addressed: How far in mass does the stellar Initial Mass function (IMF) extend? Do the lowest-mass objects form "like stars" or "like planets"? Is BD formation environment dependent?

Many surveys have been dedicated to studying this problems by finding and comparing complete censuses of BDs for particular regions. Most of them, such as SONYC (Substellar Objects in Nearby Young Clusters), focuses on nearby star-forming regions (SFRs). SONYC obtained deep substellar IMF using the consistent methodology of deep optical and near-infrared photometry with spectroscopic follow-up necessary to confirm the youth and BD nature of substellar objects. The overall results from this and other surveys find the universality of low-mass end of IMF in nearby SFRs (expressed as power-law with slope $\alpha = 0.6 - 1$). They also find that for every BD formed, there are 2 to 6 stars; despite the large range, this number is consistent with a single underlying IMF. The wide range in the star-to-BD ratio is likely caused by uncertainties due to incompleteness of the spectroscopic follow-up, mass estimation, etc. and does not necessarily express the difference between regions. Strong IMF variations are excluded for most nearby SFRs. An overabundance of very low mass objects has been reported in IC 348, [6] and NGC 1333 [7], and hint that the change in environment may indeed affect the efficiency of BD formation.

The environmental difference is, in fact, theoretically expected, as most of the current BD formation theories predict an overproduction of substellar objects in dense environments or the vicinity of massive stars. To test the low mass star and brown dwarf formation across environments, we move to drastically different conditions looking for the most radical and extreme properties that can be found only in the most massive clusters. We selected three young massive clusters that encompass the wide range of initial conditions for star formation. RCW38, one of the densest and most massive young clusters; RCW36, dense, but with a few OB stars, and NGC2244, which is loose and rich in OB stars. Studying massive clusters brings many challenges for data reduction and analysis, from which the most important are: distance and high extinction due to the high column density molecular clouds with which they are associated, and in some cases crowding.

Figure 1: JHK colour-composite of RCW 38 obtained with Hawk-I/GRAAL, with the NACO observations in the central part.

This contribution gives insight into our preliminary analysis of the deepest and largest near-infrared imaging survey in RCW38. Located in the Vela complex, at a distance of 1.7 kpc, it hosts dozens of OB star candidates. RCW38 is more than twice as dense as the Orion Nebula Cluster and orders of magnitude denser than other nearby SFR.

Previous near-infrared studies of the cluster used data from NAOS-CONICA/VLT and covered about 0.5x0.5 pc in the cluster's core (see Figure 1). The IMF presented in [8] as a power-law with a slope of 0.4±0.2 for low-mass and 1.5±0.1 for massive stars stays in agreement with results for nearby SFRs. Our recent studies obtained by HAWK-I/GRAAL cover a 64 times larger field and contain 20 times more objects, allowing us to study most of the massive cluster (3.7 by 3.7 pc). The 90% completeness limits are J =19.8mag, H = 19.6mag and Ks = 17.7mag as the average values for the full field.

Figure 2 presents the colour-magnitude diagram (CMD) of all the sources detected in the JHK HAWK-I images. One can easily see that substellar objects can be detected at such large distances and substantial extinction.

Using colour-magnitude and colour-colour diagrams, we derived extinction values and masses to the sources in RCW38. Given the young age of the cluster, we expect many sources to host disks or envelops; therefore, we find it necessary to correct for this additional intrinsic excess. The applied correction depends on the position of the star in the J-H vs H-K space. Suppose the star falls in the region where the colours are consistent with reddened evolutionary models. In that case, no correction is applied, extinction and mass are obtained by simple de-reddening the source photometry to the isochrone in J vs J-H CMD. If the stars lie inside the colour-colour space attributed to the redder CTTS or Herbig AeBe stars, we de-redden them by applying the additional correction. The exact procedure is described in detail in [8].

Confirming a membership of individual sources in our field is not straightforward beside a small fraction of the clearly foreground population that separates nicely on the CMD. The bulk of sources are a mixture of cluster and field members. We, therefore, assess statistically the contamination from background sources by comparing the cluster and control field CMDs. We divided both CMDs into identical grids in both colour and magnitude directions. Next, we calculated the number densities of stars in every cell in each diagram as a sum of individual star's probability, whereas a Gaussian probability distribution represents each star of magnitude and colour, with the widths determined by the uncertainties as shown in [9]. In the last step, cell by cell, the amount of objects associated with the expected control field population is then randomly removed from the cluster CMD. The procedure
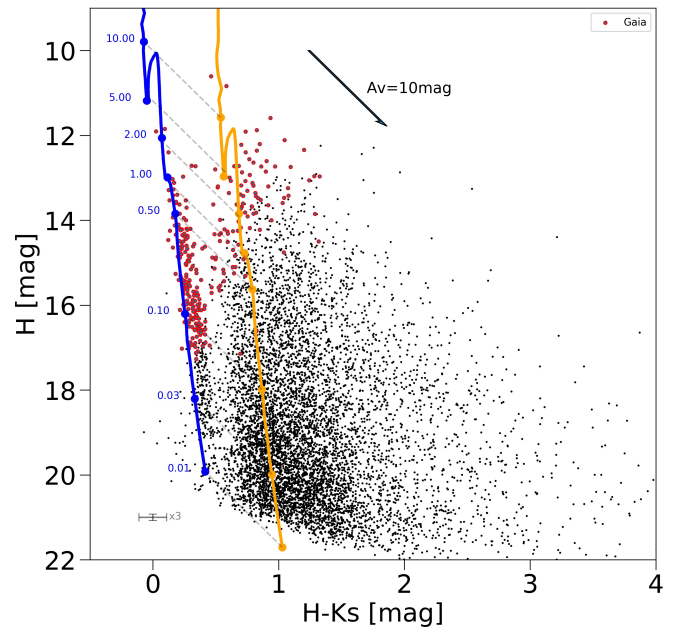

Figure 2: H vs H-Ks color-magnitude diagram of the sources detected towards RCW38. Red dots indicate sources with Gaia parallaxes. The blue solid line shows the 1 Myr isochrone shifted to the distance of 1.7 kpc, the orange line represents the same isochrone reddened to the A_V =10mag. The model masses are marked on the left side of the isochrone, dashed lines indicate corresponding points on the extincted isochrone.

is repeated for different sizes, and initial positions of the grid result in various membership lists, which were used to estimate uncertainties of the IMF.

Summary and conclusions

We present the deepest and largest near IR survey in RCW38. We find no clear evidence for variations in the formation efficiency of BDs and very low-mass stars due to the presence of OB stars, or a change in stellar densities. We find the IMF in a form of segmented power law: $\alpha = 0.6 \pm 0.15$ for $M < 0.3\,M_\odot$, and $\alpha = 1.69 \pm 0.18$ for $M > 0.3\,M_\odot$. The star-to-BD ratio (N($\star$)/N(BD) = 2 to 4) also does not seem to depend on neither the stellar density, nor presence of OB stars. A detailed description of our work will be presented in a forthcoming publication (Kubiak et al., in prep.).

References
[1] Burrows A. 2001, Reviews of Modern Physics, 73, 719
[2] Bonnell, I.A., et al. 2008, MNRAS, 389, 1558
[3] Stamatellos, D., et al. 2007, MNRAS, 382, 30
[4] Reipurth, B., & Clarke, C., 2001, AJ, 122, 432
[5] Whitworth, A.P., & Zinnecker, H., 2004, A&A, 427, 299
[6] Scholz, A., et al. 2013, ApJ, 775, 138
[7] Luhman, K., et al. 2016, ApJ, 827, 52
[8] Mužić, K., et al. 2017, MNRAS, 471, 3699
[9] Bonatto, C., & Bica, E., 2007, A&A, 473, 445

Short CV

2014: Master in Astronomy, Wrocław, Poland
2019: PhD in Astronomy, Vienna, Austria
2021: CENTRA - Faculdade de Ciencias, Universidade de Lisboa, Portugal

Accretion behaviour during binary star formation

Rajika Kuruwita

Niels Bohr Institute, University of Copenhagen, Øster Voldgade 5-7, DK-1350, Copenhagen K, Denmark

Binaries of separations $\lesssim 10\,\mathrm{AU}$ cannot form in situ during molecular core collapse because the initial hydrostatic core that collapses to form the protostar has a radius of $\sim 5\,\mathrm{AU}$ [1], and this hydrostatic core is not susceptible to fragmentation during the second protostellar collapse phase [2]. Therefore, binaries with a semi-major axis $a \lesssim 10\,\mathrm{AU}$ likely form via the in-spiral of an initially wider binary, possibly via viscous evolution through discs [3]. During viscous evolution of the gas disc, the angular momentum of the binary can be transferred to the gas, thus shrinking the orbit of the binary. During this dynamical evolution, accretion events may be triggered.

In this proceedings, I summarise the work published in [4], where we investigated any dependence of eccentricity and the accretion rate during accretion bursts triggered by a binary companion.

Methods

We use the adaptive mesh refinement (AMR) code FLASH [5] to integrate the compressible ideal MHD equations. The size of the three-dimensional computational domain is $\sim 8000\,\mathrm{AU}^3$ and with AMR, we obtain a resolution of $\sim 1.95\,\mathrm{AU}$ when fully refined. At this resolution the accretion radius of the sink particles is $r_{\mathrm{sink}} \sim 4.9\,\mathrm{AU}$.

Our simulations begin with a spherical cloud of mass $1\,\mathrm{M}_\odot$, and radius $\sim 3300\,\mathrm{AU}$ placed in the centre of the simulation domain. The cloud is initially given solid body rotation with angular momentum of $1.85 \times 10^{51}\,\mathrm{g\,cm^2\,s^{-1}}$. An initially uniform magnetic field of $100\,\mu\mathrm{G}$ is also threaded through the cloud in the *z*-direction. The cloud is initially given a uniform density of $\rho_0 = 3.82 \times 10^{-18}\,\mathrm{g\,cm^{-3}}$, and a density perturbation is imposed on the cloud. This is to seed the formation of a binary-star system. An initial turbulent velocity field is imposed on top of the solid body rotation. We run two simulations with turbulence of Mach number $\mathcal{M} = 0.1$ and 0.2, which are referred to as *T1* and *T2* hereafter.

Analysis and Results

The binary star systems form in the simulations and evolve. They accrete mass and during the early in-spiral of the binaries, we observed spikes in accretion correlated with the periastron passage of the binaries. In order to understand the dependence of accretion bursts and eccentricity, the accretion data of the binaries needs to be phase-folded. To do this, the times of periastron and apastron must be found and are defined as orbital phase, $\phi = 0$ and 0.5, respectively. After these are found, the sink particle data is divided into ten time bins between each periastron and apastron, which results in a total of 20 time bins or phase-space bins between consecutive periastrons. In each bin, the average accretion rate $\langle \dot{M} \rangle$ is calculated. After the phase-folding is completed, the median accretion rate in each phase-space bin is calculated and the orbit-to-orbit variation for each bin is taken to be the 16th and 84th percentile. Since the eccentricity of the binary is also evolving over the course of the

simulations, it is not appropriate to phase-fold the accretion over the entire duration of the simulation. In order to study the dependence of the intensity of episodic accretion on eccentricity, we define eccentricity bins to phase-fold over. For *T1*, these eccentricity bins were selected to be $e = [1.1, 0.7, 0.5, 0.4, 0.3, 0.2, 0.1, 0.0]$. As the eccentricity in *T2* reduces at a faster rate than in *T1*, these same bins were not appropriate for *T2*, because in some bins only two orbits would be folded. Thus, for *T2*, we adjusted the bins to be $e = [1.1, 0.7, 0.5, 0.3, 0.1, 0.0]$.

To determine the strength of a burst, we calculate β, which is the ratio between the burst ($\dot{M}_b$) and quiescent ($\dot{M}_q$) accretion rates. $\dot{M}_b$ is the average accretion rate between phases $0.8 < \phi < 1.1$. $\dot{M}_q$ is taken to be the average accretion rate between phases $0.2 < \phi < 0.75$. β against eccentricity is shown in Figure 1, and we find $\beta \sim 1$ for eccentricities $e < 0.2$, i.e. consistent with no episodic accretion. For *T1*, the strength of episodic accretion peaks at moderate eccentricities, $0.2 < e < 0.6$. A similar trend is seen for *T2* with higher eccentricities displaying stronger episodic accretion up to the highest eccentricities. While *T1* peaks at $\beta \sim 3$, *T2* produces higher β for higher eccentricity. This may suggest some dependence of the strength of episodic accretion on the level of turbulence, with stronger turbulence producing stronger accretion. Based on the derived β values, we approximate that binaries with eccentricities $e \gtrsim 0.2$ should display episodic accretion.
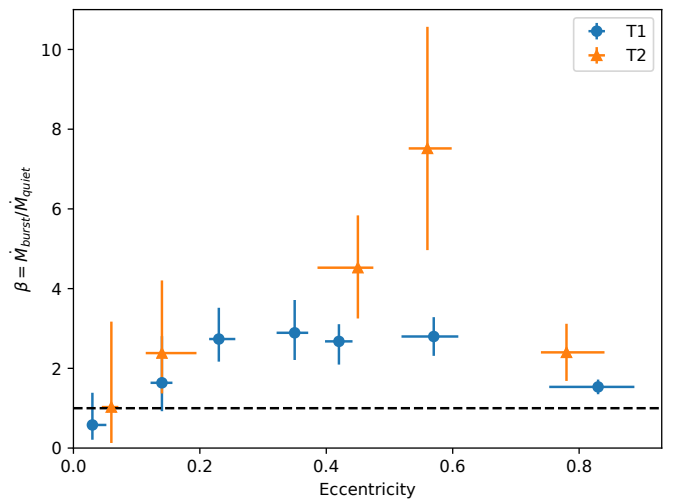
Figure 1: Strength of accretion vs binary eccentricity.

To understand the mechanism which drives the accretion rate, we look closely at the periastron passage of one of our high-resolution simulations. Projections of this is shown in Figure 2. We see from the figure that the approach of the companion distorts the circumstellar disc, which excites a spiral wave. It is the approach of the companion that removes angular momentum from the gas in the outer disc due to the different angular velocities. This angular momentum is transferred from the

Figure 2: Zoom in projections of the first periastron in our high-resolution simulation. The solid lines are density contours spaced evenly in log-space.

gas to the stellar orbits. After periastron, we see that the material is ejected outward, and this is because momentum from the binary orbit is imparted into the gas to push it to higher orbits, and the binary separation is reduc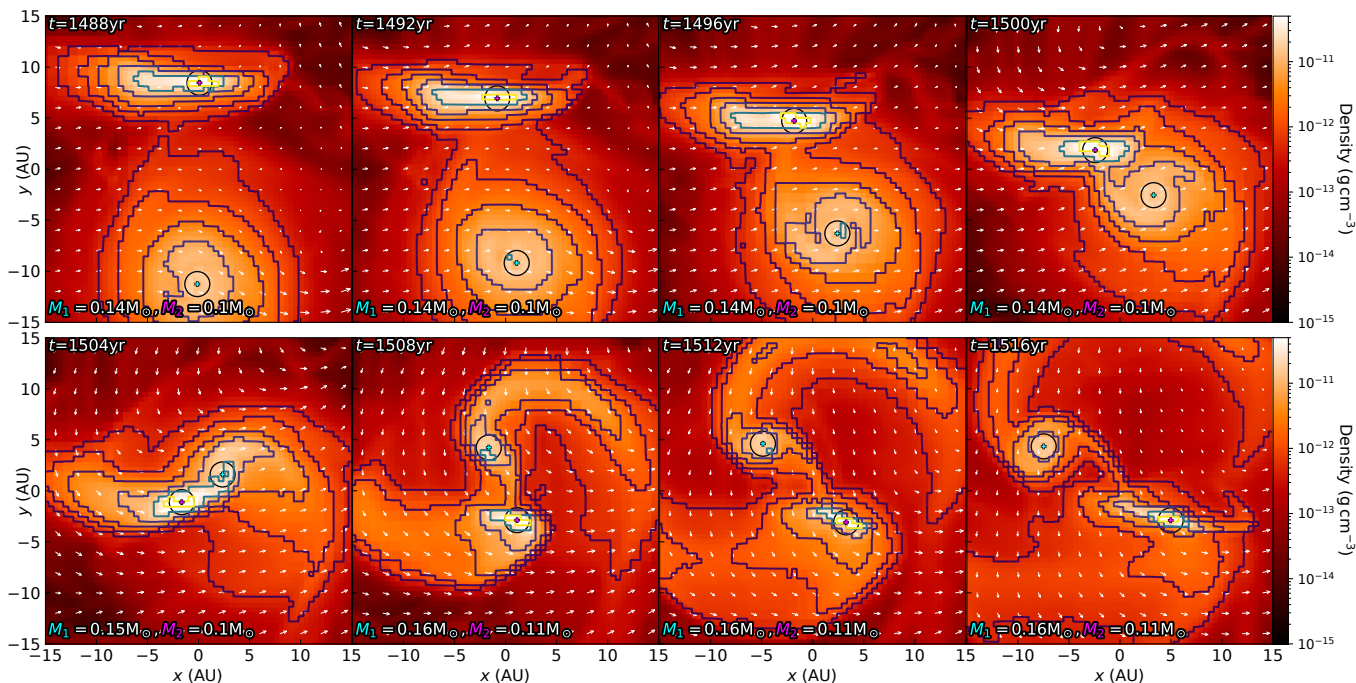ed. From looking at the evolution of the orbital angular momentum, we observe the accretion event begins before periastron when the spiral wave is excited. We also observe the orbital angular momentum of the binary components increases due to the exchange between the binary and circumstellar discs before periastron. The orbital angular momentum then decreases after periastron, because of the ejection of gas. From this close analysis of an accretion burst, we find that an accretion event is ultimately triggered by angular momentum moving from the circumstellar discs to the binary orbit, exciting the spiral wave.

Conclusions

We quantified how eccentricity influences the strength of accretion over a binary orbit, what physical mechanism triggers accretion events.

Dependence of episodic accretion on eccentricity: We find that orbital phase-correlated episodic accretion occurs in binaries of eccentricity $e > 0.2$. For *T1*, we find that episodic accretion peaks for moderate eccentricity ($0.3 < e < 0.7$). *T2* shows a general linear trend of weak episodic accretion at low eccentricity to strong accretion at high eccentricity. These varying results imply

that eccentricity alone does not determine the strength of episodic accretion.

Mechanism triggering accretion events: Based on high-resolution simulations, we determine that it is primarily torques between the circumstellar disc and the companion that triggers an accretion event. Observations of spiral arms in protoplanetary discs show similar structures to those seen in our simulations [6].

Overall we find that episodic accretion can be seen in binaries with eccentricity > 0.2, and the shape of episodic accretion is in good agreement with that found in observations of short-period binaries (this is investigated in [4]). We suggest that signs of episodic accretion should be observable in long-period binaries.

Acknowledgements

References

[1] Larson, R. 1969, MNRAS, 145, 271
[2] Bate, M. 1998, ApJL, 508, L95
[3] Korntreff, C., et al. 2012 A&A, 543, A126
[4] Kuruwita, R. L., et al. 2020, A&A 641, A59
[5] Fryxell, B., et al. 2000 ApJSS, 131, 273
[6] Rosotti, G. P., et al. 2019 MNRAS, 491, 1335

Short CV

2014: Master in Astronomy & Astrophysics, Macquarie University, Sydney, Australia
2019: PhD in Astronomy, Australian National University, Canberra, Australia
2021: INTERACTIONS Fellow, University of Copenhagen, Copenhagen, Denmark

Photoionized Herbig-Haro objects in the Orion Nebula through deep high-spectral resolution spectroscopy

José Eduardo Méndez-Delgado

Instituto de Astrofísica de Canarias (IAC), E-38205 La Laguna, Spain

Herbig-Haro objects (HHs), named for their discoverers, George Herbig and Guillermo Haro, are small nebular regions originated from gas ejections from newly formed stars. Since the early 50s, many of these objects have been observed in neutral environments where their optical emission stands out from the surrounding gas. In these cases, the optical spectrum is dominated by shock heating, a process that excites and ionises the gas using the kinetic energy of the jet. This heating is followed by a cooling of the gas through the emission of Recombination Lines (RLs) and Collisional Excited Lines (CELs). HHs are also present in the nebulae where stars are born, that is, HII regions. In these cases, the intense radiation field emitted by the O- and B-type stars is capable of photoionising the surrounding gas, which reaches an equilibrium set by the global physical conditions of electron density and temperature (n_e, T_e).

Figure 1: Image of the central area of the Orion Nebula taken with the WFPC2 of the HST [1] using 3 filters: F502N, F658N, and F656N for colors red, green, and blue, respectively. The three most prominent bow shocks of the Herbig-Haro object HH529 are indicated. Image taken from [3], indicating the slit position of the spectroscopic observations.

The Orion Nebula, the brightest HII region in the night sky, is home to a significant number of HHs. Several of these objects are photoionised by the intense radiation field of the Orion Trapezium stars, particularly from the θ^1 Ori C star. This radiation dominates over the shock-heating and fix a photoionisation equilibrium in these HHs, so their emission spectra become analogous to those of small-scale HII regions.

The great variety of morphologies, velocities and distances with respect to θ^1 Ori C covered by these HHs allows us to study the chemical composition of the Orion Nebula, which is representative of the Solar neighbourhood, under different conditions of density and degree of ionisation. In addition, it allows us to investigate the impact that shocks have on the destruction of dust grains. Through deep observations of these HHs with high spectral resolution spectroscopy, we can separate their Doppler-shifted emission from the optical radiation of the Orion Nebula and study them individually.

HH529II-III

HH529 is an HH object located in the central zone of the Orion Nebula as is shown in Figure 1. Its three most prominent bow shocks, named HH529I, HH529II, and HH529III, indicate its eastward propagation. We [3] analysed HH529II and HH529III through deep optical spectra taken with the UVES spectrograph at the Very Large Telescope (VLT) and 20 years of images from the Hubble Space Telescope (HST).

The emission spectra of these objects indicate that they are composed of fully photoionised gas, mainly from intermediate and high ionisation species (ions with ionisation potentials, IPs > 25 eV). The compression of the gas in the bow shocks of HH529 increases their electron density, reaching values of $n_e \sim 30\,000$ cm^{-3} in HH529III, up to a factor 5 higher than the density of the Orion Nebula in the same line of sight. Due to their high degree of ionisation, it is possible to estimate the total abundances of He, C, O, Cl, Ar and Fe without Ionisation Correction Factors (ICFs), which are relationships based on photoionisation models used to consider the contribution of non-observed ions in the optical range to the total abundance.

Multiple RLs from heavy elements as O^{2+}, C^{2+} or Ne^{2+} were detected in HH529II and HH529III, which are several orders of magnitude weaker than the CELs of the same ions. This allowed to explore the Abundance Discrepancy problem (AD problem), which is the systematic difference between the ionic abundances obtained with the intensity of RLs and CELs. The AD problem may indicate the existence of physical phenomena not well understood such as temperature inhomogeneities, fluorescent excitation processes, chemical inhomogeneities, etc. The different temperature determinations available in HH529II and HH529III suggests that the possible ex-
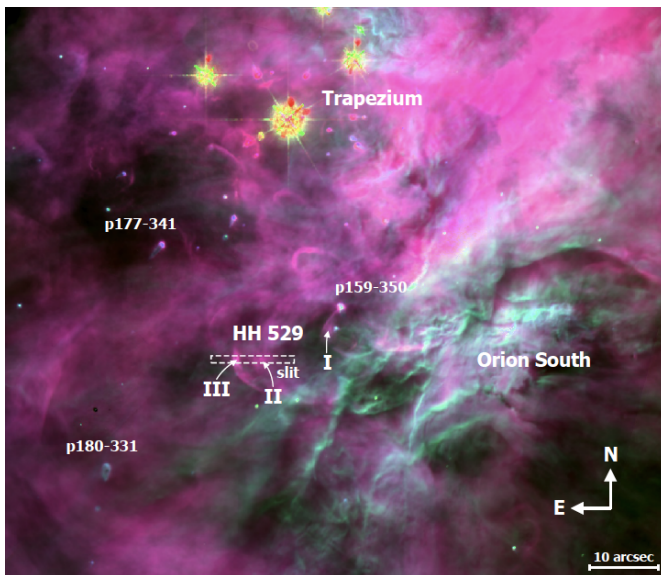
istence of small temperature fluctuations is not enough to explain the observed Abundance Discrepancy Factor (ADF) between the O^{2+} and Ne^{2+} ionic determinations based on RLs and CELs.

A slight overabundance of the heavy elements O, Ar, Ne, S, and Cl (~ 0.12 dex), with a possible origin in inclusions of H-deficient gas, is found in HH529. In addition, there is direct evidence that the shock between HH529 and the Orion Nebula is able to destroy dust grains with Fe content. HH529II shows and abundance of Fe by a factor ~ 2.35 higher than what is found in the Orion Nebula in the same line of sight. The efficiency of the dust destruction may be related to the velocity propagation of HH529, which is ~ -70 kms^{-1} in the reference frame of the Orion Molecular Cloud (OMC), propagating at an angle of $\sim 58°$ with respect to the plane of the sky [3].

HH204
HH204 is an HH object located in the southeast of the Orion Bar, close to θ^2 Ori A in the plane of the sky, as shown in Figure 2. For HH204, we [4] used the same kind of observations as in HH529II-III.
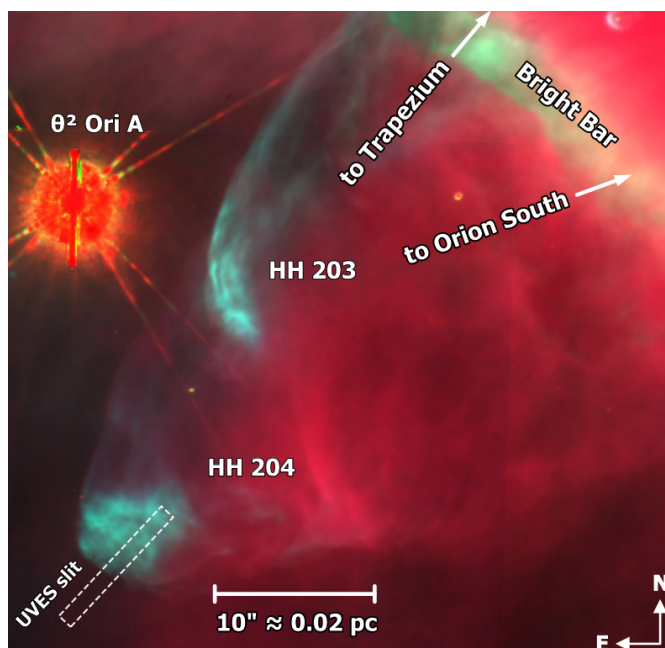

Figure 2: Image of the Orion Nebula in the southeast of the Orion bar taken with the HST WFPC2 [2] using the same color scale as Figure 1. Image taken from [4], indicating the location of the UVES spectrograph slit.

In contrast to the ionisation conditions of HH529II-III, HH204 is mainly composed of low- and intermediate ionisation species (IPs<25 eV) with strong emissions from neutral elements such as O^0 or N^0. This allowed to estimate the abundances of O, N, S, Cl, Fe and Ni without ICF. In addition, it was shown that Fe and Ni have similar depletion and ionisation patterns, presenting abundances a factor 3.5 higher than in the Orion Nebula. This supports the hypothesis that the velocity of propagation of the jet is a key factor in the degree of dust destruction, since HH204 propagates at ~ -90 km s^{-1}, faster than HH529II and HH529III, with a propagation angle of $\sim 32°$ with respect to the plane of the sky.

In this object, the abundance of O presents zero ADF, that is, the abundances obtained with RLs and CELs match. Some clues found in HH204 that can help to solve the AD problem in ionised nebulae are the following: (i) there are no relevant temperature fluctuations in HH204, (ii) the effects of starlight fluorescence in the OI RLs are plausibly negligible for this HH and (iii) no errors in physical conditions or chemical inhomogeneities are expected in HH204.

Finally, we [4] showed that some density diagnostics, commonly used in the study of the interstellar medium –such as [SII] $I(\lambda6716)/I(\lambda6731)$– can underestimate the true density in an integrated spectrum when a high-density inclusion (such as an HH object) is present. This could lead to an overestimation of the true gas temperature, implying wrong estimates of chemical abundances.

Future work
Through the analysis of data of further HHs (such as HH514, HH203, HH202, HH625 and HH518) we seek to explore the relationships between the level of dust destruction, degree of ionisation of the gas, velocity of the jet propagation and distance from the ionizing source. We also seek to determine more precisely the actual chemical composition of the solar neighborhood and constrain the AD problem.

References

[1] Bally, J., et al. 1998, AJ, 116, 293

[2] O'dell, C. R., & Wong, K. 1996, AJ, 111, 846

[3] Méndez-Delgado, J. E., et al. 2021, MNRAS, 502, 1703

[4] Méndez-Delgado, J. E., et al. 2021, ApJ, 918, 27

Short CV

2017: BSc in Physics, Universidad Nacional Autónoma de México, Mexico
2019: MSc in Astrophysics, Universidad de La Laguna, Spain
2018–2022: PhD in Astrophysics, Universidad de La Laguna and Instituto de Astrofísica de Canarias, Spain

Tracing cosmic magnetic fields using molecules

Boy Lankhaar

Department of Space, Earth and Environment, Chalmers University of Technology, Onsala Space Observatory, 439 92 Onsala, Sweden

The Universe is permeated by magnetic fields, that often play an important role in the dynamics of astrophysical processes [1]. Observations of spiral galaxies generally reveal magnetic field strengths on the order of $\sim 10~\mu G$ [2], while molecular clouds in star-forming regions are associated with dynamically important magnetic fields [1]. All main-sequence stars are thought to host a magnetic field, which is likely boosted through a stellar dynamo [3], and inherited as the star evolves away from the main-sequence as an evolved star [4]. The magnetic field in all these phases will affect the dynamics of the associated astrophysical processes. To characterize the effects, one requires information on both the magnetic field strength, and morphology.

With the advent of (sub)millimeter interferometers, it has been possible to analyze the (polarized) emission of astrophysical sources at sub-arcsecond resolution. This has opened up the possibility of studying the resolved structure of many astrophysical sources. Molecular line polarization traces magnetic fields at these scales most robustly. Here, we discuss different techniques of magnetic field detection with molecules. We discuss mapping of magnetic field morphology with (sub-)millimeter interferometry techniques using (i) the Goldreich-Kylafis effect [5] and collisional polarization [6], to map the magnetic field morphology and (ii) through the Zeeman effect of paramagnetic molecules, tracing the magnetic field strength. We also discuss using masers (Microwave Amplification of Stimulated Emission of Radiation) to trace the magnetic field strength and morphology towards high-mass star-forming regions.

Line polarization: PORTAL & collisional polarization

Linear polarization in molecular lines is found in non-LTE excited molecular species, that are under the influence of an anisotropic radiation field [7]. Because the magnetic precession rate of non-paramagnetic molecules is on the order of $\sim \mathrm{s}^{-1}/\mathrm{mG}$, while other aligning interactions typically occur at rates of $\lesssim 10^{-4}~\mathrm{s}^{-1}$, molecules almost always orient themselves to the magnetic field under astrophysical conditions and their polarization direction is related to the magnetic field direction. Molecules therefore provide for a very robust magnetic field tracer.

However, to properly model the polarization of molecular lines, comprehensive radiative transfer modeling, that takes into account the intricate density, velocity and temperature structures of astrophysical sources, is vital. Line radiative transfer modeling tools, such as LIME (LIne Modeling Engine, [8]) have been developed to perform such comprehensive modeling for three-dimensional astrophysical structures. In [7], it was shown how to extend a three-dimensional line radiative transfer with the capability to model line polarization radiative transfer, for arbitrary magnetic field configurations.

The polarized line radiative transfer modeling tool is called PORTAL (POlarized Radiative Transfer Adapted to Lines). The source code of PORTAL is available on GitHub at `https://github.com/blankhaar/PORTAL`. PORTAL allows for the rigorous prediction and modeling of line polarization signals from arbitrary astrophysical regions with arbitrary magnetic field configurations.
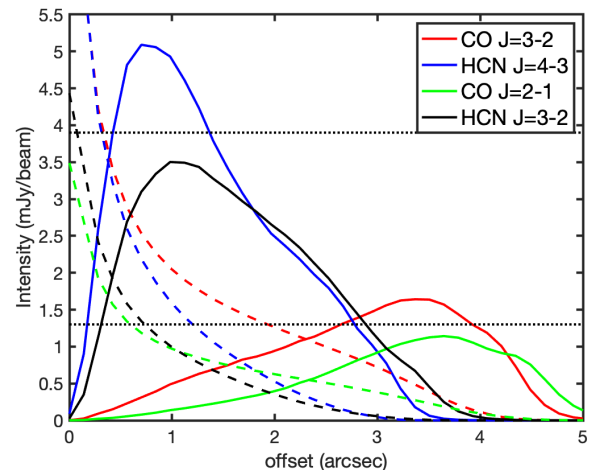

Figure 1: Plots of the azimuthally averaged polarized emission of transitions of HCN and CO from a face-on axisymmetric disk of mass $10~M_J$. We plot the $J = 3 \rightarrow 2$ and $J = 2 \rightarrow 1$ transitions of CO and the $J = 4 \rightarrow 3$ and $J = 3 \rightarrow 2$ transitions of HCN at systemic velocity. We assume a source of distance 60 pc and a beam size (FWHM) of $0.7" \times 0.7"$. The polarized emission is computed for a toroidal magnetic field configuration. We also plot the total emission divided by 1000 associated with each transition in a dotted line of the same color to represent the (current) ALMA sensitivity limit of the detectability of linear polarization. We also added a dotted line, representing $1\times$ and $3\times$ a typical ALMA sensitivity of 1.3 mJy/beam. Taken from [9].

Lines may also polarize through collisional polarization if two collision partners interact through oriented collisions [10]. Recently, we pointed out [6] that oriented collisions in astrophysical settings may be the product of ambipolar diffusion. Ambipolar diffusion is generally thought to be one of the most important regulators of star formation, and it occurs in a magnetized and partially ionized plasma, where the neutral and ionized medium are collisionally coupled [11]. In star-forming regions or clouds, a molecular ion such as HCO^+ has as its main collision partner the neutral H_2. Collisions between these molecules have a preferred direction when ambipolar diffusion is active. In [6], we modeled the collision-induced alignment of HCO^+ and the associated polarization of its spectral lines, under the influence of ambipolar diffusion. It is predicted that detectable polarization emerges in the C-shock associated with the accretion onto young stellar objects [12] or generally in the colder phase of the ISM.

Detecting collisional polarization would be the first direct observation of ambipolar diffusion.

Line polarization opportunities

The formation of solar type stars is accompanied by a protoplanetary disk. Magnetic fields are fundamental to the accretion dynamics of protoplanetary disks and they likely affect planet formation. Zeeman measurements of paramagnetic molecules have been able to put stringent constraints on the magnetic field of protoplanetary disks [13, 14], but have yet to make a direct detection of the global magnetic field in these objects. In Figure 1, we show PORTAL modeling of the polarization signal from the ALMA band 6 and 7 CO and HCN transitions that are excited in a protoplanetary disk such as the one around TW Hya. PORTAL modeling predicts detectable polarization signals for the band 7 transition of HCN, that trace the magnetic field structure around 60 au from the central protostar. Polarization signals of CO are estimated to be weak, which is in line with earlier ALMA line polarization observations [15].

The loss of mass in evolved stars forms a circumstellar envelope around these objects. Molecules form in the envelope and the dust that is produced in the extended atmosphere, absorbs the radiation from the central stellar objects, driving an outward wind. Magnetic fields possibly play an important role in the wind-launching, but are very hard to characterize in these objects. Line polarization in these regions are expected to be strong, due to the strong directional radiative interactions of the stellar radiation field with molecular vibrational transitions [7]. Special care has to be taken here to characterize the aligning interactions (magnetic vs. radiative), but comprehensive and resolved high-resolution line observations may provide important constraints on the magnetic field morphology of these objects.

Some galaxies, such as NGC 4418, host a CON (Compact Obscured Nucleus). CONs are characteristic of a highly dynamical evolutionary stage, associated with a large inflow and a collimated outflow of gas. In turn, the CON is uniquely characterized by very bright vibrationally excited emission, in particular the vibrational transitions of HCN (HCN-VIB). HCN-VIB is pumped by hot ($T > 100K$) dust in the inner ($r < 15 - 75$ pc) and opaque ($N_{H_2} \geq 10^{24}$ cm^{-2}) regions centered on the nuclei. PORTAL simulations show that the vibrationally excited transitions are prone to polarize to very high degrees, because of the strong radiative vibrational excitation in the war inner regions of the CON. The predicted polarization degrees are observable with ALMA. Such observations would constitute the first direct constraints on the magneto-hydrodynamic (MHD) dynamics of the outflow-launching region of a CON.

The simplest example of an anisotropic radiation is field is the astrophysical maser, which is (almost) one-dimensional due to maser beaming [16]. They are therefore also prototypical examples of radiative transfer systems wherein polarized emission arises. Masers occur under special conditions towards many interesting astrophysical objects. We highlight here methanol masers; which occur exclusively towards high-mass star forming regions. Recent theoretical efforts were able to characterize the Zeeman effect in methanol [17], which now opens up the possibility of using this maser as a probe for the magnetic field strength towards massive protostars. Recent developments in the theory of the polarized radiative transfer of masers will allow for the proper interpretation of coming maser polarization observations [18, 19].

References

[1] Crutcher, R.M. 2012, Ann.Rev. A&A, 50, 29-63
[2] Beck, R. 2016, A&A Rev., 24, 4
[3] Parker, E.N. 1955, ApJ, 122, 293
[4] Vlemmings, W.H.T. 2019, Proc. IAU, 343, 14
[5] Goldreich, P., & Kylafis, N. 1981, ApJL, 243, L75
[6] Lankhaar, B., & Vlemmings, W. 2020, A&A, 638, L7
[7] Lankhaar, B., & Vlemmings, W. 2020, A&A, 636, A14
[8] Brinch, C., & Hogherheijde, M. 2010, A&A, 523, A25
[9] Lankhaar, B., & Vlemmings, W. 2021, A&A, subm.
[10] Fiedrich, B., & Herschbach, D.R. 1991, Nature, 353, 412
[11] Mestel, L., & Spitzer, L. 1956, MNRAS, 116, 503
[12] Li, Z., et al. 2011, ApJ, 738, 180
[13] Vlemmings, W. H. T., et al. 2019, A&A, 624, L7
[14] Harrison, R.E., et al. 2021, ApJ, 908, 141
[15] Stephens, Ian W, et al. 2020, ApJ, 901, 71
[16] Elitzur, M. 1992, Ann.Rev. A&A, 30, 75
[17] Lankhaar, B., et al. 2018, Nature Astronomy, 2, 145
[18] Lankhaar, B., & Vlemmings, W. 2019, A&A, 628, A14
[19] Dall'Olio, D., et al. 2020, A&A, 644, A122

Short CV

2015:	MSc in Theoretical Chemistry, Radboud University, Nijmegen, The Netherlands
2021:	PhD in Astronomy, Chalmers University of Technology, Gothenburg, Sweden
2021–present:	Postdoc, Chalmers University of Technology, Gothenburg, Sweden
2021–present:	Guest Postdoc, Leiden Observatory, Leiden, The Netherlands

Hotter than hell:
understanding highly-irradiated worlds through transmission spectroscopy

Julia V. Seidel

University of Geneva, chemin des Maillettes 51, 1290 Versoix, Switzerland

Since the discovery of an exoplanet around a sun-like star in the mid-nineties [1], the field of exoplanet science has made large strides towards a better understanding of planetary atmospheres. First observations from space [2], which were then later confirmed from the ground [3], have since been joined by a plethora of observations of these far away atmospheres. One of the most puzzling results from this early phase of discoveries are hot and ultra hot Jupiters, the latter being Jupiter-sized planets with temperatures above 2000 K. These worlds have no equivalent in our Solar System and provide insights into the most extreme conditions atmospheres can be placed under.

Transmission spectroscopy

To study these enigmatic highly irradiated atmospheres, one can utilise the so called transmission spectroscopy method, where the planet is observed while it occults part of the starlight captured by the observer. During this occultation part of the light is not blocked but interacts with the atmosphere of the exoplanet as it traverses. Depending on which particles the light encounters in the atmosphere, it is then absorbed, changing the apparent radius of the planet depending on the absorption wavelength. The detection of this atmospheric absorption gives us information about the composition of the atmosphere, but the depth of the absorption line is also directly proportional to the absorption height in the atmosphere (see Figure 1). This allows us to create a vertical profile of the observed exoplanet atmosphere.
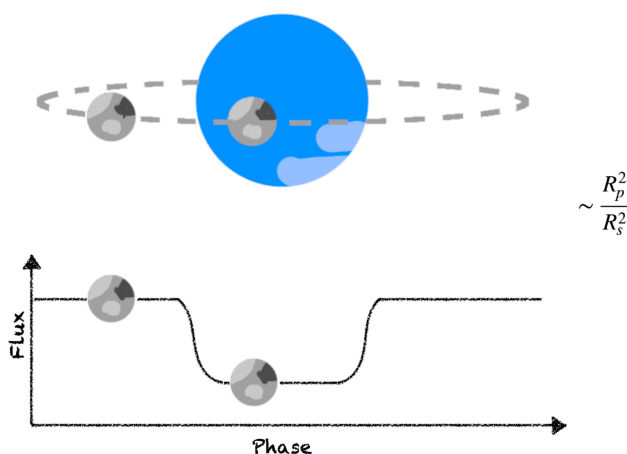

$$\sim \frac{R_p^2}{R_s^2}$$

Figure 1: Depiction of an exoplanet transit in front of a host star. The lower panel shows the absorption as a function of time, called a lightcurve.

Studying winds in ultra hot Jupiters

One of the various subfields of interest to paint a more coherent picture of exoplanet atmospheres is the study of their wind profiles and, in the case of highly irradiated planets such as hot Jupiters, their mass loss. From observations of phase curves in the infra-red and subsequent modelling with global circulation models (so called GCMs, see [4]), we know that most giant gas planets have a zonal structure up to the millibar level in pressure with winds either super-rotating faster than the planet itself or, for tidally locked hot Jupiters, a day to night side wind, blowing from the hot, constantly irradiated day side to the cooler night side (see, e.g. [5] for HD189733 b).

On the other hand, from observations of the main constituents of hot Jupiter atmospheres, Hydrogen and Helium, in the ultra violet we can study the outermost rim of these atmospheres. For example [6] studied the hot Jupiter HD189733 b with the Hubble Space Telescope to observe its Lyman-α absorption and found that even long after the planet had already left the stellar disk it had occulted before, the atmosphere continued to obscure part of the star. This result led to the conclusion that the exoplanet is blasted with stellar irradiation and the outer layer of its atmosphere (at the nanobar level in pressure) evaporates material into space, dragging a comet-like tail behind the planet.

But how are these horizontal winds at the millibar level connected to the mass loss in the outermost parts of the atmosphere? This question is answered for the specific case of the ultra hot Jupiter WASP-76 b in my work on the connecting layers between the above described pressure regimes, which we will call here the intermediate atmosphere.

The intermediate atmosphere and radial winds

Transmission spectroscopy has one compelling advantage when conducted from the ground: the spectral absorption lines from the atmosphere can be resolved in wavelength, so called high-resolution transmission spectroscopy. And one of the best targets for this kind of observation is the sodium doublet in the yellow visible wavelength range. Due to its large oscillator strength, this resonant doublet produces a large absorption feature even if only a small fraction of sodium is present in the atmosphere. In consequence, the shape of the sodium absorption feature traces through the entire atmosphere of the exoplanet up the thermosphere, thus bridging the two wind regimes discussed before.

In [7], this knowledge of the line shape was exploited via a nested sampling retrieval algorithm that compared
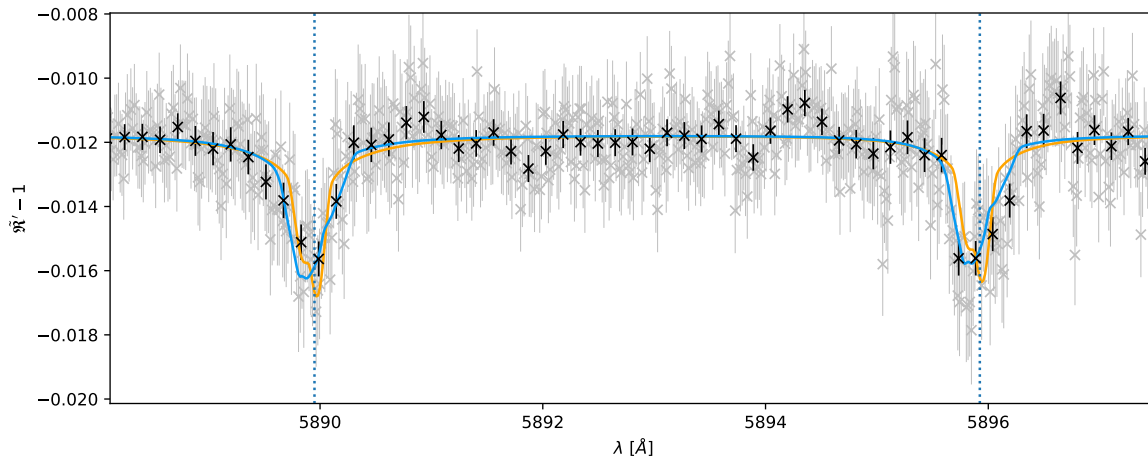
Figure 2: Figure 5 from Seidel [9]. The combined data of three HARPS and two ESPRESSO transits of WASP-76 b is shown with the best fit model in blue and a model solely with lower atmospheric day to night side wind in orange.

a theoretical line shape broadened via the Doppler-effect from different atmospheric wind patterns with the observed line shape for the hot Jupiter HD189733 b. This code is called MERC in the following. Already in this work, we found that the line shape can only be explained by a radial, vertical wind. However, some simplifications were made to save computing time, meaning that the wind speed had to be considered an upper limit.

In the follow up work presented in the Hypatia series, these simplifications were removed and a latitude dependence of the winds introduced, so that the poles and the equator had physically sound differences in wind speed. Additionally, planetary rotation was accounted for. This update of MERC was then applied to the ultra hot Jupiter WASP-76 b (see Figure 2), and revealed a day to night side wind of roughly 5 kms^{-1} in the lower atmosphere at the millibar level and at higher pressures. This observational retrieval result is compatible with the same wind pattern and speed found for this planet in [8], where iron was traced in time during the transit. In the intermediate atmosphere the same radial, vertical wind connects the zonal winds in the lower atmosphere with the expanding atmosphere in the outer layers that was already found for HD189733 b. This vertical wind is likely driven by the strong irradiation which is also responsible for the upper atmospheric mass loss. An additional hypothesis is the possible interaction of ions in the zonal winds with the strong magnetic field of these ultra hot planets. These findings were subsequently published in [9].

Additional studies of other ultra hot Jupiters are necessary to verify the origin and strength of this wind in WASP-76 b and to understand if this vertical wind is a common feature in highly irradiated atmospheres.

References
[1] Mayor, M., & Queloz, D. 1995, Nature, 378, 6555
[2] Charbonneau, D., et al. 2002, ApJ, 568, 1
[3] Redfield, S., et al. 2008, ApJL, 673, 1
[4] Showman, A., et al. 2008, ApJ, 682, 1
[5] Steinrueck, M., et al. 2019, ApJ, 880, 1
[6] Bourrier, V., et al. 2020, A&A, 557, A124
[7] Seidel, J. V., et al. 2020, A&A, 633, A86
[8] Ehrenreich, D., et al. 2020, Nature, 580, 7805
[9] Seidel, J. V., et al. 2021, A&A, 653, A73

Short CV

2015: BSc in Physics, TU Darmstadt, Germany
2017: MSc (ext. Research) in Physics with Distinction, Imperial College London, UK
2021: PhD in Astronomy and Astrophysics, University of Geneva, Switzerland
2021: PostDoc (3 months), University of Geneva, Switzerland
2021: ESO Fellow, Santiago de Chile, Chile

Atmospheric Dispersion Corrector:
from design phase to on-sky commissioning

Bachar Wehbe

Instituto de Astrofísica e Ciências do Espaço, Universidade de Lisboa, Lisboa - Portugal

Departamento de Física, Faculdade de Ciências, Universidade de Lisboa, Lisboa - Portugal

Astronomical observations with ground-based telescopes are affected by differential atmospheric dispersion, a consequence of the wavelength-dependent index of refraction of the atmosphere. The problem of atmospheric dispersion is particularly serious for high-resolution spectrographs aiming at sub-pixel radial velocity (RV) precision. In order to detect Earth-like planets orbiting Sun-like stars, an RV precision of around 10 cm s^{-1} must be achieved. With the objective of developing high-resolution spectrographs that can reach such a RV precision [1], a correction of atmospheric dispersion variation down to this level of positioning accuracy must be included. An Atmospheric Dispersion Corrector (ADC) is thus mandatory [2].

What is an ADC?

An ADC, is a prism, or a set of prisms, that is used to counteract the effect of atmospheric dispersion. As we know, a prism produces refraction. An ADC is supposed to produce an equal amount of dispersion as the atmosphere, and in an opposite direction. The design of an ADC can vary from a simple prism, to a complicated counter-rotating prism made of two or more prisms glued together. One of the most common types of ADC, is the rotating atmospheric dispersion corrector. The ADC can perform two rotations: i) when the two prisms rotate together to define the ADC dispersion direction that should oppose that of the sky; ii) when the two prisms counter-rotate to define the ADC dispersion amount that should be equal to that of the sky (Figure 1).
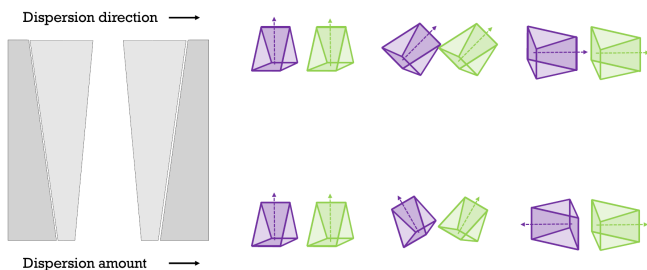

Figure 1: Left: schematic of a rotating ADC; right: schema of the different rotations of an ADC.

How can we design/model an ADC?

As mentioned before, an ADC is supposed to create a dispersion with an equal amount, and opposite direction to that of the sky in order to cancel it. The design of an ADC is usually based on atmospheric dispersion models, that up to our knowledge, were never tested on-sky. With the increase of the requirements demands on the ADC, with residuals at the level of few tens of milli-arcseconds (mas), it is important to re-visit how an ADC is modeled.

For example, the difference between the two most common models, Filippenko [3] and Zemax [4], is higher than the required residuals. Therefore we developed a method to measure on-sky the atmospheric dispersion to better characterize the different models [5, 6].

The method is based on the use of cross-dispersion spectrographs to determine the position of the centroid of the spatial profile at each wavelength of each spectral order. The method is validated using cross-dispersed spectroscopic data acquired with the slit spectrograph UVES. The accuracy of the method is 18 mas. At this level, we are able to compare and characterize the different atmospheric dispersion models of interest. For better future ADC designs, we recommend to avoid the Zemax model, and in particular in the blue range of the spectra, when expecting residuals at the level of few tens of mas.
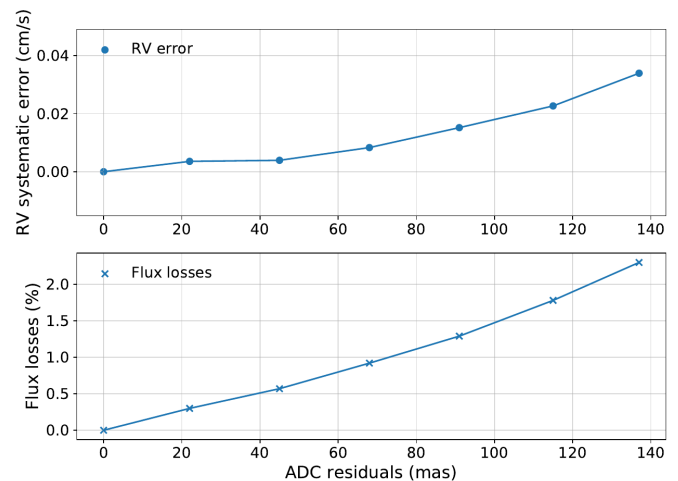

Figure 2: Top: expected RV error due to ADC residuals; bottom: expected flux losses at 380 nm due to ADC residuals.

How can we define ADC residuals requirements?

When designing an ADC, an important factor that plays a role is the requirement set, in particular the ADC residuals (remaining dispersion after sky correction). These residuals errors can affect the position of the target as perceived on the sky and its flux distribution. This effect will affect the results of astronomical observations. Therefore, it was important that we test the effect of atmospheric dispersion on astronomical observations in general, and in particular on RV precision degradation and flux losses. Our scientific objective is to quantify the amount of residuals needed to fulfil the requirements set on an ADC during the design phase [7]. We found that up to a dispersion of 100 mas, the effect on the RV is negligible. However, on the flux losses, such a dispersion

can create a loss of $\sim$ 2% at 380 nm, a significant value when efficiency is critical. The requirements set on ADC residuals should take into consideration the atmospheric conditions where the ADC will function, and also all the aspects related with not only the RV precision requirements but also the guiding camera used, the tolerances on the flux loss, and the different melt data of the chosen glasses. Figure 2 summarise the relation between ADC residuals and RV errors as well as flux losses.

How can we validate an ADC on-sky?

Another important step in the lifetime of an ADC, after setting its requirements and designing it, is to be able to validate it on-sky. As mentioned before, the rotating ADC can perform two rotations, that should be perfectly aligned with the sky dispersion. Insufficient or wrong correction of the atmospheric dispersion produces a spectrally elongated shape instead of a circular white one for the observed target. The commissioning tests of ADCs with on-sky observations are not an easy task. In fact, the residual dispersion is expected to be of a few tens of mas, with the object for a seeing limited telescope being almost 1 arcsec. A procedure was developed [8], based on ellipse fitting of several cuts from the guiding camera images, to determine the levels of oblongness in an object image caused by atmospheric dispersion. The characterisation of the data allows for the validation of the ADC alignment by determining the dispersion direction and minimizing the ellipticity. The procedure was tested and demonstrated using simulated data that mimics the expected images using real sky dispersion models and real sensor characteristics. The accuracy of the method is highly dependent on the observational conditions and on the ratio between expected elongation (dispersion) and image size, but it is expected that the method can be more sensitive than traditional ADC on-sky alignment methods.

References

[1] Fischer, D. A., et al. 2016, PASP, 128, 066001
[2] Avila, G., et al. 1997, SPIE 2871, 1135
[3] Filippenko, A. V. 1982, PASP, 94, 715
[4] Hohenkerk, C. Y., & Sinclair A. T. 1985, NAO Tech. Note No. 63
[5] Wehbe, B., et al. 2020, MNRAS, 499, 183
[6] Wehbe, B., et al. 2021, MNRAS, 503, 3818
[7] Wehbe, B., et al. 2020, MNRAS, 491, 3515
[8] Cabral, A., & Wehbe, B., 2021, J. of Astronomical Telescopes, Instruments, and Systems, 7(3), 035003

Short CV

2015: Master in Astrophysics, University Saint Joseph (USJ), Lebanon
2021: PhD in Astronomy, Faculty of Sciences University of Porto (FCUP), Institute of Astrophysics and Space Sciences (IA), Porto, Portugal
2021: Postdoc Fellow, IA, Portugal

Reach New Heights

Fellowships in Germany or Chile

Develop your scientific profile
Become an independent researcher
Prepare for future responsibilities

eso.org/fellowship

STELLAR EVOLUTION

Can uncertainties in the evolution of massive stars explain properties of gravitational wave progenitors?

Poojan Agrawal

Swinburne University of Technology, Hawthorn, VIC 3122, Australia

Stars more massive than $9\,M_\odot$ are known as massive stars. These stars are responsible for the chemical enrichment of the interstellar medium and are progenitors of many astrophysical phenomena such as supernovae, gamma-ray bursts and compact binary mergers. Recent observations such as the detection of gravitational waves from the merger of their remnants, neutron stars and black holes, have renewed interest in exploring the lives of these stars.

However, the evolution of these massive stars is riddled with uncertainties. These stars are born less often and spend only a few million years burning nuclear fuel, hence it is difficult to get observational constraints on their evolution. Therefore, several physical properties such as the mass-loss rates, nuclear reaction rates, and internal mixing processes remain uncertain for these stars. As a result, modellers have to make certain assumptions about these parameters while modelling the evolution of these stars with one-dimensional (1D) stellar evolution codes.

Numerical instabilities in the envelopes of massive stars

The evolution of stars more massive than $40\,M_\odot$ is further complicated by the presence of sub-surface opacity bumps in their outer layers. Such massive stars are extremely bright with luminosities close to the critical Eddington luminosity required to balance outward radiation pressure with the inward gravitational pressure. In the low-density envelope of these stars, convection, as given by the mixing length theory [1], is inefficient, and the presence of elemental opacity bumps can cause the radiative luminosity to exceed the Eddington luminosity.

To maintain hydrostatic equilibrium, the density and gas pressure, which normally decrease with radius, increase locally in sub-surface layers, forming density and gas pressure inversions. These density inversions present a challenge while modelling the evolution of massive stars. The time-steps of the simulation become exceedingly small, and it becomes computationally challenging to model the further evolution of the star [2]. Therefore, modellers have to employ certain techniques, such as enhancing mass-loss rates to remove problematic outer layers or increasing convective efficiency by setting the mixing length proportional to the density scale height, to push forward the evolution of massive stars beyond these numerical instabilities.

Comparing massive star models from various codes

The combination of the different techniques to overcome numerical instabilities and the various physical uncertainties in the evolution of massive stars can result in large differences in the stellar models between different codes.

To determine the impact of these physical and numerical uncertainties on the evolutionary properties of massive stars, we compared non-rotating models of stars with initial masses between 9–$200\,M_\odot$, at near-solar metallicity from five different codes: models from the PAdova and TRieste Stellar Evolution Code (PARSEC; [3]), MESA Isochrones and Stellar Tracks (MIST; [4]) from the Modules for Experiments in Stellar Astrophysics (MESA; [5]), models [6] from the Geneva code [7], models from the Binary Population and Spectral Synthesis (BPASS; [8]), and the Bonn Optimized Stellar Tracks (BoOST; [9]) from the 'Bonn' Code.
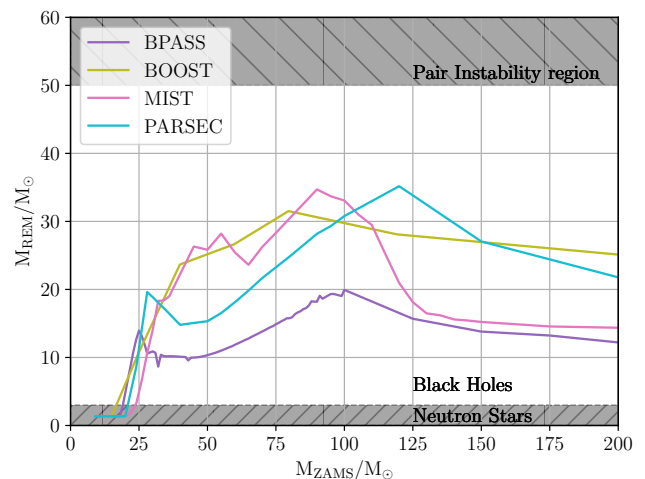

Figure 1: Mass of the stellar remnant versus the initial mass of the star as predicted by various stellar models.

We find that the evolutionary properties of massive stars can vary significantly between these models. For example, Figure 1 shows the remnant mass of the star as a function of its initial mass, as predicted by the different sets of stellar models. The remnant mass has been calculated using the prescription from [10], based on the final core mass and the final total mass of the star. Geneva models do not provide core masses and therefore they have not been included in this comparison. As shown in the figure, the remnant mass predictions can differ by $20\,M_\odot$ between different stellar models. Moreover, while the maximum black hole mass predicted by BoOST, MIST and PARSEC models at this metallicity is more than $30\,M_\odot$, the most massive black hole predicted by BPASS models is just $20\,M_\odot$. These differences are important for various studies including predictions of gravitational wave properties from compact binary mergers. However, currently none of these models can be established as better or worse than the others.

Population Synthesis and METISSE

To test the impact of the various uncertainties in the evolution of massive stars on the properties of gravitational wave progenitors, one needs population synthesis codes – codes that can models populations of stars and the various interactions between them. However, many of these codes rely on using fitting formulae for calculating evolutionary parameters of individual stars. These formulae are derived using polynomial fits to a set of 1D stellar models, and need to be recalculated for different sets of stellar models. However, defining these formulae is an arduous task. To address this, we have developed the METhod of Interpolation for Single Star Evolution (METISSE; [11]) that uses interpolation within a grid of pre-computed 1D stellar models to calculate stellar parameters. It is an improvement over the commonly used Single Star Evolution (SSE; [12]) fitting formulae, as the use of interpolation allows the user to easily use different sets of 1D stellar models, computed with different input parameters.
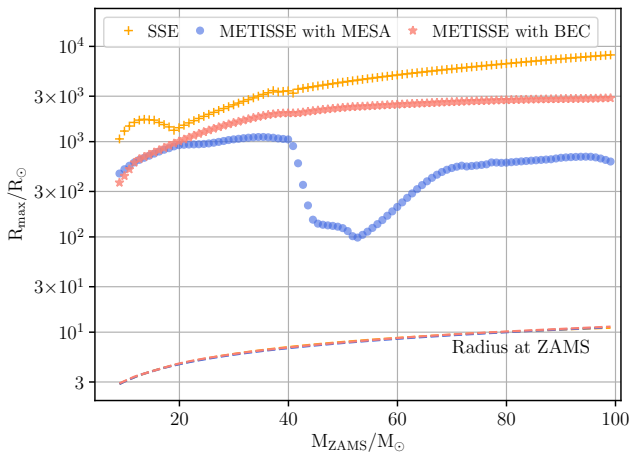
We tested METISSE with stellar models from MESA and the Bonn code (BEC) by calculating parameters for stars in the range of 9–100 $M_\odot$ at one-tenth of solar metallicity. Figure 2 shows the maximum radial expansion achieved by these stars as a function of their initial mass, as predicted by METISSE. For reference, the maximum stellar radii calculated with SSE for the same masses and metallicity are also plotted. Similar to Figure 1, stars with initial masses above 40 $M_\odot$ show a larger discrepancy ($\geq 1\,000\,R_\odot$) in the maximum radial expansion compared to other, lower mass stars. These are again an order of magnitude lower than what SSE predicts. The radial expansion of a star is important for determining its interaction with a binary companion. Thus, the different radii predicted by different stellar models can have a significant impact on the mass transfer and binary properties of the stars, which are important for predicting the formation of compact binary systems whose merger can give rise to the gravitational waves.

Conclusions

Uncertainties in the evolution of massive stars can play a significant role in predicting their evolutionary properties. Advances in observations and three-dimensional simulations might help resolve these uncertainties in the future. Until then, tools like METISSE are crucial for testing the impact of these uncertainties on the properties of stellar populations.

Figure 2: Maximum stellar radii as a function of the initial mass of the star, as predicted by SSE, METISSE with MESA, and METISSE with BEC.

References

[1] Cox, J., & Giuli, R., 1968, Principles of Stellar Structure: Physical principles. Principles of Stellar Structure, Gordon and Breach
[2] Paxton, B., et al. 2013, ApJS, 208, 4
[3] Cheng, Y., et al. 2015, MNRAS, 452, 1068
[4] Choi, J., et al. 2016, ApJ, 823, 102
[5] Paxton, B., et al. 2011, ApJS, 192, 3
[6] Ekström, S., et al. 2012, A&A, 537, A146
[7] Eggenberger, P., et al. 2008, Ap&SS, 316, 43
[8] Eldridge, J. J., et al. 2017, PASA, 34, e058
[9] Szécsi, D., et al. 2020, arXiv:2004.08203
[10] Belczynski, K., et al. 2008, ApJS, 174, 223
[11] Agrawal, P., et al. 2020, MNRAS, 497, 454
[12] Hurley, J. R., et al. 2000, MNRAS, 315, 543

Short CV

2016: Master in Physics, Savitribai Phule Pune University, India
2021: PhD in Astronomy, Swinburne University of Technology, Australia
2021: Postdoctoral researcher, Carnegie Mellon University, USA

Stromlo Stellar Tracks: the importance of non-Solar scaled abundances for massive stars

Kathryn Grasha

Research School of Astronomy and Astrophysics, Australian National University, Canberra ACT, Australia

ARC Centre of Excellence for All Sky Astrophysics in 3 Dimensions (ASTRO 3D), Australia

I present the Stromlo Stellar Tracks [1], a set of stellar evolutionary tracks for massive stars (>10 $M_\odot$), computed by modifying the `Modules for Experiments in Stellar Astrophysics` (MESA) 1D stellar evolution package, to fit the Galactic Concordance abundances for massive Main-Sequence stars. Until now, all stellar evolution tracks are computed at solar, scaled-solar, or alpha-element enhanced abundances, and none of these models correctly represent the observed abundances of H II regions in the Milky Way or Magellanic Clouds at a given metallicity [2, 3]. This paper is the first implementation of Galactic Concordance abundances to stellar evolution models. I find that adopting Galactic Concordance abundances can significantly affect the evolution of main-sequence, massive hot stars in order to estimate accurate stellar outputs (L, T_{eff}, g), which, in turn, have a significant impact on determining the ionising photon luminosity budgets. I additionally support prior findings of the importance that rotation plays on the evolution of massive stars and their ionizing budget. The evolutionary tracks for our Galactic Concordance abundance scaling provides a more physically motivated approach than simple uniform abundance scaling with metallicity for the analysis of H II regions and have considerable implications on predictions for nebular emission lines and line diagnostics. Moving beyond assumptions of the Solar elemental abundance scaling methods is critically needed to accurately interpret emission lines from theoretical models, the primary source of our physical understanding of the formation and evolution of galaxies. These tracks will allow consistent abundance ratios to be used in stellar population synthesis and photoionisation models to derive accurate galaxy diagnostics for the first time.

Background

A simple stellar population model describes how a coeval stellar population at a given mass, metallicity, and elemental abundance pattern evolves over its lifetime, referred to as "stellar evolution tracks". Stellar tracks are computed from stellar evolution theory and large observational stellar libraries. Stellar tracks require a set of elemental abundance ratios as an input parameter and have previously been calculated by scaling the relative abundance ratios to Solar. However, it is now known that Solar relative abundance ratios do not match Galactic Concordance abundances. Because of this, stellar tracks and opacity tables that represent the observed abundance ratios in the Milky Way and nearby galaxies need to be computed within current stellar evolution models to allow for self-consistency in stellar population synthesis and photoionisation models.

Stellar Evolution Calculations

The Stromlo Stellar Tracks [1] present stellar evolution models with the scaling abundances based on 'Galactic Concordance' abundances [3]. I use the MESA [4] stellar evolution code within the framework developed by MESA Isochrones and Stellar Tracks [MIST; 5]. The Stromlo Tracks cover the evolution of massive ($10 \leq M/M_\odot \leq 300$) stars with varying rotations (v/v_{crit} = 0.0, 0.2, 0.4) and a finely sampled grid of metallicities (–2.0 $\leq$ [Z/H] $\leq$ +0.5; Δ[Z/H] = 0.1).

I focus on massive (>10 $M_\odot$) stars as they have traditionally been neglected in prior stellar evolution models. In addition, massive, rotating stars dominate the ionising budget powering H II regions and are a vital component in controlling the physics that regulates the efficiency of star formation. Using Flexible Stellar Population Synthesis (FSPS; [6]), I generate synthetic spectra for the Stromlo tracks (Figure 1).
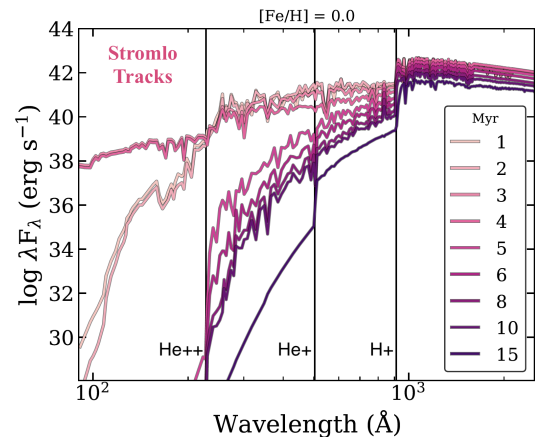

Figure 1: Synthetic spectra calculated using the Stromlo stellar tracks shown at different ages. The vertical lines represent the energies to ionise hydrogen and helium (singly and doubly).

Results – Stellar Rotation and Surface Abundances

Rotation in the massive (>100 $M_\odot$) stars heavily impacts their surface composition (Figure 2). These stars spend the vast majority of their main sequence lifes with enhanced He surface abundances consistent with the Wolf-Rayet evolutionary phase. For non-rotating massive stars, there are no diffusion mechanisms for the transport of chemical elements from the inner convective core to the outer convective shell, and therefore, there is little to no surface enhancement. The impact of rotation in altering the observed surface abundances of stars increases dramatically at lower metallicities.

Results – Stellar Ionising Spectra

Using the synthetic spectra (Figure 1), I calculate the total ionising photon rate Q to constrain the difference
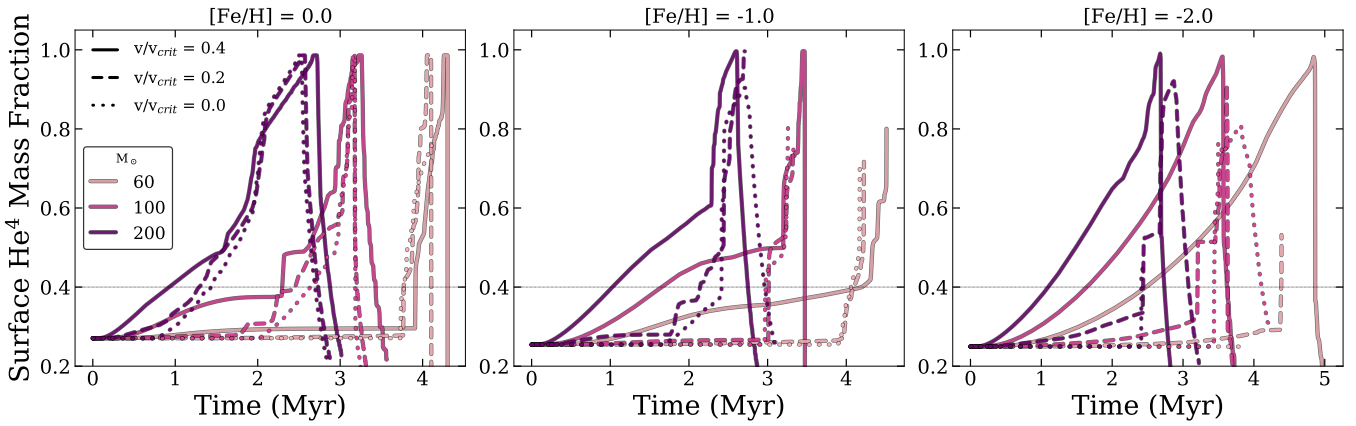
Figure 2: Time evolution of the surface ^{4}He abundances for 60, 100, and 200 M$_\odot$ Stromlo stars with v/v$_{\text{crit}}$ = [0.4, 0.2, 0.0] (solid, dashed, and dotted lines, respectively) at metallicities of [Fe/H] = [0.0, −1.0, −2.0] (left, middle, and right, respectively). The gray line at 0.4 marks the He abundance that delineates the start of the Wolf-Rayet phase of stellar evolution. The effects of rotation are more important (larger differences) at lower metallicity.
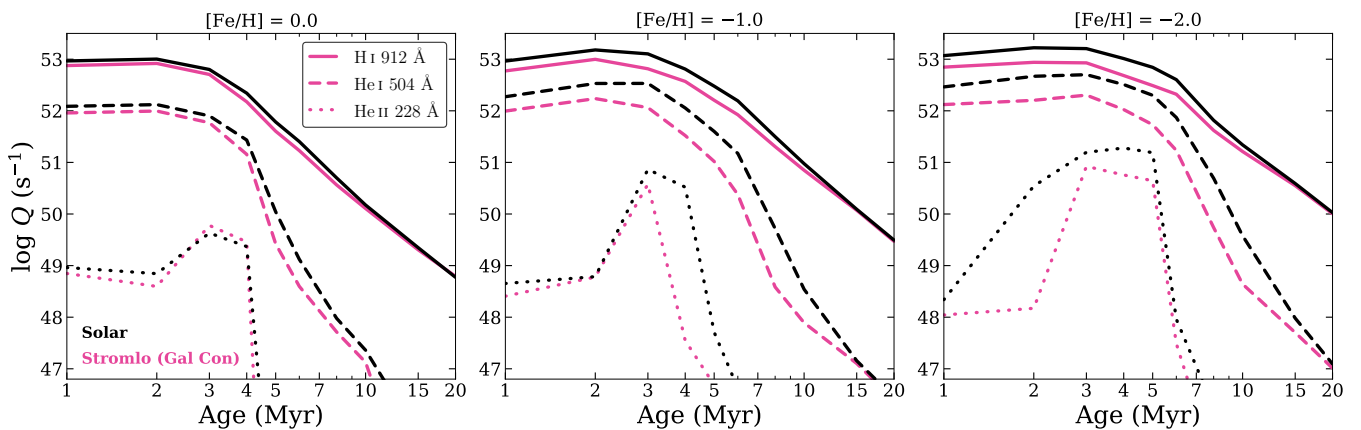

Figure 3: Time evolution of the ionising photon rate Q for the Stromlo models (Gal Con; pink) and Solar abundance models (black) for a 10^6 M$_\odot$ stellar population at [Fe/H] = 0.0 (left), −1.0 (middle), and −2.0 (right). The line-style represent the ionising photons capable of ionising hydrogen H$^+$ (912 Å; solid lines), singly ionising helium He$^+$ (504 Å; long dashed lines), and doubly ionising helium He^{++} (228 Å; short dotted lines). The ionising photon output for solar-scaled stars is overestimated at all metallicities, with the difference between the ionising budget of Solar and non-Solar becoming substantially larger at lower metallicities.

between Solar versus non-Solar scaled elemental abundances at varying metallicities (Figure 3). Solar-scaled abundances overpredict the stellar ionising spectra with discrepancies of up to 1 dex for the youngest stars at low metallicities. This has an enormous and substantial impact on the observed emission lines and subsequent galaxy diagnostics (SFR, metallicities, etc).

Implications and Future Work

This work demonstrates that it is essential to have a self-consistent picture of how stars ionise their local star-forming sites at different metallicities and abundances. In the future, the Stromlo tracks will be combined self-consistently with nebular photoionisation models, setting the foundation for realistic nebular emission line predictions from the *James Webb Space Telescope*. *JWST* will

obtain spectra for 100,000s of galaxies across 13 billion years of cosmic time. These new diagnostics from self-consistent modelling of galactic spectra will enable us to reliably interpret the wealth of data from the next generation of observatories. This undoubtedly will bring about a major advance in our understanding of how the physical properties of galaxies and their elemental compositions have evolved over the history of the universe.

References
[1] Grasha, K., et al. 2021, ApJ, 908, 241
[2] Nieva, M.F., & Przybilla, N. 2012, A&A, 539, A143
[3] Nicholls, D.C., et al. 2017, MNRAS, 466, 4403
[4] Paxton, B., et al. 2011, ApJS, 192, 3
[5] Choi, J., et al. 2016, ApJ, 832, 102
[6] Conroy, C., et al. 2009, ApJ, 699, 486

Short CV

2018: PhD in Astronomy, University of Massachusetts, United States
2018: Laureate Postdoctoral Fellow, Australian National University, Australia
2021: ASTRO 3D Fellow, Australian National University, Australia
2022: DECRA Fellow, Australian National University, Australia

Blue straggler stars in galactic open clusters

María José Rain

Università degli studi di Padova, Vicolo Osservatorio 3, 35122, Padova, Italy

The so-called Blue Straggler Stars (BSS) are exotic objects present in all stellar environments, whose nature and formation channels are still partially unclear. In the colour-magnitude (CMD) diagram of a stellar system, they appear blueward and above the turnoff (TO), on the continuation of the main sequence. This position is incompatible with the predictions of the standard stellar evolution theory of single stars, and multiple mechanisms have been proposed for their formation. In particular, in stellar clusters, BSS could be the product of direct collisions or mergers in dynamical encounters, the merger of a contact binary, mass transfer activity in binary systems, or the merger of a inner binary in a hierarchical triple system via Kozai-Lidov mechanisms. Hence, this population is extremely important because it can provide information on the dynamics, the binary population, and the history of the stellar evolution of the system they belong to. An extensive review of the BSS properties has recently been presented in [1].

BSS seem to find themselves particularly comfortable in open clusters (OCs). These systems hold many lessons about the origins of the BSS. Given their sparse nature and proximity, they enable an in-depth analysis of basic BSS characteristics such us frequency, orbital parameters, and masses. In this context, large and homogeneous catalogues are needed to properly understand, identify, and characterize this population. By searching relations between the straggler population and the cluster properties (e.g., mass, age, binary fraction) we can identify potential clusters for further targeted multi-epoch radial-velocity monitoring, and so reveal their properties and provide evidence to support or rule out the formation mechanisms so far proposed. Drawbacks of previous catalogue of BSS in OCs [2, 3] are the lack of homogeneity of the open cluster data available at the time they were published, and the uncertain membership of the BSS candidates. Now, however, by taking advantage of the *Gaia* DR2 survey, we can determine accurate membership and, consequently, put the study of BSS in OCs on a much more solid statistical ground for the first time. This work presents a new catalogue of blue straggler stars in a large sample of OCs. It is based on the inspection of the CMDs of 408 clusters, and a membership characterisation provided by the *Gaia* DR2 astrometric solution.

Main results

In total, 897 blue straggler candidates were identified in the 408 OCs investigated. The number of clusters with at least one blue straggler is 111 (27.20%). In comparison with [2] and [3], our percentage is $\sim 30\%$ and $\sim 20\%$ lower, respectively. Figure 1 shows the combined colour-magnitude diagram for all our straggler candidates, corrected for distance and extinction, and coloured according to the cluster age. We see that the brightest BSS are in the young clusters, as expected, and they become progressively fainter in older clusters. Some general highlights from our work are i) no blue straggler candidates were found in clusters with $\log(\text{age}) \leq 7.3$ (20 Myr) ii) the number of BSS in clusters with ages below 1 Gyr is relatively low, and around 70% (623) of them are in clusters older than $\log(\text{age}) = 9.3$ (2 Gyr) iii) there are on average 2.19 BSS per cluster.
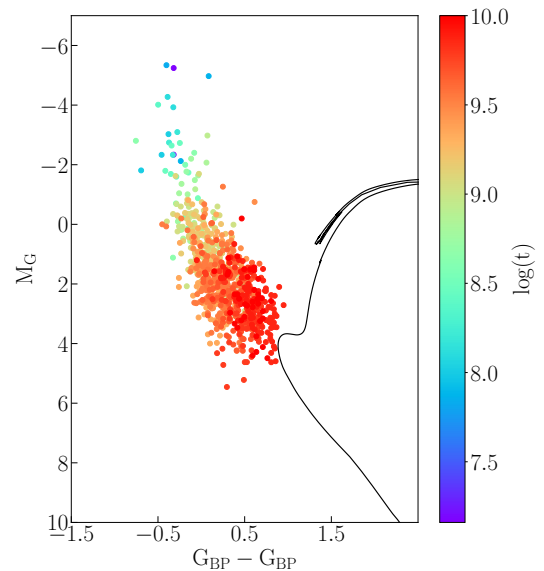

Figure 1: Colour-magnitude diagram showing dereddened, corrected-by-distance BSS candidates. The BSS are coloured according to the cluster age.

When comparing our catalogue with [3], we found large inconsistencies; for individual clusters, the percentage of BSS found to be non-members according to our criteria is about 10–60% of that catalogue. However, it is possible to retrieve about 70-100% of the BSS of [3] in close and very well studied clusters, specially in those with spectroscopic studies, like, e.g., NGC 188.

Using 107 clusters and BSS with membership probability $P_{\text{memb}} \geq 80\%$, we explored the dependency of the ratio $N_{\text{BSS}}/N_{\text{MSS}}$§§ and the cluster age (see Figure 2), metallicity, distance, and reddening. When comparing with the cluster age, we found two trends: i) $N_{\text{BSS}}/N_{\text{MSS}}$ is approximately constant—flat—for young clusters, until $\log(\text{age}) \sim 8.7$ (500 Myr, $M_{\text{TO}} = 2.4\ M_\odot$), and ii) the ratio shows a steep increase with cluster age starting from $\log(\text{age}) = 9.0$ (1 Gyr, $M_{\text{TO}} = 1.81\ M_\odot$) towards later ages. We also observed the plateau described by [4] in the range $9.3 < \log(\text{age}) < 9.6$. We can safely assume that the older clusters harbour more BSS. No clear relation with the cluster metallicity [Fe/H], distance, or reddening was found.

Although the anti-correlation between the specific frequency $N_{\text{BSS}}/N_{\text{HB}}$ and the integrated magnitude M_{v}

---

§§ N_{MSS} is the number of cluster main sequence stars down to 1 magnitude below the TO, adopted as a proxy of the cluster richness.

shown by [5] still holds for OCs using our data, this follows a different distribution, more similar to the one described by the globular clusters (GCs) in the same reference.

When comparing the total mass (M_{tot}) and the number of blue stragglers N_{BSS}[¶¶], we found a power-law relation of the form $N_{\text{BSS}} \propto M_{\text{tot}}^{0.3-0.43(\pm0.15)}$, very similar to the one found for GCs by [6] ($N_{\text{BSS}} \propto M_{\text{tot}}^{0.38\pm0.04}$). This could indicates that binaries dominated BSS formation in both type of clusters, and that the formation and evolution of BSS is quite similar in both open and globular clusters.
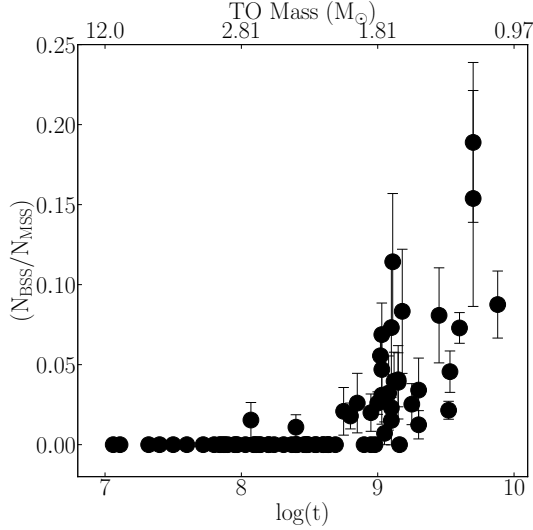

Figure 2: Ratio N_{BSS} /N_{MSS} as a function of the age in logarithmic scale. Errors are Poisson statistics.

Additionally we analysed in detail the BSS population of four old clusters—Collinder 261, NGC 2477, Trumpler 5, and Trumpler 20. The clusters were observed with FLAMES@VLT and the data were collected between January 2012 and March 2018, under ESO-programs 88.D-0045(A) and 0100.D-0052(A). By using the radial velocity variability technique, we assessed the BSS membership and classified them into members, non-members, close binaries (CB), and long-period binaries (LP); for more details, see [7, 8]. The spectra obtained for radial velocities also allowed us to obtain measurements of the projected rotational velocities. In all we found 10 CB (all within $30 \text{ km/s} \leq v \sin i \leq 270 \text{ km/s}$),

1 LP ($v \sin i = 30 \text{ km/s}$), 7 member non-variable stars (all within $10 \text{ km/s} \leq v \sin i \leq 40 \text{ km/s}$), one non-variable yellow straggler ($v \sin i = 10 \text{ km/s}$), and 3 non-members. It is possible that these non-velocity-variable BSS are indeed long-period binaries, perhaps outside of our detection limit. For those stars with data in the literature (3 BSS in Collinder 261), we estimated their masses. To fit the orbits we used our radial velocities and the periods reported in the literature. To derive the values of the mass of the secondaries (M_2), we first estimated the masses of the primaries (M_1) from the CMD. Finally, we obtained a M_2 for Crd261-BS4, Crd261-BS5, and Crd261-BS8, of 0.118 ± 0.005 $M_{\odot}$, 0.21 ± 0.01 $M_{\odot}$, and 0.42 ± 0.02 $M_{\odot}$ respectively.

Finally, by cross-matching our catalogue with the Transiting Exoplanet Survey Satellite (TESS), we found that 40% of BSS in Collinder 261 (9 Gyr) are in short-period binaries with orbital periods between 5 hours and 3 days. These results are at odds with the fraction of short-period binaries found among BSS in old open clusters (e.g., NGC 188 with 7 Gyr, and M67 with 4 Gyr), and may tell us important facts about the relative importance of the BSS formation mechanism as a function of the age of the cluster.

Conclusions

We have provided the scientific community with a new, internally consistent and homogeneous catalogue of BSS candidates in Galactic open clusters. We found 897 BSS in 408 OCs in the 1 Myr–10 Gyr age range. We have confirmed that the number of BSS increases with cluster age and cluster mass. Finally, we have performed the first spectroscopic analysis of the blue straggler population in four open clusters, where different types of binaries were identified among them.

References

[1] Boffin, H. M. J. 2015, "Ecology of Blue straggler stars", eds. H. M. J. Boffin,& G. Carraro, & G. Beccari, Springer 413
[2] Ahumada, J.A., & Lappaset, E. 1995, A&AS, 109, 375
[3] Ahumada, J.A., & Lappaset, E. 2007, A&A, 463, 789
[4] Leiner, E.M., & Geller, A. 2021, ApJ, 908, 229
[5] Momany, Y., et al. 2007, A&A, 468, 973
[6] Knigge, C., et al. 2009, Nature, 457, 228-290
[7] Rain, M.J., et al. 2020, AJ, 159, 59
[8] Rain, M.J., et al. 2021, AJ, 161, 37

Short CV

2015:   Bachelor in Astronomy, Universidad de Concepción, Chile
2018:   Master in Science/Physics, Universidad de Concepción, Chile
2018–present: PhD student, Universitá degli studi di Padova, Italy

[¶¶]This comparison was carried out using clusters with $N_{BSS} \geq 10$.

Panchromatic observations of X-ray binaries

Noel Castro Segura

University of Southampton, Southampton SO17 1BJ, UK

Accretion is the natural process by which objects in the universe grow in mass. As a consequence of the angular momentum typically carried by the accreted material, during this process, the material tends to organise itself in the form of a thin disc.

Disc winds and jets are ubiquitous among accreting systems on all scales, from active galactic nuclei down to young stellar objects. Thus, mass loss appears to be a universal – and perhaps necessary – part of the accretion process. These outflows can carry large amounts of mass and energy, representing a key mechanism by which these systems interact with their environment ("feedback"). They may also be responsible for the mysterious state changes observed in low-mass X-ray binaries (LMXBs; [1]).

Transient LMXBs harbouring black holes and neutron stars provide us arguably with one of the best laboratories for studying the interplay between accretion, jets and disc winds. While spending most of their time in quiescence, these systems undergo violent outbursts, during which they brighten dramatically across the whole electromagnetic spectrum. These outbursts typically last hundreds of days and reflect a sudden increase in the accretion rate onto the compact object. Over the course of an outburst, LMXBs exhibit two distinct spectral states. In quiescence and on the rise, the X-ray spectrum is dominated by a hard power law component. By contrast, near the peak of the eruption and during the early decline, most of the accretion luminosity emerges in a soft, thermal component. These spectral states are thought to be a consequence of different accretion geometries close to the central object. Specifically, the hard state is associated with a hot, optically thin, geometrically thick accretion flow, which is largely replaced by an optically thick, geometrically thin accretion disc in the soft state.

Intriguingly, a strong connection between these two spectral states and two distinct types of outflows is observed. In the hard state, steady compact radio jets are seen. On the other hand, during the soft state, blue-shifted absorption lines associated with highly ionised accretion disc winds are often observed. This anti-correlation between winds and jets in the different spectral states is poorly understood. One possibility is that both outflows are magnetically driven, but this would require a dramatic reconfiguration of the global magnetic field. On the other hand, the strong irradiation of the disc provides a natural explanation if the winds are thermally driven. Remarkably, blue-shifted absorption lines have recently also been discovered in optical and NIR recombination lines. These features must also be produced in an outflow, but the physical conditions traced by these outflows are different. Despite this, the characteristic Doppler velocities of all types of wind signatures are comparable, even though they have never been observed simultaneously.

While monochromatic observations can provide important insights of particular regions in the systems, multi-wavelength (MW) observations are required to develop a comprehensive physical picture. Coordinated observations across observatories at different wavelengths and resolutions have already provided groundbreaking insights into the physics of these accretion discs and their outflows. Examples include the determination of the magnetic field and location of the jet [2], its geometry and energetics [3] and evolution throughout an outburst [4], as well as how the dense winds can contribute to the transport of angular momentum, irradiation of the disc and how this affects their appearance and outburst evolution [5].

In this contribution, I present an overview of a MW campaign I have led which succeeded in obtaining simultaneous time-resolved observations of an erupting LMXB (*Swift J1858*) across the electromagnetic spectrum. This remarkable data set has already yielded the first detection of *ultraviolet* wind signatures in an transient LMXB [6], but there is much more yet to come.

Campaign overview

In Figure 1, I present an overview of the time-resolved simultaneous observations we obtained over a 4-hour window while *Swift J1858* was in its luminous hard state. The characteristic flaring of the source across all wavelengths is thought to be consequence of accretion taking place at super-Eddington rates. It is immediately obvious that the amplitude of the variations is increasing toward shorter wavelengths. Moreover, the absence of lags between different bands points to the X-ray emitting region as the driver of the strong variability.

The near-IR band exhibit strong short "bursts" on timescales of seconds on top of the normal flaring activity. The irregular morphology of these bursts indicate a non-thermal origin. However, there is no counterpart to these rapid variations at higher energies. The variable radio emission is likely driven by variations in the accretion flow being propagated to the compact jet. The lower panel shows the integrated flux of the Bowen blend + He II ($\lambda 4686$; B+He: this line complex can be interpreted as a proxy to the inaccessible extreme ultraviolet). In the same panel I also plot the significance with which wind signatures are detected (or not) in the Hα line (triangles). While the B+He follows the overall flaring variability, the wind signatures seems to be anti-correlated with it. More specifically, the wind is most clearly detected when the source is faintest (clearly illustrated during the first hour of the campaign). This could be interpreted as the wind signatures becoming undetectable as the outflow becomes over-ionised by the extreme radiation field.

References

[1] Shields, G. A., et al. 1986, ApJ 306, 90
[2] Gandhi, P., et al. 2010 MNRAS, 407, 2166
[3] Tetarenko, A. J., et al. 2021, MNRAS, 504, 3862
[4] Russell, T. D., et al. 2020 MNRAS, 498, 5772.
[5] Tetarenko, B. E., et al. 2020, MNRAS, 495, 3666
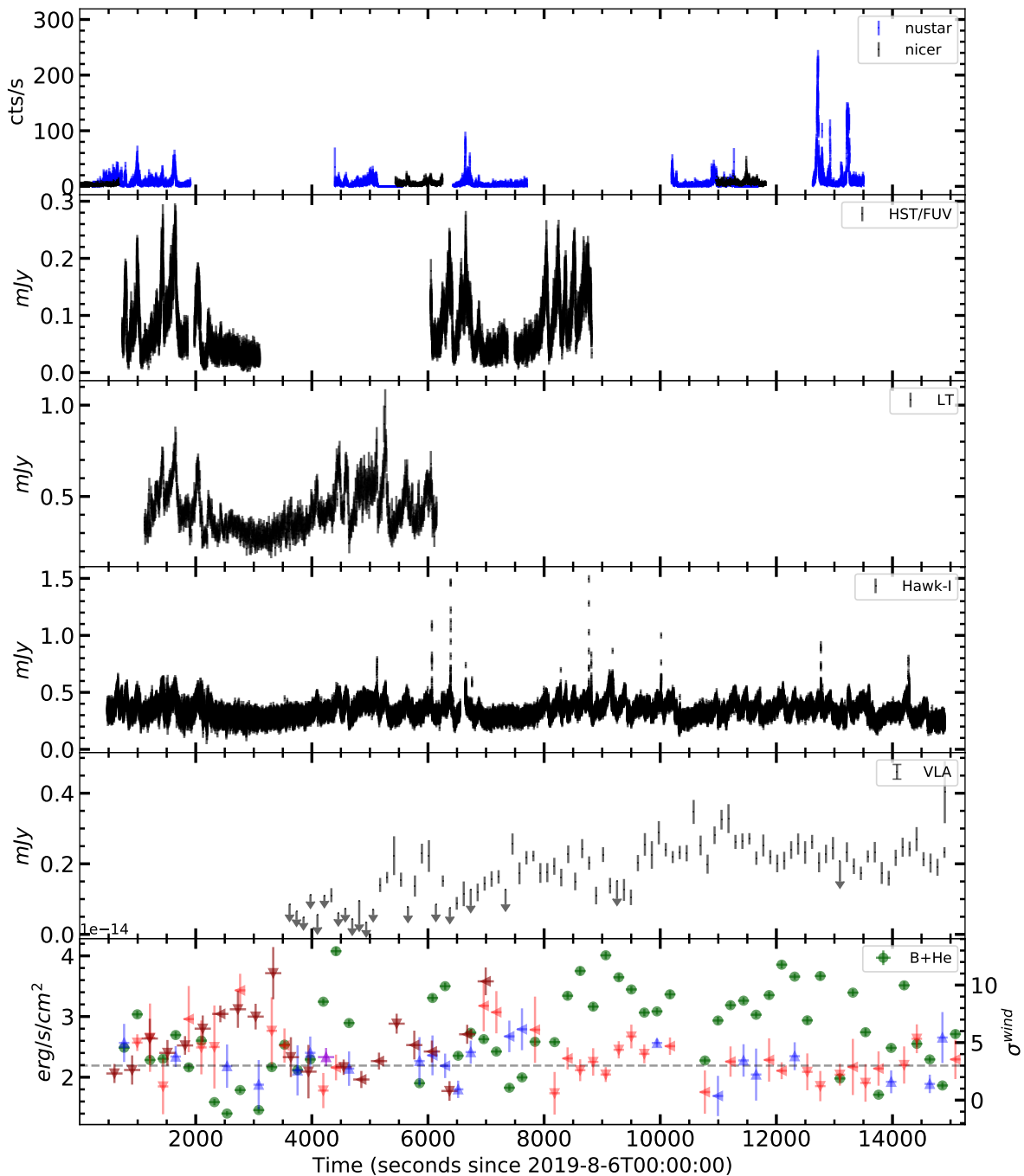[6] Castro Segura, N., et al. 2021, subm.

Figure 1: Overview of the strictly simultaneous data collected during the campaign. Instruments were sorted from top to bottom with increasing wavelength, in the X-rays *NICER* and *NuSTAR*, *HST* in the UV, *Liverpool Telescope* in the optical, *VLT/HAWK-I* in the near-IR and *VLA* ($4.5 + 7.5$ GHz bands) in radio. Finally, in the bottom panel the flux of the Bowen blend and the optical He II as measured from the *VLT/X-Shooter* spectra is shown with green dots. The dark (GTC/OSIRIS) and light (VLT/X-Shooter) triangles in the same panel indicate the significance of the wind signatures (right axis) and the horizontal dashed line indicate the 3σ level.

Short CV

2016: BSc in Physics, University of La Laguna, Tenerife, Spain
2017: Master in Astrophysics, University of La Laguna, Tenerife, Spain
2021: PhD in Astrophysics, University of Southampton, UK

Hypatia

Wikipedia

Hypatia (born c. 350–370; died 415 AD) was a Greek Neoplatonist philosopher, astronomer, and mathematician, who lived in Alexandria, Egypt, then part of the Eastern Roman Empire. She was a prominent thinker of the Neoplatonic school in Alexandria where she taught philosophy and astronomy. Although preceded by Pandrosion, another Alexandrine female mathematician, she is the first female mathematician whose life is reasonably well recorded. Hypatia was renowned in her own lifetime as a great teacher and a wise counselor. She wrote a commentary on Diophantus's thirteen-volume Arithmetica, which may survive in part, having been interpolated into Diophantus's original text, and another commentary on Apollonius of Perga's treatise on conic sections, which has not survived. Many modern scholars also believe that Hypatia may have edited the surviving text of Ptolemy's Almagest, based on the title of her father Theon's commentary on Book III of the Almagest.

Hypatia constructed astrolabes and hydrometers, but did not invent either of these, which were both in use long before she was born. Although she herself was a pagan, she was tolerant towards Christians and taught many Christian students, including Synesius, the future bishop of Ptolemais. Ancient sources record that Hypatia was widely beloved by pagans and Christians alike and that she established great influence with the political elite in Alexandria. Towards the end of her life, Hypatia advised Orestes, the Roman prefect of Alexandria, who was in the midst of a political feud with Cyril, the bishop of Alexandria. Rumors spread accusing her of preventing Orestes from reconciling with Cyril and, in March 415 AD, she was murdered by a mob of Christians led by a lector named Peter.

Hypatia's murder shocked the empire and transformed her into a "martyr for philosophy". [Around the end of the nineteenth century,] European philosophers and scientists described Hypatia as the last representative of science and free inquiry before a "long medieval decline". In the twentieth century, Hypatia became seen as an icon for women's rights and a precursor to the feminist movement.

Figure 1: This fictional portrait of Hypatia by Jules Maurice Gaspard, originally the illustration for Elbert Hubbard's 1908 fictional biography, has now become, by far, the most iconic and widely reproduced image of her.

Hypatia was honored as an astronomer when 238 Hypatia, a main belt asteroid discovered in 1884, was named for her. The lunar crater Hypatia was also named for her, in addition to craters named for her father Theon. The 180 km Rimae Hypatia are located north of the crater, one degree south of the equator, along the Mare Tranquillitatis.